

6-20-2023 2:00 PM

Multiparametric Classification of Tumor Treatment Using Ultrasound Microvascular Imaging

mahsa bataghva, *Western University*

Supervisor: James C. Lacefield, *The University of Western Ontario*

A thesis submitted in partial fulfillment of the requirements for the Doctor of Philosophy degree
in Biomedical Engineering

© mahsa bataghva 2023

Follow this and additional works at: <https://ir.lib.uwo.ca/etd>



Part of the [Other Biomedical Engineering and Bioengineering Commons](#)

Recommended Citation

bataghva, mahsa, "Multiparametric Classification of Tumor Treatment Using Ultrasound Microvascular Imaging" (2023). *Electronic Thesis and Dissertation Repository*. 9324.
<https://ir.lib.uwo.ca/etd/9324>

This Dissertation/Thesis is brought to you for free and open access by Scholarship@Western. It has been accepted for inclusion in Electronic Thesis and Dissertation Repository by an authorized administrator of Scholarship@Western. For more information, please contact wlsadmin@uwo.ca.

Abstract

Ultrasound-based microvascular imaging is a promising technique for evaluating tumor response to antiangiogenic therapy in preclinical settings. However, challenges such as tissue motion and noise can hinder the accuracy and reliability of contrast-free ultrasound imaging. Additionally, there is a lack of consensus on how to best combine different microvascular ultrasound techniques, like contrast-free and contrast-enhanced ultrasound, for detecting treatment response in cancer models. To address these challenges, this thesis proposes an optimal shrinkage singular value decomposition (SVD) based clutter filtering method. The proposed method significantly enhances visualization and microvascular quantification by increasing the signal-to-noise ratio (SNR) and contrast-to-noise ratio (CNR).

Additionally, a scalable preclinical tumor model is presented using ex-ovo chick chorioallantoic membrane (CAM) tumor model and machine learning algorithms. The model aims to classify renal cell carcinoma (RCC) tumor cell response to antiangiogenic treatment based on ultrasound microvascular and perfusion parameters. Perfusion parameters derived from optimal shrinkage SVD-based contrast-free ultrasound and statistical analysis of contrast-enhanced ultrasound, along with microvascular parameters from conventional analysis, are evaluated. Feature selection algorithm identifies the best combination of ultrasound-based perfusion parameters for classification. The study expands from using control and treatment groups of a sensitive cell line to using two different cell lines with varying sensitivity levels. The model pipeline is also tested on an independent cell line with unknown sensitivity to the machine learning model.

The results demonstrate the effectiveness of the model in studying antiangiogenic treatment response using ultrasound microvascular imaging. The newly developed analysis for contrast-free and contrast-enhanced ultrasound improves classification results, and the model performs well with a separate test set, demonstrating its generalization capabilities and robustness. Therefore, the proposed model pipeline has the potential to evaluate treatment response in other tumor cells and preclinical translation.

In summary, this thesis highlights that optimal shrinkage SVD-based clutter filtering method improves microvascular quantification and its vascular quantification parameters when used along with other contrast-free and contrast-enhanced perfusion parameters improves the classification of the RCC tumor responses to antiangiogenic treatment in the proposed tumor chick CAM model. The results demonstrate the robustness of this study, and its potential for broader preclinical applications.

Keywords: Anti-Angiogenic Treatment Response, Cancer Imaging, Cell Lines, Clutter Filter, Contrast-Enhanced Ultrasound Imaging, Contrast-free ultrasound imaging, Ex Ovo CAM Tumor Model, Feature Analysis, Machine Learning, Morphological Analysis, Mouse Hindlimb Perfusion Model, Perfusion Parameters, Power Doppler Ultrasound Imaging, Singular Value Decomposition, Speckle Statistics, Tumor Cell Lines, Ultrasound Microvascular Imaging, Vascular Quantification

Summary for Lay Audience

Ultrasound imaging holds promise for investigating the response of tumors to a type of therapy that aims to degrade the microvessels. However, there are challenges that can compromise the accuracy of ultrasound images in detecting microvessels. Furthermore, there is currently no established method for determining the optimal combination of ultrasound-based microvessel parameters to effectively assess treatment efficacy. This thesis proposes a novel approach to enhance the ultrasound images in detection and quantification of microvessels, facilitating the observation and measurement of tumor blood vessels.

Additionally, this study introduces a scalable preclinical tumor model utilizing machine learning models and is based on ultrasound-based microvascular parameters. The objective of the model is to assess the response of kidney cancer tumor cells to anti-angiogenic treatment by analyzing different ultrasound images and conducting blood flow measurements within the tumor. Initially, blood flow measurements and vascular quantifications were computed for a responsive tumor cell to the treatment used in this study for both the treated group and non-treated group. This analysis was subsequently expanded to include two distinct tumor types, each exhibiting different responses to treatment. Moreover, the model was evaluated using a new tumor cell to ascertain its ability to accurately predict treatment response.

The study demonstrates that the proposed model is valuable for evaluating the efficacy of the treatment in inhibiting tumor blood supply using ultrasound imaging. Furthermore, the newly proposed method for enhancing ultrasound imaging exhibits improved discriminative capabilities for tumors with varying treatment responses, as facilitated by machine learning. The model also demonstrates robust performance when tested with independent tumor cells, suggesting its potential for assessing treatment responses in other tumor types. Overall, this model has the potential to aid in the study and translation of preclinical cancer treatments.

In summary, this thesis establishes that the proposed method enhances the measurement of tumor blood vessels in a specific ultrasound imaging modality. When combined with other ultrasound imaging techniques, it augments the model's ability to differentiate between tumor responses to treatment. The study yields robust results, indicating that this approach holds promise for broader preclinical applications in evaluating tumor responses to treatment.

Co-Authorship Statement

This dissertation is prepared in the integrated article format. Chapter 2, 3 and 4 are based on a manuscript that is under preparation for transactions on medical imaging (TMI), and the four published conference proceedings and one submitted abstract to international ultrasonic symposium (IUS) over my PhD program.

Chapter 2 is based on an original research article entitled “Contrast-Free Ultrasound Microvascular Imaging With Optimal Shrinkage Clutter Filtering to Enhance Vascular Quantification” and is under preparation for Transactions on medical imaging (TMI), 2023. This manuscript is co-authored by Mahsa Bataghva, Fiona Serack, Christopher Leclerc, Danielle Johnston, David Hess, Lauren Flynn, Nick Power, Silvia Penuela and James C. Lacefield. I was responsible for developing the idea of optimal shrinkage clutter filtering method, experimental design, and all image acquisition, image and data analysis, as well as manuscript preparation. Fiona Serack, Christopher Leclerc assisted with providing mice underwent unilateral femoral artery and vein ligation for mice hindlimb perfusion experiment while Danielle Johnston provided support for chick CAM experiments. James C. Lacefield, as the principal investigator and supervisor, designed the study, reviewed the results, gave editorial assistance, and provided mentorship. The initial results of this extensive study were published at IUS 2020 conference:

- **M. Bataghva**, F. Serack, C. Leclerc, D. Johnston, D. Hess, L. Flynn, N. Power, S. Penuela and J. C. Lacefield, " Contrast-Free Ultrasound Microvascular Imaging With Optimal Shrinkage Clutter Filtering to Enhance Vascular Quantification", IEEE Transactions on Medical Imaging (Submitted)
- **M. Bataghva**, D. Johnston, N. Power, S. Penuela and J. C. Lacefield, "Contrast-Free Ultrasound Microvascular Imaging With Optimal Clutter Shrinkage to Enhance Tumor Vascular Quantification," *2020 IEEE International Ultrasonics Symposium (IUS)*, Las Vegas, NV, USA, 2020, pp. 1-4

Chapter 3 is based on two published conference proceeding papers as the basis for my research. These two conference proceedings were co-authored by Danielle Johnston, Nick Power, Silvia Penuela, and James C. Lacefield. Danielle helped a lot in the CAM tumor model preparation and experiments, Silvia helped with the biology considerations of the

experiments while Nick supported and trained me on the expectations for tumor response to antiangiogenic treatment. Jim made significant contributions to the research presented in this chapter. He provided guidance on the research design, methodology, and data analysis. In addition, he reviewed and edited the manuscript, providing valuable feedback and suggestions throughout the writing process.

- **M. Bataghva**, D. Johnston, N. Power, S. Penuela and J. C. Lacefield, "Ultrasound-Based Microvascular Parameters for Classification of Anti-Angiogenic Tumor Treatment Response: A Scalable Preclinical Approach," *2020 IEEE International Ultrasonics Symposium (IUS)*, Las Vegas, NV, USA, 2020, pp. 1-4
- **M. Bataghva**, D. Johnston, N. Power, A. Ward, S. Penuela and J. C. Lacefield, "Comparison of Contrast-Enhanced Ultrasound Parameters for Classification of Anti-Angiogenic Tumor Treatment Response," *2021 IEEE International Ultrasonics Symposium (IUS)*, Xi'an, China, 2021, pp. 1-4

Chapter 4 is built upon another published conference proceeding paper that I co-authored with Danielle Johnston, Nick Power, Aaron Ward, Silvia Penuela, and James C. Lacefield. Aaron provided guidance on the machine learning model design and data analysis part while the contribution of the rest of the authors are similar to the previous articles.

- **M. Bataghva**, D. Johnston, N. Power, A. Ward, S. Penuela and J. C. Lacefield, "Multiparametric Microvascular Ultrasound to Classify Tumor Sensitivity to Anti-Angiogenic Treatment: Application to Multiple Cell Lines" *2022 IEEE International Ultrasonics Symposium (IUS)*, Venice, Italy, 2022, pp. 1-4

Dr. James C. Lacefield, as the senior co-author of the above articles, approves the use of their contents in this thesis.

Acknowledgments

I would like to express my gratitude to all those who have helped me throughout my journey of completing this thesis.

First and foremost, I would like to express my sincere gratitude to my thesis supervisor, Dr. James C. Lacefield, for his unwavering support, guidance, and mentorship throughout this journey. His expertise, feedback, and dedication were crucial in shaping my research and bringing this project to fruition.

I would also like to extend my heartfelt thanks to my advisory committee, Dr. Nicolas Power, Dr. Silvia Penuela and Dr. Aaron Ward, for their invaluable contributions, insightful comments, and constructive feedback, which helped me improve the quality and rigor of my research. Special thanks to Dr. Silvia Penuela and her team for providing me with the resources, facilities, and their assistance in experimental aspects of my work.

Words cannot express how grateful I am to have my lovely family. I would like to thank my parents, Maryam and Alireza who have devoted their lives to making the best possible for my sister, Safa, and I. Their unconditional love, support, and advice that always enlightened my way. Their unwavering support and belief in me have been a source of inspiration and motivation, and I am fortunate to have such wonderful people in my life.

Lastly, I would like to thank my husband, Mojtaba, whose love, guidance, and support have been the foundation of my academic journey.

Thank you all for your support, encouragement, and contributions to my thesis project. I am grateful beyond words.

Table of Contents

Abstract	i
Summary for Lay Audience	iii
Co-Authorship Statement	v
Acknowledgments	vii
Table of Contents	viii
List of Tables	xi
List of Acronyms and Abbreviations	xiv
1 Introduction	1
1.1 Overview	1
1.2 Ultrasound Microvascular Imaging and Its Applications	2
1.2.1 Overview of Power Doppler Ultrasound Image Acquisition and Construction	4
1.2.2 Overview of Contrast-Enhanced Ultrasound Imaging.....	9
1.2.3 Utility of Quantitative Ultrasound Imaging in Cancer Research.....	16
1.3 Preclinical Models Employed in This Thesis	18
1.3.1 Chick CAM Tumor Model.....	18
1.3.2 Mouse Hindlimb Perfusion Model.....	21
1.4 Application of Machine Learning in Ultrasound	22
1.4.1 ML in Ultrasound Image Acquisition and Reconstruction	22
1.4.2 ML in Ultrasound Image Interpretation	23
1.5 Hypotheses and objectives	25
1.6 Thesis outline	26
1.6.1 Chapter 2.....	277
1.6.2 Chapter 3.....	27
1.6.3 Chapter 4.....	27
1.6.4 Chapter 5.....	28
References	29
2 Contrast-Free Ultrasound Microvascular Imaging with Optimal Shrinkage Clutter Filtering to Enhance Vascular Quantification	34
2.1 Introduction.....	35
2.2 Theory of Optimal Shrinkage	37
2.2.1 Principals of Optimal Shrinkage	37
2.2.2 Application to Contrast-free Microvascular Ultrasound.....	39
2.3 Methods and Materials.....	40
2.3.1 Ex Ovo CAM Tumor Model.....	40

2.3.2	Murine Peripheral Arterial Disease Model	41
2.3.3	Contrast-Free Microvascular Imaging	41
2.3.4	Morphological Analysis of Vessel Networks	43
2.3.5	Image Quality Metric	43
2.4	Results	44
2.4.1	Visual Comparison of SVD Clutter Filtered Images	44
2.4.2	Vascular Network Morphological Parameters	50
2.4.3	Image Quality Metric	51
2.5	Discussion	52
2.6	Conclusion and Future Works	55
	References	57
3	Ultrasound-Based Microvascular Parameters for Classification of Anti-Angiogenic Tumor Treatment Response	59
3.1	Introduction	60
3.1.1	PD Microvascular Quantification	61
3.1.2	CEUS Perfusion Analysis	62
3.1.3	Machine Learning Models for Antiangiogenic Treatment Response	63
3.2	Methods and Materials	63
3.2.1	Study Design	63
3.2.2	Ex-Ovo Tumor Model Experiment	65
3.2.3	Power Doppler Image Acquisition and Analysis	66
3.2.4	CEUS Image Acquisition and Analysis	67
3.2.5	Classification and Feature Selection Algorithms	68
3.3	Results	70
3.3.1	Power Doppler and CEUS Vascular Parameters	70
3.3.2	Tumor Treatment Classification Response	72
3.3.3	CEUS + conventional PD and optimal shrinkage SVD-filtered PD analysis	73
3.3.4	Feature Selection	75
3.4	Discussion	75
3.4.1	Scalable Preclinical Model for Tumor Treatment Response Evaluation ..	75
3.4.2	Utility of a Statistical CEUS Analysis for Tumor Response Evaluation ..	78
3.5	Conclusion	80
	References	81
4	Generalization of Multiparametric Microvascular Ultrasound Models to Assess Tumor Response to Anti-Angiogenic Treatment	83
4.1	Introduction	84
4.1.1	A more comprehensive study with more perfusion parameters to classify resistant and sensitive tumors to antiangiogenic treatment	85
4.1.2	Evaluate classification performance on an independent tumor	85
4.1.3	Study Design	86
4.2	Materials and Methods	88
4.2.1	Tumor Model Experiment	88
4.2.2	Image Acquisition and Feature Analysis	88
4.2.3	Classification and Feature Selection Algorithms	89
4.3	Results	91

4.3.1	Perfusion parameters for cell lines with different sensitivity level to antiangiogenic therapy	91
4.3.2	Utility of Lab-developed versus Conventional PD and CEUS perfusion parameters in Tumor Treatment Response Classification	92
4.3.3	Feature Importance Analysis	93
4.3.4	Robustness and Generalization capabilities of the model pipeline.....	94
4.4	Discussion	95
4.5	Conclusion	97
	References	98
5	Conclusion and Future Works.....	100
5.1	Summary	100
5.2	Future Works	101
5.2.1	Optimal Shrinkage SVD Clutter Filtering	101
5.2.2	Other Tumor and Animal Models to Study Anti-Angiogenic Therapy Effectiveness	102
5.2.3	Use of Additional Parameters for Tumor Treatment Response.....	104
5.2.4	Use of Ultrasound-based Perfusion Parameters in Other Anti-Angiogenic Treatment Response Evaluation.....	104
5.3	Conclusion	105
	References	107
	Appendix: Copyright Approval.....	108
	Curriculum Vitae	115

List of Tables

Table 2.1: NV = number of vessels, NB = number of branching points, VL = mean vessel length for 22 tumors and 8 mice hindlimb images.	50
Table 2.2: SNR and CNR for the two applications using reconstructed images after truncated SVD and optimal shrinkage SVD.	52
Table 3.1 lists the means and standard deviations of the vascular parameters.	70
Table 3.2: Perfusion parameters from conventional and statistical analysis of CEUS.....	72
Table 3.3: Classification results using only perfusion parameters from conventional CEUS.	72
Table 3.4: Classification performance for comparing the usefulness of conventional and statistical analysis of CEUS	74
Figure 3.5 List of selected features among conventional and statistical CEUS.	75
Table 4.1: Perfusion parameters of conventional and developed PD and CEUS	91
Table 4.2: Classification results using two different tumor cell lines.....	92
Table 4.3: Classification results using 786-O tumor cell line.....	94

List of Figures

Figure 0.1: Tumor model pipeline to assess tumor treatment response to antiangiogenic therapy using ultrasound microvascular parameters.....	3
Figure 1.2: CEUS tumor images (a) baseline (unenhanced) and at (b) peak bolus enhancement, with (c) corresponding Pareto fits to intensity ROI histograms, and (d) weighting functions.....	14
Figure 1.3: Perfusion Parameters Based on Time Intensity Curve.....	15
Figure 1.4: Progression of chick embryo development in weigh boat <i>ex-ovo</i> culture vessel used in this study.....	19
Figure 2.1: Reconstructed images of tumors engrafted on the CAM of chick embryo after truncated and optimal shrinkage SVD clutter filtering.....	45
Figure 2.2: Reconstructed images of mice hindlimb after truncated and optimal shrinkage SVD clutter filtering..	46
Figure 2.3: Singular value curves for truncated and optimal shrinkage SVD filtered images of tumor images..	48
Figure 2.4: Singular value curves for truncated and optimal shrinkage SVD filtered images of mouse hindlimb images..	49
Figure 2.5: Segmented blood flow of the reconstructed images of both tumor and hindlimb after optimal shrinkage clutter filtering to SNR and CNR evaluation.....	51
Figure 3.1: Chick CAM Tumor Model and Development Timeline	66

Figure 3.2: Nonlinear contrast-enhanced ultrasound (CEUS) images of a control tumor engrafted on the CAM of a chick embryo. a) Baseline image. b) Image at peak enhancement..	71
Figure 3.3: Scatter plot of vascularization index and number of branching points for sunitinib-treated (blue circles) and DMSO-control red circles) tumors.	73
Figure 3.4: The ROC curve of the three logistic regression models.....	74
Figure 4.1: Feature importance analysis	93
Figure 4.2: SHAP value of all twelve features used in this study.....	94

List of Acronyms and Abbreviations

2-D	Two-dimensional
3-D	Three-dimensional
AROC	Area under the receiver operative curve
AUC	Area under the curve
CAM	Chorioallantoic membrane
CEUS	Contrast-enhanced ultrasound
CNN	Convolutional neural network
CNR	Contrast-to-noise ratio
DMSO	Dimethyl sulfoxide
EDD	Embryonic development day
FI	Flow index
FIR	Finite impulse response
FOV	Field of view
Hz	Hertz
IIR	Infinite impulse response
IQ	In-Phase Quadrature
LDRW	Local density random walk
LR	Logistic regression
MB	Micro bubble
ML	Machine learning
MLE	Maximum likelihood estimators
mRCC	Metastatic renal cell carcinoma
MTT	Mean Transit Time
MVD	Micro vascular density
NB	Number of branching points
NV	Number of vessels
PAD	Peripheral Arterial Disease
PBS	Phosphate-buffered saline

PD	Power Doppler
PDF	Probability density function
PDX	Patient derived xenograft
PE	Peak enhancement
PRF	Pulse repetition frequency
RCC	Renal cell carcinoma
RF	Radio Frequency
ROC	Receiver Operating curve
ROI	Region of interest
SHAP	Shapely additive explanations
SNR	Signal-to-noise ratio
SVD	Singular value decomposition
SVM	Support Vector Machine
TTP	Time to peak
UMI	Ultrasound microvascular imaging
VEGF	Vascular Endothelial Growth Factor
VFI	Vascularization flow index
VI	Vascularization index
VL	Vessel length
WIC	Wash-in curve

Chapter 1

1 Introduction

1.1 Overview

Ultrasound-based microvascular imaging, *i.e.*, power Doppler (PD) and Contrast Enhanced Ultrasound (CEUS), are popular imaging modalities in preclinical and clinical settings for assessing microvascular perfusion parameters including blood flow, blood volume, and microvascular density. The technique enables the visualization of small blood vessels, providing valuable information on microvascular function, morphology, and density. In recent years, microvascular imaging has become an essential tool in both angiogenesis and anti-angiogenesis research, especially in the field of cancer research. However, the accuracy and reliability of these measurements are still a challenge due to factors such as tissue motion, signal attenuation, and noise. To improve the quality and reliability of ultrasound-based perfusion imaging, several approaches have been proposed, including contrast-enhanced ultrasound imaging and power Doppler ultrasound imaging.

Machine learning models can be used to analyze these parameters to derive insights into the efficacy and the progression of angiogenesis and anti-angiogenesis therapy. Machine learning models have been increasingly used in the field of angiogenesis and anti-angiogenesis therapy, particularly in the context of ultrasound microvascular perfusion parameters and have the potential to revolutionize detect tumor treatment response in patients with various diseases. These models can identify patterns and changes in the images that may not be easily detectable by the human eye, providing a more accurate and objective assessment of treatment response. By analyzing parameters such as blood flow, vessel density, and perfusion, these models can predict the success of treatment and guide clinical decision-making. The use of machine learning models in ultrasound imaging has

the potential to improve patient outcomes and enhance the precision of diagnosis and treatment in patients with vascular disease.

Chick Chorioallantois Membrane (CAM) tumor models and mice hindlimb are popular preclinical applications for tumor treatment response and angiogenesis of peripheral arterial disease studies, respectively. The CAM tumor model is an efficient and cost-effective preclinical model for angiogenesis studies while mice hindlimb an easily accessible, well-defined and reproducible model for studying angiogenesis and perfusion in response to different treatments and they are genetically similarity to humans.

This thesis aimed to determine the essential combination of microvascular ultrasound features required to accurately classify the sensitivity of a tumor model (*i.e.*, tumor cells engrafted on the CAM of chick embryo) to antiangiogenic treatment using classical machine learning methods. The rest of this chapter aims to provide a comprehensive overview of the enhancements in microvascular imaging, with a focus on power Doppler and CEUS ultrasound imaging and the application of machine learning models anti-angiogenesis therapy using power Doppler and CEUS ultrasound microvascular perfusion parameters CAM tumor model preclinical application of and mice hindlimb.

1.2 Ultrasound Microvascular Imaging and Its Applications

Ultrasound microvascular imaging (UMI) [1] is a non-invasive and real-time imaging technique providing valuable information on microvascular function, morphology, and density. UMI can create high-resolution images of blood flow and vessel structure in real-time and has the potential to improve patient outcomes and enhance the precision of diagnosis and treatment. Traditionally, color and power Doppler have been widely used for visualizing microvascular flow without the need for contrast agents. These techniques rely on Doppler shift of the reflected sound wave relative to the transmitted wave and both are overlaid on bright-mode (B-mode) data using a variety of color hues. Power Doppler and color Doppler both use ultrasound to measure blood flow in vessels, rely on the Doppler effect, which is the change in frequency of sound waves as they reflect off moving objects, and they both produce images that are superimposed on a B-mode ultrasound image.

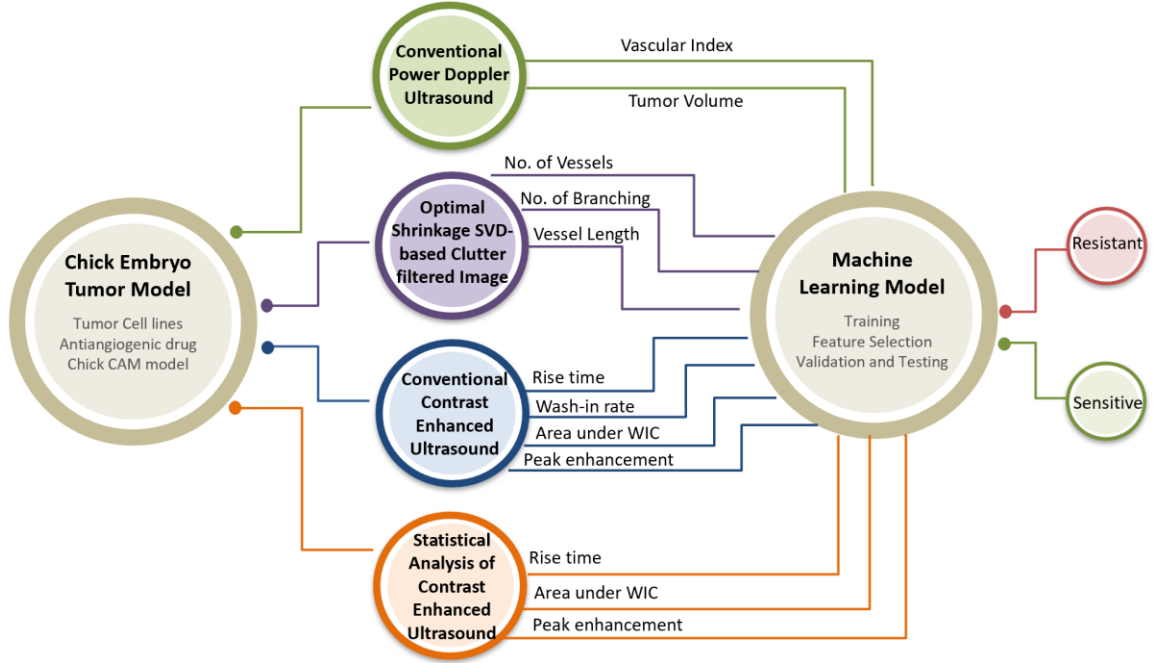


Figure 1.1: Tumor model pipeline to assess tumor treatment response to antiangiogenic therapy using ultrasound microvascular parameters

Color Doppler [2] image is generated by calculating the average Doppler frequency, based on the analysis of phase shifts or time delays between the echoes received and displays an estimate of the axial blood velocity from mean frequency estimate. Power Doppler ultrasound, on the other hand, distinguishes between echoes from moving red blood cells and solid tissues by estimating the power of the slow-time signal, which represents blood flow over time. The slow-time signal in ultrasound represents the changes in blood flow over time in a region of interest. The power of the slow-time signal is proportional to the number and movement of red blood cells in the region of interest and reflects the concentration of moving blood scatterers. Slow-time signal is different from the fast-time signal which represents the spatial distribution of echoes within a single pulse. in the region of interest. The slow-time signal is used to form power Doppler images, while the fast-time signal is used to form B-mode images.

The B-mode sequence in ultrasound imaging involves acquiring ultrasound data to generate grayscale images of anatomical structures. Focused beam imaging uses a narrow, focused ultrasound beam that is mechanically scanned across the region of interest, providing high

spatial resolution and detailed visualization at the focal depth. In contrast, plane-wave imaging insonifies the entire field of view simultaneously, allowing for rapid image acquisition and real-time imaging with a high frame rate. However, the spatial resolution of plane-wave imaging is generally lower since the beams are not concentrated on a specific target area.

Nowadays, advanced flow imaging techniques are commercially available on high-end ultrasound systems, such as Superb Microvascular Imaging (SMI) from Canon Medical, Slow Flow from Siemens Healthineers, Microvascular Imaging (MVI) from GE Healthcare, MicroFlow Imaging from Philips, and MV-flow from Samsung. [3]. This approach, also known as contrast-free ultrasound, is based on the detection of motion of the surrounding tissue caused by blood flow [4]. Contrast-free ultrasound exploits the high sensitivity of power Doppler to slow flow signals from small vessels and uses spatiotemporal signal processing to suppress the background tissue motion artifacts and enhance the signals from the moving blood cells to improve sensitivity to Doppler signals with slower flow. Contrast-free ultrasound does not require any contrast agents or injections and is therefore non-invasive and safer than contrast-enhanced techniques.

1.2.1 Overview of Power Doppler Ultrasound Image Acquisition and Construction

The image acquisition process in power Doppler imaging is similar to conventional B-mode ultrasound imaging. A transducer is placed on the surface and emits high-frequency sound waves that penetrate the body tissues. The sound waves are then reflected back by the tissue interfaces and detected by the transducer. The reflected signals are processed by the ultrasound system to generate a two-dimensional (2D) or three-dimensional (3D) image of the tissue being scanned. PD computes the power of the slow-time signal and is color-coded to indicate the presence of blood flow.

Unlike color Doppler images that is reconstructed using mean of the Doppler shift, PD uses power of the Doppler shift within the received ultrasound echo to reconstruct the image. Power Doppler image acquisition typically involves the use of a low pulse repetition frequency (PRF) to capture the strength of the Doppler signal over time, rather than the

velocity. This makes it particularly useful for visualizing slow-flowing or weakly perfused tissues, such as those in tumors. However, it does not provide directional or quantitative information about blood flow. Also, because power Doppler ultrasound is more sensitive to the detection of low flow signals, it is more susceptible to false positives, which may lead to the incorrect identification of blood flow in areas where it does not exist. On the other hand, it may also miss some areas of low flow, resulting in false negatives.

Power Doppler image acquisition is a technique that uses the power of the slow-time signal to detect moving matter, such as blood flow, in a region of interest. The slow-time signal is obtained from the returned echoes, which have a Doppler shift due to the Doppler effect. The power of the slow-time signal is mapped to a color hue according to a predefined color scale and superimposed on a B-mode image, which shows the anatomical structures of the tissue. Power Doppler image acquisition can provide more sensitive information about blood flow than color Doppler image acquisition, which uses the frequency shift of the slow-time signal.

1.2.1.1 Clutter Filtering for Power Doppler and Contrast-free Ultrasound

Contrast-free microvascular ultrasound imaging is a valuable technique used to visualize small blood vessels and blood flow in different organs and tissues. However, this type of imaging is prone to motion artifacts, noise, and echoes from tissue structures. Motion artifacts which arise from stationary tissue and other non-moving structures can obscure the detection of low-velocity blood flow making it difficult to visualize and analyze microvascular structures and blood flow. These clutter artifacts can result in false positives and reduce the sensitivity and specificity of the imaging technique. Therefore, clutter filtering techniques are necessary to improve the accuracy and reliability of power Doppler imaging.

Frequency-based clutter filtering is a commonly used method to address clutter in ultrasound imaging by removing echoes from stationary tissue structures. However, this method is not effective in microvascular imaging. One reason for this is that frequency-based clutter filtering can also remove the low-frequency signals associated with microvascular blood flow and slow blood flow signals may be mistakenly filtered out as

clutter, resulting in a loss of information and decreased sensitivity. Additionally, the clutter in microvascular ultrasound images tends to overlap with blood in both spatial and temporal (*i.e.*, frequency) domain.

This makes spatiotemporal filtering more effective than frequency-based filtering for removing clutter in microvascular ultrasound images. These methods take into account both spatial and temporal information of the microvascular ultrasound data and utilize it to differentiate between blood flow signals and stationary tissue structures. Due to the overlap of blood and clutter signals in the spatiotemporal domain, these methods are designed to selectively remove clutter without affecting the blood flow signals. This makes it possible to accurately identify and measure small blood vessels.

Several clutter filtering techniques have been proposed, including Infinite Impulse Response (IIR), Finite Impulse Response (FIR), as well as singular value decomposition (SVD) based clutter filtering methods which are discussed in the following.

1.2.1.1.1 Conventional Clutter Filtering Methods

Conventional FIR and IIR filtering methods have been widely used for clutter filtering in ultrasound imaging. FIR filters [7] have a linear phase response and are generally stable, but the problem is that a length N filter requires a Doppler ensemble with N pulses, so it slows the frame rate if N is large. On the other hand, IIR filters [8] have a nonlinear phase response and require fewer coefficients, but they can be unstable and prone to artifacts. IIR filters have steeper roll-off than FIR for a given order, but also exhibit a longer settling time. FIR filters have a short settling time but need a higher order to efficiently discriminate clutter from blood signal.

Doppler uses only time-domain (or temporal-frequency-domain) signal processing to separate blood from clutter, however, due to real-time requirements and the use of focused ultrasonic beams, the number of temporal samples available in each spatial location is low, making these filters difficult to optimize for general Doppler imaging applications. The problem of settling time can be reduced by proper initialization in the case of IIR filters, but the transient response cannot be completely canceled. Moreover, conventional FIR and

IIR clutter filtering methods do not adapt well to variations in tissue motion and clutter distribution over time, which can limit their effectiveness. Additionally, these methods often rely on assumptions about the data, such as a specific distribution of clutter, and may not perform well when those assumptions are not met. Furthermore, selecting the appropriate filter parameters, such as the filter order and cutoff frequency, can be a subjective and time-consuming process.

1.2.1.1.2 SVD-based Clutter Filtering in Contrast-Free Ultrasound

Conventional Doppler imaging often lacks sensitivity in detecting slow-flow vessels due to the short Doppler ensemble length and the inability of traditional clutter filtering techniques, which rely on high-pass temporal filtering, to differentiate between microvasculature and tissue clutter. To overcome this constraint, UMI has emerged based on Eigen-based tissue clutter filters and in some studies in combination with high frame-rate ultrasound plane wave imaging (where considerable number of Doppler ensembles within a brief timeframe acquired can enhance the sensitivity of Doppler imaging to detect slow flow signals) [9]. SVD clutter filtering can be employed on RF or IQ image sequences obtained through various methods, such as focused beam, plane wave, or diverging wave. The UMI performed based on in-phase/quadrature (IQ) cine loop of B-mode frames with the spatiotemporal SVD-based clutter filtering was applied on the long ensemble of the B-mode IQ data, to extract the blood flow signals has shown superior performance in tumor microvascular detection [10].

Eigen-based clutter filters, such as SVD, leverage the inherent distinctions in spatiotemporal properties among tissue, blood, and electronic noise, resulting in more effective clutter removal. SVD-based filtering works by decomposing the signal into orthogonal basis functions (*i.e.*, its singular values and vectors) and filtering out the singular values associated with clutter artifacts. Assuming that the acquired beam-formed RF signal with dimension of (x, z, t) , it can be reshaped as S with a dimension of $(x \times z, t)$ where x , z , and t denote the lateral, axial, and slow-time dimension (*i.e.*, the ensemble size), respectively. The SVD of Casorati matrix S can be presented as:

$$S = U\Delta V^T = \sum_{i=1}^t \gamma_i U_i V_i^T \quad (1.1)$$

where U and V are the orthonormal matrices with dimensions of $(x \times z, x \times z)$ and (t, t) , respectively. V^T is the transpose of V . U_i and V_i are the i th ($i \in [1, t]$) columns of U and V , which correspond to the spatial and temporal singular vectors, respectively. Δ is a diagonal matrix with a dimension of $(x \times z, t)$ and the diagonal values are the singular values of S in a descending order. γ_i represents the i th diagonal value. When decomposing, tissue displacements are primarily represented in the first singular values and singular vectors due to their high spatiotemporal coherence while blood signal are in lower singular values. The reason for the low blood singular values can be attributed to two factors. Firstly, the scattered power from blood is generally low because blood cells are small, and vessels tend to occupy only a small area within the region of interest (ROI). Secondly, the coherence of the blood signal is also lower, which results in the signal power being distributed across multiple singular vectors. An SVD clutter filter suppresses tissue clutter by selecting a threshold rank and attenuating the singular vectors with rank below the threshold. By setting a threshold on the singular values, the clutter subspace can be separated from the blood flow subspace, and the clutter can be effectively removed. A microvascular image is then reconstructed from the filtered data set.

Various methods for determining the rank threshold have been proposed, including a predetermined threshold based on the expected blood-to-clutter signal power ratio [11], or an adaptive threshold calculated from the slope of the singular value curve [12]. These methods employ a truncated SVD filter, where the singular values at ranks below the blood-clutter rank threshold are set to zero, and the singular values above the threshold are left unchanged. The SVD-based clutter filtering has been shown to reveal previously undetected blood flows, such as microvascular networks or blood flows corrupted by significant tissue or probe motion artifacts. Recent research has focused on developing faster and more efficient methods for SVD-based clutter filtering, such as randomized SVD [12] and block-wise adaptive SVD [13]. These methods have been shown to provide comparable clutter rejection performance to full SVD while significantly improving computational performance.

1.2.1.2 PD Quantitative and Morphological Analysis

Quantitative analysis of power Doppler ultrasound images involves the measurement of various parameters such as vessel density and tortuosity. These measurements can be obtained using specialized software tools that provide automated image analysis capabilities. The use of quantitative analysis has been shown to improve the accuracy and reproducibility of power Doppler ultrasound imaging. Morphological analysis and features in power Doppler ultrasound imaging involve the evaluation of the shape, size, and distribution of vessels in the tissue or organ being examined. Morphological features such as vessel length, branching patterns, and diameter can provide valuable information on tissue microvasculature and can be used for cancer diagnosis and treatment response evaluation [14].

PD quantitative information on blood flow is commonly used in clinical practice to assess tissue perfusion and vascularization [15-18]. The basic PD metrics include vascular index (VI), flow index (FI), and vascular flow index (VFI). VI represents the percentage of the image area that contains blood vessels, while FI quantifies the intensity of the blood flow signal. VFI is the product of VI and FI, which reflects the volume of blood flow in a given area. These metrics can be used to monitor changes in tissue vascularity, which is often associated with various pathological conditions such as cancer, inflammation, and ischemia. In addition to clinical applications, PD metrics are also used in preclinical research to evaluate the efficacy of antiangiogenic therapies or to investigate the pathophysiology of vascular diseases.

Overall, the use of perfusion parameters and morphological and quantitative analysis in power Doppler ultrasound imaging can provide valuable insights into the tissue microvasculature and aid in the diagnosis and monitoring of various diseases. However, there are still several challenges associated with the use of these techniques, such as the need for standardized protocols and the limitations of current image analysis tools.

1.2.2 Overview of Contrast-Enhanced Ultrasound Imaging

Perfusion imaging utilizing contrast-enhanced ultrasound involves the administration of a contrast agent in the form of microbubbles that enhance the signal. This is achieved by

administering the contrast agent intravenously. CEUS has several advantages over other imaging modalities, such as computed tomography (CT) and magnetic resonance imaging (MRI), including its real-time imaging capabilities, lack of ionizing radiation, and relatively low cost. CEUS involves the use of microbubble contrast agents that enhance the visualization of microvessels and allow for real-time monitoring of the microcirculation. Microbubbles are small gas-filled particles that are injected into the bloodstream and are highly reflective to ultrasound waves. CEUS has emerged as an important imaging modality in various clinical settings, including oncology [19], liver [20], kidney [21,22], and many other applications due to its ability to provide real-time, high-resolution images with excellent contrast enhancement.

1.2.2.1 CEUS Image Acquisition and Construction

Contrast-enhanced ultrasound is capable of detecting signals from the vasculature by utilizing microbubbles that have diameters measured in microns. These microbubbles significantly enhance the acoustic backscatter signal from blood. To acquire CEUS images, the ultrasound probe is placed on the surface and ultrasound waves are emitted from the probe. These waves then bounce off the contrast agent bubbles in the blood vessels and return to the probe, where they are detected and converted into an image. The imaging process is usually performed in real-time, allowing the operator to view the contrast agent flow as it occurs [23]. Contrast-enhanced ultrasound (CEUS) can be performed using two different methods: bolus enhancement and destruction-reperfusion kinematic models.

Bolus enhancement [24], is a method that involves the injection of a large quantity of indicators into the venous system, and then a series of ultrasound images are acquired over time to track the enhancement of the tissue of interest. The main advantages of bolus enhancement CEUS provide a rapid assessment of the vascularization and perfusion of the organ of interest. It is a simpler technique to use compared to destruction-reperfusion techniques since it avoids the complexities of constant infusion, such as the need for catheterization, surgical tubing, controlled flow rates, and agitation of the indicator to maintain a consistent injection concentration. Furthermore, a single bolus injection requires less total indicator and setup time compared to constant infusion. However, there are various limitations to its application in quantitative imaging such as not physiologically

feasible, particularly when considering the short time scale of contrast-enhanced ultrasound imaging. The drawback is that the contrast agent has a short half-life, so the imaging window is limited to a few minutes.

The destruction-reperfusion technique [25], that is used throughout this thesis, is a unique approach to contrast-enhanced ultrasound that differs from relying on an intravenous bolus injection of contrast agent washing into the imaging plane. Instead, it utilizes a constant infusion of microbubbles into systemic circulation and implements a high-energy ultrasound pulse to induce the complete destruction of all indicators within an acoustic window.

1.2.2.2 Statistical CEUS Analysis

Conventional CEUS image analysis overlooks important information that can be obtained from speckle statistics. Many studies have used CEUS to evaluate tumor perfusion heterogeneity, including a log-normal perfusion model, micro flow image processing, and contrast ultrasound dispersion imaging. However, these methods have limitations, such as subjectivity and a lack of spatial heterogeneity quantification.

In previous research in our lab, Lowerison, *et. al.*, [26] proposed a method for analyzing the first-order speckle statistics of sub-harmonic CEUS images from tumors using a compound distribution of exponential probability density functions. The proposed method can be used to quantify the heterogeneities of the contrast speckle pattern and characterize the microbubble concentration among vessel lumina in the tumor. The proposed method can quantify spatial heterogeneity and provide an alternative metric for assessing vascular network complexity using a single ROI encompassing the entire tumor cross section analyzed at two time points during wash-in.

The proposed model can approximate the local changes in microbubble number density, such as a high concentration microbubble bolus surrounded by a low-intensity tissue background in a contrast-specific image. It was applied to contrast-specific, amplitude-modulated, CEUS cine loops acquired from a mouse breast cancer mammary fat pad xenograft model treated with a monoclonal anti-vascular endothelial growth factor (anti-

VEGF) antibody (specifically, the murine analog to bevacizumab). The proposed method was able to detect a significant reduction in micro-vascular density due to the anti-angiogenic therapy and changes in tumor vascular complexity in response to the therapy.

In this statistical CEUS method [26], the probability density function (PDF) of the contrast-enhanced signal intensity $f(I)$, is modeled as a mixture of exponential PDFs weighted by the function $w(\theta)$,

$$f(I) = \int w(\theta)p(I|\theta)d\theta, \quad (1.3)$$

where $p(I|\theta)$ is an exponential distribution conditional on the scale parameter, θ :

$$p(I|\theta) = \theta e^{-\theta I}. \quad (1.4)$$

The study also assumes, based on [27], that an arbitrary vascular network can be simplified by assuming a fractal branching geometry that yields a distribution of vessel diameters and flow velocities governed by a log-normal distribution. Therefore, the weighting function in Eq. 1.3 may also be assumed to be log-normal. Different values of θ can be viewed as arising from different local microbubble concentrations, such that $w(\theta)$ characterizes the spatial heterogeneity of contrast enhancement in the region of interest.

The gamma family of PDFs can serve as an approximation to the log-weighting function, and use of a gamma distribution to estimate the weighting function (Eq. 1.4) leads to a Lomax distribution (Eq. 1.5) as an analytic solution for the compound speckle PDF, $f(I)$.

$$w(\theta|\alpha, \beta) = \frac{\alpha^\beta}{\Gamma(\beta)} \theta^{\beta-1} e^{-\alpha\theta} \quad (1.5)$$

where α and β are hyper-parameters. Substitution of Eq. 1.4 and Eq. 1.5 into Eq. 1.3 yields the model's approximation to the backscatter intensity distribution, a Type-II Pareto (Lomax) probability function:

$$f(I|\alpha, \beta) = \frac{\beta\alpha^\beta}{(I + \alpha)^{\beta+1}} \quad (1.6)$$

The hyper-parameters, α and β , of this compound model can be determined by applying established maximum likelihood estimators (MLE) to intensity histograms from the image sequence.

A statistical CEUS wash-in curve is constructed by analyzing the change in $w(\theta)$ during either a bolus infusion or destruction-replenishment. Wash-in time series were constructed to characterize the kinematics of contrast enhancement, and the local density random walk model (LDRW) was selected for fitting to the bolus wash-in curves [28]. In this kinematic analysis, the weighting function is a PDF to describe the expected value of the exponential speckle distribution. Areas of overlap with the baseline weighting function indicate unenhanced speckle populations. By subtracting the overlapping area from one, we obtain the weighting function discrepancy, which was plotted against time to estimate the total tracer mass in Fig. 1.1.

The model's final step is to make explicit the time-dependence of the hyper-parameters and the weighting function. Each frame in a CEUS cine loop yields a separate estimate of the hyper-parameters, and interpreting the Lomax function as a compound PDF makes the model useful for analyzing heterogeneous vascular networks. Quantitative perfusion metrics were calculated from the fitting parameters of the LDRW model to the wash-in curves. The area under the curve (AUC) of LDRW fit to the time series of the weighting function discrepancy curve, was correlated with micro-vascular density (MVD), which is a key measure of angiogenesis. This perfusion parameter is of particular interest for this study design as successful anti-angiogenic therapy would manifest predictably as a decrease in MVD in the mouse tumor model.

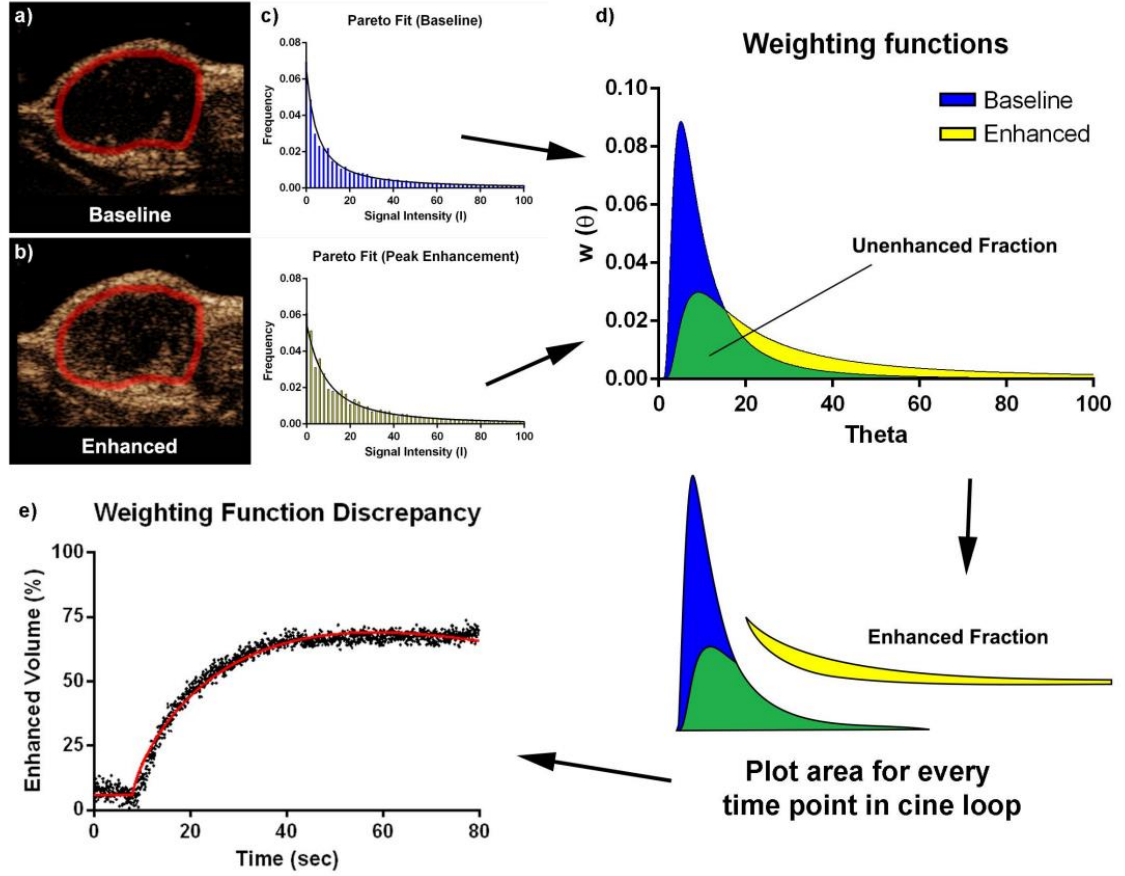


Figure 1.2: Representative CEUS tumor images (anatomical transverse plane, 14 days post inoculation) taken at (a) baseline (unenhanced) and at (b) peak bolus enhancement, with (c) corresponding Pareto fits to intensity ROI histograms, and (d) weighting functions. The change in area of overlap (yellow region) over time in (d) was used to construct wash-in curves as demonstrated in (e) [28]

Assuming that the Micro bubble (MB) concentration is high, the spatial pattern of the MBs becomes the same as the spatial pattern of the vessel and therefore this model assumes that the statistics of CEUS images can be analyzed using the same models as speckle formation in B-mode images. The backscatter intensity of microbubble populations is expressed using a weighted mixture distribution of speckle sub-regions. Parker et. al. [29], derive several probability distributions to describe the first-order statistics of speckle from soft vascularized tissues and observed that the Lomax distribution, also known as Pareto Type II distribution, describes the expected histogram distribution of echo intensities from a fractal branching set of Born cylinders. Thus, if the vascularized tissue can be described by

Lomax distribution, then the distribution for MB is Lomax as well. The weighting function of the compound distribution is assumed to belong to the gamma family of distributions, and the hyper-parameters can be determined by applying maximum likelihood estimators to intensity samples from the image. The model is useful for providing an alternative metric for assessing vascular network complexity in CEUS images.

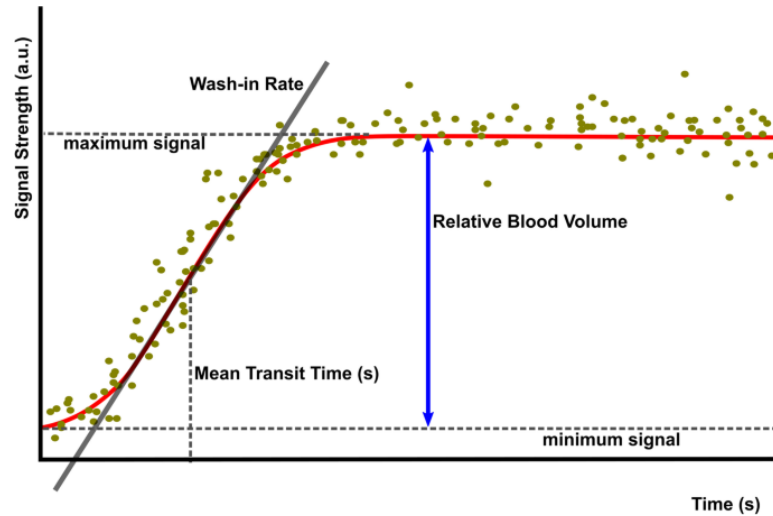


Figure 1.3: Perfusion Parameters Based on the Destruction-replenishment Time Intensity Curve [30]

1.2.2.3 Wash-in Curve Perfusion Parameters

The wash-in curve (WIC) perfusion parameters, defined in Fig. 1.2, which include peak enhancement (PE), time to peak (TTP), area under the curve (AUC), and mean transit time (MTT), are widely used in CEUS imaging to assess tissue perfusion and diagnose various pathologies. PE is the maximum enhancement reached during the first pass of the contrast agent through the tissue. It reflects the microvascular density and blood flow velocity of the tissue. TTP is the time from contrast agent injection to the maximum enhancement. It reflects the tissue's blood flow velocity and the timing of the contrast agent's arrival at the tissue. AUC is the total amount of contrast agent that passes through the tissue over time. It reflects the microvascular density, blood flow velocity, and blood volume of the tissue. MTT is the average time for the contrast agent to pass through the tissue. It reflects the blood flow velocity and the tissue's microvascular density.

Despite the promising results of WIC perfusion parameters in CEUS imaging, there are some challenges that need to be addressed. One of the challenges is the inter- and intra-observer variability in the measurements of the WIC perfusion parameters. Another challenge is the lack of standardization of the contrast agent dose and injection protocol, which may affect the WIC perfusion parameters. In addition, the correlation between WIC perfusion parameters and histopathological features is not well established, which limits their diagnostic value in some cases.

1.2.3 Utility of Quantitative Ultrasound Imaging in Cancer Research

Quantitative analysis of ultrasound microvascular imaging has emerged as a valuable tool in cancer research due to its ability to provide information on tumor vascularity and perfusion. By analyzing ultrasound images of the tumor microvasculature, researchers can extract information on blood flow, vessel density, vessel size, and other parameters that can help them understand the biology of cancer and evaluate the efficacy of anti-cancer therapies. It can provide valuable information on the microvascular architecture and function. Several microvascular parameters have been identified and studied, including vessel density, vessel diameter, and blood flow velocity. Quantitative analysis of ultrasound microvascular imaging has shown promise in different cancer applications.

One of the key applications of quantitative analysis of ultrasound microvascular imaging in cancer research is in the assessment of tumor response to therapy. By monitoring changes in tumor vascularity and perfusion following treatment, researchers can evaluate the effectiveness of anti-cancer therapies and identify patients who may benefit from alternative treatment strategies [31]. Additionally, by analyzing changes in the microvasculature over time, researchers can identify tumors that are more likely to progress and intervene before they become untreatable thus technique can be used to differentiate malignant tumors from benign ones [32] to monitor tumor progression [33].

Morphology analysis of the vessel network is another important aspect of microvascular imaging and can provide information on the complexity and organization of the microvascular network. Several morphological features of the vessel network have been studied, including vessel tortuosity, branching, and fractal dimension [14].

Overall, the application of quantitative and morphology analysis of ultrasound microvascular imaging in cancer research has the potential to improve patient outcomes by enabling more accurate diagnosis, better monitoring of treatment response, and early detection of recurrence.

1.2.3.1 Utility of Quantitative Analysis of Ultrasound Imaging in Cancer Detection

Studies have shown that quantitative analysis of power Doppler and CEUS imaging can improve the accuracy of cancer detection and characterization, particularly in difficult-to-image lesions. A study by [34] investigated the diagnostic performance of quantitative analysis of CEUS in differentiating benign and malignant breast lesions. The study found that perfusion parameters, such as time to peak and wash-in time, were significantly different between benign and malignant lesions. Furthermore, the combination of perfusion parameters with conventional B-mode ultrasound imaging improved the sensitivity and specificity of breast cancer detection. Similarly, another study [35], the author evaluated the diagnostic value of quantitative analysis of power Doppler ultrasound in differentiating benign and malignant thyroid nodules. The study found that peak intensity and time to peak were significantly different between benign and malignant nodules, and the combination of perfusion parameters with B-mode ultrasound imaging improved the diagnostic accuracy of thyroid cancer.

1.2.3.2 Utility of Quantitative Analysis of Ultrasound Imaging in Cancer Treatment Response Evaluation

In addition to cancer detection, quantitative analysis of perfusion parameters from power Doppler and CEUS imaging can also provide information on tumor response to treatment. A study by Faccia et al. [36] investigated the use of CEUS imaging in monitoring the response of hepatocellular carcinoma to treatment. The study found that changes in perfusion parameters, such as time to peak and wash-out time, were correlated with tumor response to treatment, and could be used to predict treatment outcome. For example, [12] found that quantitative parameters derived from UMI images provided significantly improved evaluation of anti-angiogenic therapy response compared to conventional power Doppler imaging. These findings suggest that quantitative analysis of perfusion parameters

from power Doppler and CEUS imaging has potential as a valuable tool for cancer detection and monitoring of treatment response.

The clutter filtering methods based on SVD are more adept at detecting smaller vessels and improving the measurement of vascular morphology parameters. On the other hand, the statistical CEUS method, which describes the change in the histogram of image intensity during microbubble wash-in, showed that it could improve the reliability of CEUS for quantifying anti-angiogenic treatment response in tumors. However, it is not clear whether these parameters are superior to those obtained from conventional analysis of PD and CEUS. As part of this thesis, the effectiveness of each perfusion parameter was evaluated separately, as well as in conjunction with parameters from traditional PD and CEUS analysis. This analysis contributed to identifying the optimal combination of features for accurately classifying the application of anti-angiogenic treatment in tumors.

1.3 Preclinical Models Employed in This Thesis

1.3.1 Chick CAM Tumor Model

Preclinical models that resemble human tumors play an essential role in cancer research [37]. Tumor models are critical tools in cancer research for understanding tumor development and response to therapies. CAM tumor model is a promising alternative to traditional in vivo animal models due to its low cost, rapid growth, and the ease of handling.

The CAM is highly vascularized and contains many growth factors and cytokines, making it an ideal site for tumor cell implantation [38]. The CAM tumor model is a well-established and widely used in vivo model for studying tumor growth, angiogenesis, and metastasis. It is based on the observation that tumors implanted on the CAM can grow and produce the required microenvironment for tumor cell growth and invasion. The chick embryo is a convenient and cost-effective alternative to traditional mouse models that has been widely used in preclinical research for studying tumor biology and angiogenesis [39, 40], metastasis [41], and drug testing [42].

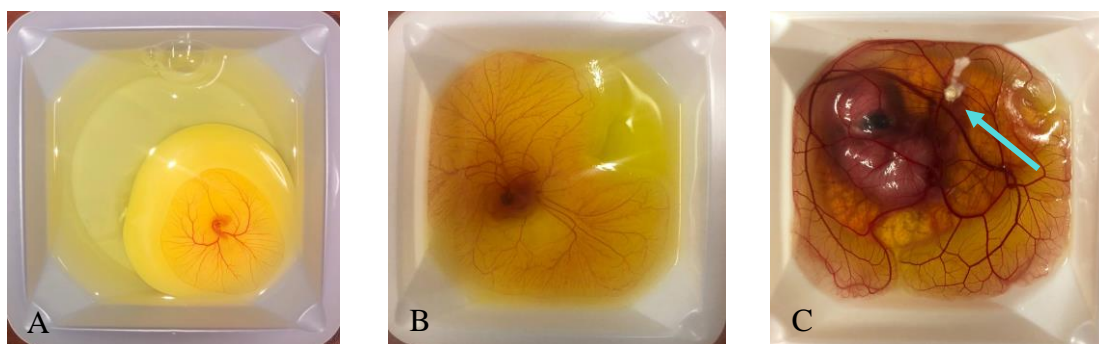


Figure 1.4: Progression of chick embryo development in weigh boat *ex-ovo* culture vessel used in this study. A shows the CAM vascular development on the 4th day of embryonic development (EDD 4), B and C are captured on EDD 10 and EDD 16 where C shows the tumor engrafted on the CAM shown by cyan arrow.

Chick CAM is easy to handle and enables direct visualization of tumor growth and angiogenesis. The CAM model can be used for both solid and liquid tumors. In this model, tumor cells are implanted onto the CAM of a chick embryo, which is then incubated for several days. The tumor cells grow and develop on the CAM, and researchers can monitor tumor growth, metastasis, and angiogenesis through non-invasive imaging techniques such as ultrasound. Both *in-ovo* and *ex-ovo* CAM models have been used to study tumor biology and angiogenesis. *In-ovo* models involve growing the tumor on the CAM within the egg, while *ex ovo* models involve growing the CAM outside the egg.

In-ovo models [43] provide a natural environment for the tumor to grow, allowing for the evaluation of the effects of the tumor on the surrounding tissue, as well as the effects of the surrounding tissue on the tumor. These models also allow for non-invasive imaging techniques, such as ultrasound, to monitor tumor growth and angiogenesis in real-time. However, they require specialized skills and equipment, and are limited by the size and number of eggs that can be used, which can impact experimental throughput.

Ex ovo models [44], shown in Fig. 1.3, which is used throughout this thesis, on the other hand, offer several advantages over *in ovo* models. They are easier to set up and do not require specialized equipment or skills. They also allow for larger numbers of tumors to be grown and monitored simultaneously, which can increase experimental throughput. *Ex ovo*

models also allow for easier access to the tumors for experimental manipulations, such as drug treatments or genetic modifications. However, they may not fully recapitulate the *in vivo* tumor microenvironment, as the tumor is not in direct contact with the chick embryo. Choosing between the two approaches depends on the specific research question and resources available, including expertise, equipment, and experimental throughput needs.

One of the key advantages of the CAM model is its ability to directly visualize the tumor and the surrounding vasculature. This is particularly relevant in studies that aim to evaluate angiogenesis and the effects of anti-angiogenic therapies. It allows for the visualization of tumor growth and vascularization in real-time, non-invasively, and with high spatial resolution. This can provide insights into the behavior of cancer cells and their interaction with the surrounding microenvironment. Furthermore, the chick CAM model can be used to study both primary and metastatic tumors, making it a useful tool for investigating the progression and spread of cancer.

Despite these advantages, the CAM model also has some limitations and challenges. One of the main challenges is the lack of an immune system in the chick embryo, which limits its ability to recapitulate the tumor microenvironment and immune response. In addition, the CAM model lacks the three-dimensional complexity of tumors and the surrounding tissue architecture, which may limit its translatability to human tumors. Additionally, the chick embryo is only able to tolerate tumor implants for a limited amount of time, which can restrict the duration of experiments. Also, if the chick can't hatch on time or they die during the experiment, it can negatively impact the experiment throughput.

Nonetheless, recent studies have shown that the CAM model can be a valuable tool for studying tumor biology and screening potential anti-cancer therapies. The CAM model has been successfully used in a variety of tumor types, including kidney cancer, and has shown promise in identifying novel anti-cancer compounds. While the CAM model has some limitations and challenges, it remains a valuable tool for cancer research.

Ultrasound imaging has several benefits for monitoring a chick CAM tumor model [45]. The non-invasive and real-time imaging capabilities of ultrasound make it an attractive tool for longitudinal studies, as multiple imaging sessions can be performed on the same animal

over time. Additionally, ultrasound can provide high spatial resolution and can be used to visualize the tumor and its surrounding vasculature in great detail. This can be especially useful for assessing the efficacy of anti-angiogenic therapies, as changes in the tumor vasculature can be observed and quantified. Overall, ultrasound imaging is a powerful tool for monitoring the development and treatment of chick CAM tumor models.

1.3.2 Mouse Hindlimb Perfusion Model

Peripheral arterial disease (PAD) is a common condition characterized by the narrowing or blockage of arteries that supply blood to the limbs. Mouse models have been widely used to study PAD due to their genetic similarity to humans and the ability to manipulate their genetic makeup. Mouse hindlimb ischemia model is commonly used for PAD, where the femoral artery is surgically ligated to induce ischemia in the hindlimb. Several mouse models have been used to study PAD, including the femoral artery ligation model [46]. In the hindlimb ischemia model, the femoral artery is surgically removed, resulting in decreased blood flow to the limb. The femoral artery ligation model involves the occlusion of the femoral artery, resulting in ischemia and tissue damage. These models have been used to study the mechanisms underlying PAD, including inflammation, oxidative stress, and angiogenesis.

Angiogenesis, the growth of new blood vessels, is a key process in the development of collateral circulation in response to ischemia. In addition to investigating underlying mechanisms, the hindlimb ischemia model has also been used to test potential therapeutic interventions for PAD. Several studies [47] have investigated the use of pro-angiogenic therapies to treat PAD, including the administration of growth factors and gene therapy.

While mouse models have been invaluable in studying the mechanisms underlying the development of PAD, there are several challenges associated with these models. One of the main challenges is the limited size of the mouse vasculature, which can make it difficult to accurately measure blood flow and assess the efficacy of therapeutic interventions. Another challenge is the high metabolic rate of mice, which can lead to rapid clearance of therapeutic compounds and limit their efficacy. In addition, the hindlimb ischemia model

relies on a surgical procedure to induce ischemia, which can introduce variability between animals and can also cause tissue damage that can confound results.

1.4 Application of Machine Learning in Ultrasound

Machine learning has become a popular tool in medical imaging, particularly in ultrasound imaging [51]. The application of machine learning in ultrasound imaging has shown promise in improving accuracy, efficiency, and diagnosis of various medical conditions, including cancer. Here is an overview of the application of machine learning in ultrasound imaging for medical and cancer applications [48-51],

1.4.1 ML in Ultrasound Image Acquisition and Reconstruction

Machine learning (ML) has shown great potential in improving the medical imaging workflow, from image acquisition and reconstruction and processing [52]. ML algorithms are widely used to enhance the quality of ultrasound images by reducing image noise and artifacts. ML has also been used to segment anatomical structures in ultrasound images, such as the liver, kidney, and heart, which can aid in the diagnosis of various diseases. Moreover, ML techniques have been used to optimize ultrasound image acquisition by automating the process of adjusting image acquisition parameters, such as gain, depth, and focal length, to obtain high-quality images [53] and also to improve the performance of beamforming [54]. In addition, ML techniques have been used to quantify ultrasound images by automatically measuring anatomical structures and identifying abnormalities.

1.4.1.1 ML in Ultrasound Image Segmentation

One of the major applications of ML in ultrasound imaging is image segmentation. Segmentation is an essential step in many clinical applications such as identifying tumors, tracking the growth of a fetus, and quantifying tissue characteristics. ML algorithms such as convolutional neural networks (CNNs) have been applied to segment ultrasound images with high accuracy and efficiency [55]. For instance, Badawy et al. [56] proposed a two-step approach that combines fuzzy logic and deep learning for automatic semantic segmentation of tumors in breast ultrasound images and showed it could enhance automatic semantic segmentation. Girum et al., [57], designed a high-performance deep learning model, combined from convolutional neural network (U-Net)-based architectures, for

segmentation of the transrectal ultrasound image. Moreover, Gulame, et al. [58], studied different thyroid nodule segmentation methods in clinical ultrasound images and showed that deep learning approaches give better performance but require more labeled data.

1.4.1.2 ML in Ultrasound Image Quality Optimization and Quantification

ML algorithms have also been used to optimize ultrasound image acquisition parameters or improve image quality [59]. Ultrasound images are affected by various factors such as noise, artifacts, and motion, which can degrade image quality and affect diagnostic accuracy. A survey on deep learning in medical image reconstruction [60] found that deep learning-based reconstruction methods improve the quality of reconstructed images qualitatively and quantitatively. However, deep learning techniques are generally computationally expensive, require large amounts of training datasets, lack decent theory to explain why the algorithms work, and have issues of robustness.

1.4.2 ML in Ultrasound Image Interpretation

Machine learning algorithms, particularly deep learning methods, have shown promise in automating and improving the accuracy of ultrasound image interpretation in cancer diagnosis in breast cancer [61], prostate cancer [62], and thyroid nodules [63]. By leveraging large datasets of ultrasound images, machine learning models can learn to identify patterns and features that are indicative of cancerous tissues, enabling more accurate and efficient diagnosis and treatment planning. Despite the promising results of these studies, there are still several challenges to be addressed in the application of machine learning to ultrasound imaging in cancer research.

One of the challenges is the lack of standardized protocols for ultrasound image acquisition and annotation, which can affect the quality and consistency of the datasets used for training and testing machine learning models. Moreover, the interpretability and transparency of machine learning models in medical imaging remain a concern, as these models often work as "black boxes" that are difficult to understand and interpret by clinicians. These issues need to be addressed in order to ensure the ethical and responsible use of machine learning in medical imaging and cancer research.

1.4.2.1 ML in Cancer Detection Using Ultrasound Imaging

In medical diagnostics, ML techniques have played a fundamental role in improving the reliability of diagnosis by reducing operator-dependence, standardizing image interpretation, providing stable results, enabling rapid decision-making, and relieving the heavy workload of radiologists. ML algorithms can be used to detect and classify tumors in ultrasound images. These algorithms use various features such as texture, shape, and intensity to differentiate between normal and abnormal tissues. Automated detection and classification of tumors can provide faster and more accurate diagnoses and reduce the risk of false-positive or false-negative results.

1.4.2.2 ML in Cancer Treatment Evaluation Using Ultrasound Imaging

One of the most common applications of machine learning in cancer treatment evaluation using ultrasound imaging is the classification of tumor response to treatment. Machine learning algorithms can analyze changes in tumor size, texture, and vascularization on ultrasound images before and after treatment, and classify tumors as responding or non-responding to the treatment. Several studies have reported high accuracy in tumor response classification using machine learning algorithms such as random forests, support vector machines, and convolutional neural networks.

Another application of machine learning in cancer treatment evaluation using ultrasound imaging is the assessment of tumor response. By analyzing ultrasound images before and after treatment, machine learning algorithms can predict the probability of tumor recurrence, metastasis, or progression. Studies have reported promising results in the prediction of treatment outcomes using machine learning algorithms such as deep learning models.

Despite the promising results, there are still several challenges in the application of machine learning to ultrasound imaging for cancer treatment evaluation. One of the main challenges is the lack of standardization in ultrasound imaging protocols and parameters. This makes it difficult to compare results from different studies and develop generalizable machine learning models. Although using simulated images has been proposed [63] to address the limited availability of annotated ultrasound images for training machine

learning models, it remains a challenges in the field. This limits the development of large-scale and accurate machine learning models [64].

1.5 Hypotheses and objectives

The overall hypothesis of this thesis is that microvascular parameters from SVD-based clutter-filtered power Doppler and statistical analysis provides additional information about tumor angiogenesis than conventional PD and CEUS analysis. To test this hypothesis, initially, we proposed a new SVD-based clutter filtering for contrast-free ultrasound imaging was proposed to enhance microvascular detection. We then proposed a pre-clinical tumor treatment response classification model which utilized quantitative perfusion features from proposed SVD-filtered reconstructed PD images, as well as those from statistical analysis and conventional analysis of CEUS and conventional analysis of PD. We evaluated the effectiveness of these features in terms of improved classification accuracy, precision, and recall. Therefore, this thesis has been divided into the following four specific technical objectives:

1. Develop and evaluate, by comparison with truncated SVD clutter filtering, an optimal shrinkage SVD-based clutter filter to improve microvascular detection and quantification of contrast-free microvascular ultrasound images.
2. Present a scalable pre-clinical *ex-ovo* chick CAM tumor model based on PD and CEUS microvascular and perfusion parameters to evaluate the tumor treatment response to anti-angiogenic therapy and determine the best approach to combine ultrasound-based microvascular features.
3. Assess the effectiveness of morphological and perfusion parameters from optimal shrinkage SVD filtered PD images and statistical analysis of CEUS to discriminate tumor treatment response to antiangiogenic therapies.
4. Evaluate the generalization of the developed model and evaluate the performance of the model in evaluating unseen tumors with unknown sensitivity to antiangiogenic therapy.

1.6 Thesis outline

The combination of microvascular ultrasound, machine learning, and CAM tumor models provided a unique opportunity to address the research question of identifying essential parameters for classifying antiangiogenic treatment sensitivity in a tumor model. The focus of this research project was to identify the optimal combination of power Doppler, contrast-free microvascular, and CEUS features required to classify the antiangiogenic treatment sensitivity of a tumor model using classical machine learning methods.

The incorporation of contrast-free microvascular imaging led to the recognition of an opportunity to enhance these images by addressing the overlap between clutter and blood-signal components in the eigen spectrum, which was solved using the optimum shrinkage SVD clutter filter introduced in Chapter 2. The effectiveness of this filter was tested in both a preclinical tumor model and mouse hindlimb perfusion, demonstrating its broad potential.

In establishing the experimental protocol for the cancer anti-angiogenesis application, the importance of including both the optimum shrinkage contrast-free images and statistical CEUS parameters was demonstrated. Chapter 3 established the essential steps in the experimental protocol for the metastatic renal cell carcinoma (mRCC) anti-angiogenesis application by demonstrating the protocol in a simplified scenario comparing a highly sensitive tumor cell line to untreated tumors. The results motivated the inclusion of both the optimum shrinkage contrast-free images and statistical CEUS parameters in subsequent studies.

Finally, Chapter 4 demonstrated that the multiparametric ultrasound approach was used to discriminate between treatment-sensitive and treatment-resistant tumor cell lines, and the machine learning model was shown to be generalizable to accurately classify the sensitivity of a third cell line that was not used to train the model. Taken together, these findings highlight the potential of microvascular ultrasound, use of CAM tumor model and machine learning to provide an effective and comprehensive ultrasound-based approach to evaluating the efficacy of antiangiogenic treatments in cancer and other diseases.

1.6.1 Chapter 2

Chapter 2 presents a clutter filtering method called optimal shrinkage SVD-based clutter filtering, to enhance the microvascular quantification in power Doppler ultrasound. This clutter filtering method was applied on both images of tumors engrafted on the CAM of chick embryo and the images of mice hindlimb where the mice underwent unilateral femoral artery and vein ligation and excision. Optimal shrinkage SVD-based clutter filtered images yields a higher-fidelity reconstruction of the microvascular network and also demonstrated Improvements in image quality. The proposed method enables the use of contrast-free microvascular imaging in applications where the detection and quantification of microvessels are essential in diagnosis and treatments.

1.6.2 Chapter 3

Chapter 2 presents a scalable preclinical platform to compare methods for classifying anti-angiogenic treatment response using ultrasound-based multiparametric microvascular imaging. The model pipeline consists of human mRCC cell lines engrafted on the CAM of *ex-ovo* chick embryo, imaged with PD and CEUS ultrasound and the microvascular parameters from conventional analysis for both PD and CEUS, the statistical analysis and microvascular parameters from optimal shrinkage SVD-based clutter filtered PD were used. The utility of the newly developed analysis were evaluated and the results showed the combination of perfusion and microvascular quantification parameters from statistical and conventional analysis can improve the accuracy, precision and sensitivity of the classification of treated sensitive cell line with Sunitinib antiangiogenic therapy (*i.e.*, Caki-1) and control group.

1.6.3 Chapter 4

Chapter 4 tested the ultrasound-based multiparametric microvascular classification model performance first with two different mRCC tumor cells with two different sensitivity levels (*i.e.*, resistant and sensitive tumors to antiangiogenic therapy). Moreover, the model using the combination of all perfusion parameters from both conventional and statistical analysis of CEUS as well as conventional and SVD-based optimal shrinkage clutter filtered PD images was compared to the model using only selected features. The cross-validation

results were promising with high classification capabilities using selected perfusion parameters in classifying sensitive from resistant tumors. The model performance analysis was then extended to testing it on an independent mRCC tumor cell (*i.e.*, 786-O). The results indicated high accuracy. It also demonstrated the potential of microvascular ultrasound as a non-invasive and promising tool for determining the sensitivity of new preclinical tumor models to anti-angiogenic treatment.

1.6.4 Chapter 5

Chapter 5 summarizes the thesis as well as a discussion of the potential future directions for this research, including technical improvements and the next steps for preclinical validation.

References

- [1] G. Montaldo, *et al.*, "Coherent plane-wave compounding for very high frame rate ultrasonography and transient elastography", *IEEE Transactions on Ultrasonics, Ferroelectrics, and Frequency Control*, vol. 56, no. 3, pp. 489-506, 2009
- [2] D. H. Evans, *et al.*, "Ultrasonic colour Doppler imaging", *Interface Focus*, vol. 1, no. 4, pp. 490–502, 2011
- [3] M. U. Aziz, *et al.*, "Microvascular Flow Imaging: A State-of-the-Art Review of Clinical Use and Promise", *Radiology*, vol. 305, no.2, pp. 250-264, 2022
- [4] J. Bercoff, *et al.*, "Ultrafast compound doppler imaging: providing full blood flow characterization", *IEEE Transactions on Ultrasonics, Ferroelectrics, and Frequency Control*, vol. 58, no. 1, pp. 134-147, January 2011
- [5] G. S. Lin, *et al.*, "Power Doppler: How It Works, Its Clinical Benefits, and Recent Technologic Advances", *Journal of Diagnostic Medical Sonography*, 1998,
- [6] J.A. Zeller, *et al.*, "Color flow Doppler versus power Doppler imaging in the examination of vertebral arteries", *European Journal of Ultrasound*, vol. 5, no. 3, pp. 133-13, 1997
- [7] J. C. Willemetz, *et al.*, "Bias and variance in the estimate of the Doppler frequency induced by a wall motion filter", *Ultrasonnd Imaging*, vol. 11, no. 3, pp. 215–225, Jul. 1989.
- [8] C. Tysoe, *et al.*, "Bias in mean frequency estimation of Doppler signals due to wall clutter filters", *Ultrasound in Medicine and Biology*, vol. 21, no. 5, pp. 671–677, 1995.
- [9] C. Dmené, *et al.*, "Spatiotemporal Clutter Filtering of Ultrafast Ultrasound Data Highly Increases Doppler and fUltrasound Sensitivity", *IEEE Transactions on Medical Imaging*, vol. 34, no. 11, pp. 2271-2285, Nov. 2015
- [10] C. Huang, *et al.*, "Noninvasive Contrast-Free 3D Evaluation of Tumor Angiogenesis with Ultrasensitive Ultrasound Microvessel Imaging", *Science Reports*, 9, 4907, 2019
- [11] J. Baranger, *et al.*, "Adaptive Spatiotemporal SVD Clutter Filtering for Ultrafast Doppler Imaging Using Similarity of Spatial Singular Vectors", *IEEE Transactions on Medical Imaging*, vol. 37, no. 7, pp. 1574-1586, July 2018
- [12] P. Song, *et al.*, "Ultrasound Small Vessel Imaging With Block-Wise Adaptive Local Clutter Filtering", *IEEE Transactions on Medical Imaging*, vol. 36, no. 1, pp. 251-262, Jan. 2017
- [13] P. Song, *et al.*, "Accelerated Singular Value-Based Ultrasound Blood Flow Clutter Filtering With Randomized Singular Value Decomposition and Randomized Spatial Downsampling", *IEEE Transactions on Ultrasonics, Ferroelectrics, and Frequency Control*, vol. 64, no. 4, pp. 706-716, April 2017

- [14] S. Ghavami, *et al.*, "Quantification of Morphological Features in Non-Contrast-Enhanced Ultrasound Microvasculature Imaging", *IEEE Access*, vol. 8, pp. 18925-18937, 2020
- [15] W. Sun, *et al.* "Three-dimensional power Doppler ultrasound evaluation of placental blood flow in normal monochorionic diamniotic twin pregnancies", *BMC Pregnancy Childbirth*, 18, 443, 2018
- [16] J.C. Hsu, *et al.*, "Quantitative analysis of normal fetal brain volume and flow by three-dimensional power Doppler ultrasound", *Journal of the Chinese Medical Association*, Volume 76, Issue 9, Pages 504-509, 2013
- [17] P.Y. Tsai, C. H. Chang, "Assessment of the blood flow in kidneys of growth-restricted fetuses using quantitative three-dimensional power Doppler ultrasound", *Taiwanese Journal of Obstetrics and Gynecology*, vol 57, no. 5, 2018
- [18] M.J.N.C. *et al.*, "Evaluation of volume vascularization index and flow index: a phantom study", *Ultrasound Obstet Gynecol*, 32: 560-564, 2008
- [19] Q. Cui, *et al.*, "Contrast-enhanced ultrasound-guided sentinel lymph node biopsy in early-stage breast cancer: a prospective cohort study", *World Journal of Surgical Oncology*, 21, 143, 2023
- [20] J. Zhou, *et al.*, "Feature Fusion for Diagnosis of Atypical Hepatocellular Carcinoma in Contrast- Enhanced Ultrasound", *IEEE Transactions on Ultrasonics, Ferroelectrics, and Frequency Control*, vol. 69, no. 1, pp. 114-123, Jan. 2022
- [21] H.E. Yoon, *et al.*, "A pilot trial to evaluate the clinical usefulness of contrast-enhanced ultrasound in predicting renal outcomes in patients with acute kidney injury", *PLOS ONE* vol. 15, no. 6, 2020
- [22] M. Bertolotto, *et al.*, "Contrast-enhanced ultrasound for characterizing renal masses", *European Journal of Radiology.*, vol. 105, pp. 41-48, Aug. 2018
- [23] S. Otis, *et al.*, "Contrast-Enhanced Transcranial Imaging", *Stroke Journal*, vol. 26, no. 2, pp. 203-209, 1995
- [24] C. Strouthos, *et al.*, "Indicator dilution models for the quantification of microvascular blood flow with bolus administration of ultrasound contrast agents", *IEEE Transactions on Ultrasonics, Ferroelectrics, and Frequency Control*, vol. 57, no. 6, pp. 1296–1310, 2010
- [25] K. Wei, *et al.*, "Quantification of Myocardial Blood Flow With Ultrasound-Induced Destruction of Microbubbles Administered as a Constant Venous Infusion," *Circulation*, vol. 97, no. 5, pp. 473–483, Feb. 1998
- [26] M.R. Lowerison, *et al.*, "Compound speckle model detects anti-angiogenic tumor response in preclinical nonlinear contrast-enhanced ultrasonography", *Med. Phys.*, vol. 44, pp. 99-111, 2017

- [27] H. Qian, J. B. Bassingthwaite, "A Class of Flow Bifurcation Models with Lognormal Distribution and Fractal Dispersion", *Journal of Theoretical Biology*, vol. 205, no. 2, pp. 261-268, 2000
- [28] K. H. Norwich and S. Zelin, "The dispersion of indicator in the cardio-pulmonary system", *Bull. Math Biophys.*, vol. 32, no. 1, pp. 25–43, Mar. 1970.
- [29] K.J. Parker, S.S. Poul, "Burr, Lomax, Pareto, and Logistic Distributions from Ultrasound Speckle", *Ultrason Imaging*. Vol. 42 no. 4, pp.203-212. Epub, Jun. 2020
- [30] J. Watchorn, *et al.*, "Decreased renal cortical perfusion, independent of changes in renal blood flow and sublingual microcirculatory impairment, is associated with the severity of acute kidney injury in patients with septic shock", *Crit Care*, 26, 261 (2022).
- [31] F. Lin, *et al.*, "3-D Ultrasound Localization Microscopy for Identifying Microvascular Morphology Features of Tumor Angiogenesis at a Resolution Beyond the Diffraction Limit of Conventional Ultrasound", *Theranostics.*, vol. 7, no. 1, pp. 196–204, 2017
- [32] S. Kupesic, B.M. Plavsic, "Early ovarian cancer: 3-D power Doppler", *Abdom Imaging.*, vol. 31, no. 5, Sep-Oct 2006
- [33] N. Matsumoto, *et al.*, "Quantitative Ultrasound Image Analysis Helps in the Differentiation of Hepatocellular Carcinoma (HCC) From Borderline Lesions and Predicting the Histologic Grade of HCC and Microvascular Invasion". *Journal Ultrasound Medicine.*, Apr 2021
- [34] M. Wubulhasimu, *et al.*, "The added value of contrast-enhanced ultrasound to conventional ultrasound in differentiating benign and malignant solid breast lesions: a systematic review and meta-analysis". *Clinical Radiology.*, vol. 73, no. 11, pp. 936-943, Nov. 2018
- [35] A. Cansu, *et al.*, "Diagnostic value of 3D power Doppler ultrasound in the characterization of thyroid nodules", *Turkish Journal of Medical Sciences.*, vol. 18, no. 3, pp. 723-729, Jun. 2019
- [36] M. Faccia, *et al.*, "Contrast-Enhanced Ultrasound for Monitoring Treatment Response in Different Stages of Hepatocellular Carcinoma", *Cancers*, vol. 14, no. 3, p. 481, Jan. 2022
- [37] C. A. Tufan, *et al.*, "The Chick Embryo Chorioallantoic Membrane as a Model System for the Study of Tumor Angiogenesis, Invasion and Development of Anti-Angiogenic Agents", *Current Cancer Drug Targets*, vol. 5, no. 4, 2005
- [38] P. Nowak-Sliwinska, *et al.*, "The chicken chorioallantoic membrane model in biology, medicine and bioengineering", *Angiogenesis*, vol. 17, 779–804, 2014
- [39] D. Ribatti, "The chick embryo chorioallantoic membrane as a model for tumor biology", *Experimental Cell Research*, vol. 328, no. 2, pp. 314-324, 2014

- [40] D. Ribatti, "The chick embryo chorioallantoic membrane in the study of tumor angiogenesis", *Romanian Journal of Morphology and Embryolog*, vol. 49, no. 2, pp.131–135, 2008
- [41] D. Ribatti, "The CAM assay in the study of the metastatic process", *Experimental Cell Research*, vol 400, no. 2, 2021
- [42] D. Ribatti, "The Chick Embryo Chorioallantoic Membrane as an In Vivo Assay to Study Antiangiogenesis," *Pharmaceuticals*, vol. 3, no. 3, pp. 482–513, Mar. 2010,
- [43] M. Li, *et al.*, "Chick Chorioallantoic Membrane (CAM) Assay as an Efficient Xenograft Model of Hepatocellular Carcinoma", *Journal of Visualized Experiments*, vol. 104, 2015
- [44] D. S. Dohle, *et al.*, "Chick ex ovo Culture and ex ovo CAM Assay: How it Really Works ", *Journal of Visualized Experiment*, vol. 33, no. 1620, Nov 2009
- [45] M.R. Lowerison, *et al.* "Ultrasound localization microscopy of renal tumor xenografts in chicken embryo is correlated to hypoxia". *Scientific Reports*, vol. 10, no. 2478, 2020
- [46] H. Niiyama, *et al.*, "Murine model of hindlimb ischemia", *Journal of Visualization Experiments*, vol 23, no. 1035., 2009 Jan
- [47] K. Petrak, *et al.*, "Challenges in Translating from Bench to Bed-Side: Pro-Angiogenic Peptides for Ischemia Treatment". *Molecules.*, vol. 24,7, no. 1219, Mar. 2019
- [48] L. J. Brattain, *et al.*, "Machine learning for medical ultrasound: status, methods, and future opportunities", *Abdominal Imaging*, vol. 43, no. 4, pp. 786–799, 2018.
- [49] Y.T. Shen, *et al.*, "Artificial intelligence in ultrasound", *European Journal of Radiology*, vol. 139, no. 109717, Jun. 2021
- [50] S. Liu, *et al.*, "Deep Learning in Medical Ultrasound Analysis: A Review", *Engineering*, vol. 5, no. 2, 2019
- [51] M. Micucci and A. Iula, "Recent Advances in Machine Learning Applied to Ultrasound Imaging", *Electronics*, vol. 11(11), no. 1800, Jun. 2022,
- [52] B. Luijten, *et al.*, "Ultrasound Signal Processing: From Models to Deep Learning", *arXiv:2204.04466*
- [56] R. J. G. van Sloun, *et al.*, "Deep Learning in Ultrasound Imaging," *Proceedings of the IEEE*, vol. 108, no. 1, pp. 11-29, Jan. 2020
- [54] A. C. Luchies and B. C. Byram, "Deep Neural Networks for Ultrasound Beamforming," *IEEE Transactions on Medical Imaging*, vol. 37, no. 9, pp. 2010-2021, Sept. 2018

- [55] Z. Wang, "Deep Learning in Medical Ultrasound Image Segmentation: a Review", *arXiv:2002.07703*
- [56] S. Badawy, *et al.*, "Automatic semantic segmentation of breast tumors in ultrasound images based on combining fuzzy logic and deep learning—A feasibility study", *PLoS ONE*, vol. 16, 2021
- [57] K. Girum, *et al.*, "A deep learning method for real-time intraoperative US image segmentation in prostate brachytherapy", *International Journal of Computer Assisted Radiology and Surgery*, vol. 15, pp. 1467–1476, 2020
- [58] M. Gulame, *et al.*, "Thyroid nodules segmentation methods in clinical ultrasound images: A review", *Journal of Material Today: Proceeding*, vol. 45, pp. 2270–2276, 2021
- [59] A. Ilesanmi, *et al.*, "A method for segmentation of tumors in breast ultrasound images using the variant enhanced deep learning", *Biocybernetic and Biomedical Engineering*, vol. 41, pp. 802–818, 2021
- [60] E.I Ahishakiye, *et al.*, "A survey on deep learning in medical image reconstruction", *Intelligent Medicine*, vol. 1, no. 3, pp. 118-127, 2021
- [61] W. -X. Liao, *et al.*, "Automatic Identification of Breast Ultrasound Image Based on Supervised Block-Based Region Segmentation Algorithm and Features Combination Migration Deep Learning Model", *IEEE Journal of Biomedical and Health Informatics*, vol. 24, no. 4, pp. 984-993, Apr. 2020
- [62] Y. Feng, *et al.*, "A Deep Learning Approach for Targeted Contrast-Enhanced Ultrasound Based Prostate Cancer Detection," *IEEE/ACM Transactions on Computational Biology and Bioinformatics*, vol. 16, no. 6, pp. 1794-1801, Dec. 2019
- [63] H. Zhou, *et al.*, "Online Transfer Learning for Differential Diagnosis of Benign and Malignant Thyroid Nodules With Ultrasound Images," *IEEE Transactions on Biomedical Engineering*, vol. 67, no. 10, pp. 2773-2780, Oct. 2020
- [64] A. C. Luchies, B. C. Byram, "Training improvements for ultrasound beamforming with deep neural networks", *Phys. Med. Biol.* 64 045018, 2019

Chapter 2

2 Contrast-Free Ultrasound Microvascular Imaging with Optimal Shrinkage Clutter Filtering to Enhance Vascular Quantification

The contents of this chapter have been adapted from

*"Contrast-Free Ultrasound Microvascular Imaging With Optimal Clutter Shrinkage to Enhance Tumor Vascular Quantification", published in IEEE International Ultrasonics Symposium (IUS), 2020, Las Vegas, NV, USA, pp. 1-4, by M. Bataghva, D. Johnston, N. Power, S. Penuela and J. C. Lacefield**

&

"Optimal Shrinkage Clutter Filtering to Enhance Vascular Quantification of Contrast-Free Ultrasound Microvascular Imaging" under preparation for IEEE Transactions on Medical Imaging by M. Bataghva, F. Serack, C. Leclerc, D. Johnston, D. Hess, L. Flynn, N. Power, S. Penuela and J. C. Lacefield

*© 2020 IEEE. Reprinted, with permission, from M. Bataghva, D. Johnston, N. Power, S. Penuela and J. C. Lacefield, "Contrast-Free Ultrasound Microvascular Imaging With Optimal Clutter Shrinkage to Enhance Tumor Vascular Quantification", IEEE International Ultrasonics Symposium (IUS), Las Vegas, NV, USA, pp. 1-4

2.1 Introduction

Ultrasonic power Doppler imaging is widely used to visualize small, slow-flow blood vessels without injected contrast media in applications such as imaging of tumor angiogenesis or musculoskeletal perfusion. However, the sensitivity of power Doppler for microvascular detection and quantification is limited by the overlap of the blood and tissue signal components in the Doppler spectrum. In the last decade, the performance of contrast-free ultrasound for microvessel detection was significantly improved by the introduction of eigen-based clutter filtering, with SVD being the most commonly employed eigen filtering method. Singular value decomposition separates the echo signal into a set of orthogonal singular vectors, where the low-rank, high singular value components contain primarily the tissue signal and the higher-rank, lower singular value components contain primarily the blood signal and electronic noise [1]. An SVD clutter filter selects a threshold rank and attenuates the singular vectors with rank below the threshold to suppress tissue clutter. Singular vectors with rank above a second, higher threshold may also be attenuated to suppress noise. A microvascular image is then reconstructed from the intermediate-rank singular vectors that are retained.

Various approaches to determining the rank threshold have been described in the context of SVD clutter filtering. Some methods use a predetermined threshold based on the expected ratio of blood to clutter signal power [2], while other methods use an adaptive threshold computed from the slope of the singular value curve [3]. A common feature of these methods is that they employ a truncated SVD filter, *i.e.*, the singular values at ranks below the blood-clutter rank threshold are set to zero and the singular values above the threshold are left unaltered. However, many investigators have speculated that the blood and tissue signal components overlap in the eigen spectrum in a manner analogous to their overlap in Doppler frequency; see, *e.g.*, [4, Fig. 5]. Empirical evidence for this hypothesis was provided by Waraich *et al.* [5], who used k-means clustering to label each singular vector as arising from blood, clutter, or noise and concluded that blood and clutter singular vectors may interleave at intermediate ranks. However, like the truncated SVD methods, [5] treated each singular vector as representing only one of the three signal components.

In this Study, we instead smoothly taper the singular values over the ranks where the blood and clutter signal components are assumed to overlap via a process known as singular value shrinkage. We demonstrate that singular value shrinkage retains contributions from more singular vectors in the filtered image, while reducing the weighting of singular vectors at ranks above the rank threshold in a typical truncated SVD clutter filter and yields a higher-fidelity reconstruction of the microvascular network. To implement this approach, we adopt an optimal singular value shrinkage function that was derived by Gavish and Donoho [6-7] for generic signal denoising and repurpose their method for clutter filtering of microvascular ultrasound image sequences.

In the context of biomedical imaging, Gavish and Donoho’s formulation for optimal singular value shrinkage has been applied to denoise channel data in diffusion-weighted magnetic resonance imaging (DW-MRI) [8] and to denoise magnitude signals in functional MRI [9]. Other comparable adaptive methods for singular value shrinkage have also been evaluated for DW-MRI [10] and for speckle reduction in B-mode optical coherence tomography (OCT) [11-12]. In each of those MRI or OCT applications, the objective was to eliminate higher-rank singular vectors containing unresolvable features or noise to improve visualization of low-rank, resolvable structures. Our approach differs in that it reverses the singular value shrinkage process, *i.e.*, we instead attenuate the lowest-rank singular vectors to enhance detection of the blood signal contained in the intermediate-rank singular vectors.

We introduced our optimal shrinkage SVD clutter filter in a previous conference presentation [13]. We compared the microvessel detection performance of the optimal shrinkage clutter filter to a truncated SVD filter in images acquired from a preclinical tumor model implanted in the CAM of *ex ovo* chicken embryos. The performance measures assessed the depiction of microvascular structural features, *i.e.*, the number of vessels, number of branching points, and mean vessel length, that were estimated by skeletonization of filtered microvascular images. The current paper substantially extends the preliminary results in [13].

Section II presents a more complete description of Gavish and Donoho's optimal shrinkage function and its applicability to microvascular ultrasound. In the experimental portion of the paper (Sect. III-IV), we supplement the CAM tumor model with images of hindlimb muscle perfusion in a mouse model of peripheral arterial disease. The hindlimb provides a more challenging microvessel detection task than a CAM tumor model due to the effect of the intervening tissue layers on tissue clutter and signal attenuation in the hindlimb. We also complement the microvascular structural features by reporting image quality metrics; specifically, the intravascular signal-to-noise ratio (SNR) and the contrast-to-noise ratio (CNR) of the vessel network are compared for both applications.

2.2 Theory of Optimal Shrinkage

2.2.1 Principals of Optimal Shrinkage

Gavish and Donoho [6,7] considered the signal denoising task of estimating a low-rank signal, X , from an $m \times n$ matrix of data $Y = X + \sigma Z$, where the elements of Z are independent, identically distributed noise samples with zero mean and unit variance and σ is the noise scaling. A truncated SVD estimate of X may be expressed as:

$$\hat{X}_r = \sum_{i=1}^r y_i \mathbf{v}_i \tilde{\mathbf{v}}_i', \quad (2.1)$$

where \mathbf{v}_i and $\tilde{\mathbf{v}}_i'$ are the left and right singular vectors of Y with corresponding singular values y_i and $r < m \leq n$ is the rank threshold. The value of r may be specified directly, or it may be determined by first specifying a singular value threshold, y_{th} , in which case r is the highest rank for which $y_i \geq y_{th}$. In comparison, a singular value shrinkage estimate of X may be expressed as:

$$\hat{X}_\eta = \sum_{i=1}^m \eta(y_i) \mathbf{v}_i \tilde{\mathbf{v}}_i', \quad (2.2)$$

where $\eta(y_i)$ is a *shrinkage function* defined such that $0 \leq \eta(y_i) \leq y_i$. The truncated SVD method can be considered a special case of singular value shrinkage with $\eta(y_i) = y_i$ for $i \leq r$ (or, equivalently, for $y_i \geq y_{th}$) and $\eta(y_i) = 0$ otherwise.

Gavish and Donoho derived three forms of an optimal shrinkage function, $\eta_{opt}(y_i)$, that minimize different loss functions. Our method applies the optimal shrinkage function that minimizes Frobenius norm loss,

$$L_{m,n}^{Fro}(X, \hat{X}) = \|X - \hat{X}\|^2 = \sum_{i=1}^m \sum_{j=1}^n |X_{i,j} - \hat{X}_{i,j}|^2. \quad (2.3)$$

We chose the Frobenius norm formulation for our proof-of-concept experiments because that loss function yields singular value shrinkage that is intermediate in aggressiveness compared to the other loss functions considered in [7], operator norm loss and nuclear norm loss [7, Fig. 1]. Our intention in choosing an intermediate level of shrinkage was to obtain filtered images that are meaningfully different from the microvascular images produced using truncated SVD methods while still maintaining consistent visualization of larger vessels to permit truncated SVD filtering to be used as a performance benchmark for the optimal shrinkage method.

The optimal shrinkage function under Frobenius norm loss for the signal denoising task with an assumption of “natural” noise scaling, *i.e.*, $\sigma = \sigma_{nat} = 1/\sqrt{n}$, is given by [7, (7)]:

$$\eta_{opt}(y_i) = \begin{cases} \frac{1}{y_i} \sqrt{(y_i^2 - \beta - 1)^2 - 4\beta} & y_i \geq 1 + \sqrt{\beta} \\ 0 & y_i < 1 + \sqrt{\beta} \end{cases}, \quad (2.4)$$

where $\beta = m/n$ is the aspect ratio of the data matrix. Equation (2.4) is an asymptotic result for the limit $n \rightarrow \infty$ with β held constant that was shown numerically in [7] to yield accurate results for practically sized data matrices of $m = 50$ or 100 samples. Observe in (4) that the singular value threshold is $1 + \sqrt{\beta}$. This result arises because, under the assumptions stated thus far, the histogram of singular values possesses a “bulk edge” near $y_i = 1 + \sqrt{\beta}$ such that there are only a few, widely separated singular values greater than $1 + \sqrt{\beta}$ and the slope of the singular value curve changes dramatically as it crosses this threshold (see, *e.g.*, the numerical example in [7, Fig. 3]). Gavish and Donoho’s analysis therefore yields a singular value threshold that is comparable to the adaptive thresholds computed from the slope of the singular value curve in truncated SVD methods for

microvascular ultrasound, such as [1]. If the noise level, either assumed *a priori* or estimated from the data, is denoted by $\hat{\sigma}$ and differs from σ_{nat} , the optimal shrinkage method involves first scaling the data matrix by $\sigma_{nat}/\hat{\sigma}$, computing $\eta_{opt}(y)$ by applying (2.4) to the scaled singular values, and then rescaling the shrinkage function by multiplying it by $\hat{\sigma}/\sigma_{nat}$ before substituting it into Eq. (2.2). The scaling and rescaling steps make the effective singular value threshold $(\hat{\sigma}/\sigma_{nat})(1 + \sqrt{\beta})$.

Gavish and Donoho also outlined a method to estimate the noise scaling from the data matrix [7, (47)]:

$$\hat{\sigma} = \frac{med(y)}{\sqrt{n\mu_\beta}} = \sigma_{nat} \frac{med(y)}{\sqrt{\mu_\beta}}, \quad (2.5)$$

where $med(y)$ is the median singular value of Y and μ_β is the median of the Marchenko-Pastur distribution, which is the theoretical probability density function of singular values for the covariance matrix of independent, identically distributed noise samples (see [14] for a more detailed review in a medical imaging context). The median singular value is a convenient reference for estimating the noise scaling because the assumption that X is low rank implies that $med(y)$ will correspond to a purely noise component of Y . The Marchenko-Pastur distribution is bounded within the range $[\sigma^2(1 - \sqrt{\beta})^2, \sigma^2(1 + \sqrt{\beta})^2]$, so this noise model is also the basis for the singular-value threshold applied in (4).

2.2.2 Application to Contrast-free Microvascular Ultrasound

In microvascular ultrasound, a Casorati data matrix, Y_{Cas} , is constructed from a sequence of m beamformed radio-frequency images consisting of n pixels each, such that the m rows of Y_{Cas} correspond to the time dimension and the n columns correspond to the spatial dimension. The data can be viewed as a superposition of a tissue clutter component, C , that possesses relatively high coherence with a lower-coherence blood signal component, B , and incoherent electronic noise, N :

$$Y_{Cas} = C + \sigma_B B + \sigma_N N = C + \sigma_B \left(B + \frac{\sigma_N}{\sigma_B} N \right), \quad (2.6)$$

where σ_B and σ_N are the blood-to-clutter and noise-to-clutter ratios, respectively. Application of (2) and (4) to Y_{Cas} will isolate the most coherent data component, thus yielding $\hat{X}_\eta \approx C$. Since an image of B is desired, our method subtracts \hat{X}_η from Y_{Cas} to estimate the term in parentheses on the right-hand side of (6), which we denote as \hat{Z}_η .

$$\hat{Z}_\eta \approx B + \frac{\sigma_N}{\sigma_B} N. \quad (2.7)$$

This estimator, which is the foundation of our clutter filtering method, can be expressed using (2) and (4) as:

$$\hat{Z}_\eta = Y_{Cas} - \hat{X}_\eta = \sum_{i=1}^m \left(y_i - \frac{\hat{\sigma}_B}{\sigma_{nat}} \eta_{opt} \left(\frac{\sigma_{nat}}{\hat{\sigma}_B} y_i \right) \right) \mathbf{v}_i \tilde{\mathbf{v}}'_i. \quad (2.8)$$

The blood-to-clutter ratio cannot be expected to exhibit natural scaling, so (8) incorporates an estimate of the blood-signal scaling, $\hat{\sigma}_B$, to rescale the shrinkage function as outlined in sub section 2.2.1. The experiments presented in this paper were performed using high-frequency (40 MHz) ultrasound, for which blood exhibits a relatively high backscatter intensity [15], so, in the present studies, we assume $\sigma_B \gg \sigma_N$ and therefore $\hat{Z}_\eta \approx B$. The assumption of a favorable blood-to-noise ratio is particularly appropriate for chick CAM tumor models [16] like the samples imaged in our first set of experiments. Alternatively, for applications where the blood-to-noise ratio is lower, an improved estimate of B can be obtained by applying either (2.1) or (2.2) to denoise \hat{Z}_η , thereby isolating B as it is the more coherent component of \hat{Z}_η .

2.3 Methods and Materials

2.3.1 Ex Ovo CAM Tumor Model

Caki-1 kidney tumor cells (American Type Culture Collection, Manassas, VA) were engrafted onto *ex-ovo* chick CAMs following the protocol described in [17]. Briefly, fertilized chicken eggs (McKinley Hatchery, St. Mary's, ON, Canada) were incubated in a rotating incubator for 3 days and chick embryos were transferred from their shells into laboratory weigh boats on the third day of embryonic development (EDD-3) and maintained at 37°C in a humid incubator for seven more days. On EDD-10, Caki-1 cells

were suspended in Matrigel at a concentration of 10^6 cells per 10 μ L. An abrasion was made using sterile filter paper near a branching vessel of the chick CAM and 10 μ L of the Matrigel/cell mixture was pipetted onto the abraded area. Embryos were immediately returned to the incubator after cancer cell engraftment. The images reported in this paper depict control tumors from a larger treatment-response study [18] in which dimethyl sulfoxide (DMSO) diluted to 1:1000 in phosphate-buffered saline was used as a vehicle control. Starting on EDD-12, tumors were treated daily with a topical application of 5 μ L of the DMSO solution. Tumors were imaged in cross-sectional planes through their centers on EDD-18. Data was acquired from 22 tumors.

2.3.2 Murine Peripheral Arterial Disease Model

All hindlimb perfusion experiments were performed using 8- to 10-week-old NOD.CB17-*Prkdc*^{scid}/*J* mice (stock # 001303, Jackson Laboratories, Bar Harbor, ME). To induce hindlimb ischemia, the mice underwent unilateral femoral artery and vein ligation and excision. Ultrasound imaging was performed 35 days after vessel ligation, by which time muscle perfusion is partially restored via angiogenesis induced by the injection of hematopoietic progenitor cells within human decellularized adipose tissue. During imaging, mice were anesthetized using isoflurane mixed with oxygen (4% isoflurane/oxygen, flow rate = 0.5–1.5 L/min) and placed in the supine position on a 37 °C heating pad (FujiFilm VisualSonics Inc, Toronto, ON). The hindlimb was scanned along a longitudinal cross section in a plane just lateral to the femur. Data was acquired from 8 mice. All protocols followed in the murine experiments were approved by the Western University Animal Use Subcommittee.

2.3.3 Contrast-Free Microvascular Imaging

A Vevo 2100 ultrasound system (FujiFilm VisualSonics) equipped with digital radio-frequency (RF) mode was used to acquire beamformed, quadrature demodulated (IQ) echo signals. Two-dimensional power Doppler and B-mode image sequences, $m = 100$ frames in duration, were acquired using focused-beam scanning with a 40 MHz linear array (MS-550D, FujiFilm VisualSonics). The IQ data included both B-mode and power Doppler data (9 pulses per Doppler ensemble) in an interleaved manner, *i.e.*, one frame of B-mode data

was acquired following each Doppler ensemble. The B-mode frame rate range was different for tumor images and hindlimb images. For hindlimb images, larger field of view (FOV) was required resulted in lower frame rate range of 13-18 Hertz (Hz) than for tumor application with smaller FOV slightly larger frame rate range of 24-30 Hz.

SVD-based clutter filtering was applied offline to the B-mode IQ data using either the optimal shrinkage clutter filter or a truncated SVD clutter filter implemented in MATLAB (version R2019a, The MathWorks, Natick, MA). Casorati matrices were constructed for rectangular ROIs that were manually defined to enclose the tumor or hindlimb muscles. The ROIs were 172-223 by 98-124 pixels in the tumor images and 190-247 by 180-221 pixels in the hindlimb images, so the aspect ratio, β , of the Casorati matrices was 0.0035-0.0054 in the tumor images and 0.0020-0.0029 in the hindlimb images. Optimal shrinkage clutter filtering used (8) with the shrinkage function, $\eta_{opt} \left(\frac{\sigma_{nat}}{\hat{\sigma}_B} y_i \right)$, defined as in (4) and the blood-signal scaling, $\hat{\sigma}_B$, estimated using (5) and a numerical evaluation of μ_β that is posted as a MATLAB code supplement to [19]. Truncated SVD clutter filtering was implemented as:

$$\hat{Z}_r = \sum_{i=r+1}^m y_i \mathbf{v}_i \tilde{\mathbf{v}}_i', \quad (2.9)$$

where the rank threshold, r , was identified as the rank at which the singular value curve begins to flatten:

$$r = \operatorname{argmin}(y_i - y_{i+1} \leq \alpha). \quad (2.10)$$

In (10), α is a predefined threshold based on an empirically estimated blood-to-clutter power ratio. The threshold is calculated based on the gradient of the singular value curve shown to identify a turning point from which the curve begins to flatten. The estimated threshold, α , is 8 ± 3 for tumor images and is 14 ± 4 for hindlimb images. After clutter filtering, contrast-free microvascular images were constructed by rearranging \hat{Z}_η or \hat{Z}_r into a sequence of 100 two-dimensional IQ images and summing the signal power of each pixel over all frames. Signal powers were displayed in the same format as a power Doppler image using a color heatmap with logarithmic scaling.

2.3.4 Morphological Analysis of Vessel Networks

Vascular skeletonization was applied to the signal power images in a manner similar to [20] to obtain objective comparisons of the effectiveness of each SVD clutter filter for detection of fine details of vessel networks. A subset of the morphological filtering operations described in [20] were used to prepare the images for skeletonization. Specifically, we applied a top-hat low-pass spatial filter to smooth the power values followed by image binarization, morphological opening (*i.e.*, erosion then dilation) to remove small or thin features that were not definitively vessels, and finally centerline extraction. Skeletonization was performed in ImageJ.

Quantitative descriptors of the vascular morphology depicted in each vascular skeleton were computed by recursively traversing the skeleton. The morphological features measured were the number of vessels (NV), the number of vessel branching points (NB), and the mean vessel length (VL) in rectangular ROIs corresponding to the Casorati matrices. Paired NV, NB, and VL values obtained after processing the same IQ data using the optimal shrinkage and truncated SVD clutter filters were compared to evaluate the effect of optimal shrinkage clutter filtering on microvessel detection sensitivity.

2.3.5 Image Quality Metric

The SNR and CNR of paired microvascular images were also compared. The SNR, expressed in decibels, was computed as the ratio of the mean signal power in an intravascular ROI to the mean signal power in a background noise ROI. The CNR in dB was computed as:

$$CNR = \frac{\overline{PW_{vessel}} - \overline{PW_{tissue}}}{std(PW_{tissue})} \quad (2.11)$$

Where $\overline{PW_{vessel}}$ is the mean of Doppler signal in the vessel while $\overline{PW_{tissue}}$ is the mean of Doppler signal in the surrounding tissue. For both SNR and CNR, a rectangular ROI was manually defined surrounding visually prominent vessel structures. An intravascular ROI was then segmented in a manner similar to [3] by manually outlining connected segments of color pixels within the larger rectangular ROI. Pixels within the rectangular ROI but outside the intravascular contour were treated as clutter pixels. Background noise ROIs

were defined as separate rectangular regions that lacked visually apparent vessel structures. To avoid observer bias in selection of the noise ROI, three such regions were selected for each image and the mean of the SNR computed using each noise ROI was used as an image quality metric for that image. The relative performance of the optimal shrinkage and truncated SVD clutter filters was assessed by comparing the means of the single-image SNR and CNR estimates for the tumor and hindlimb images.

2.4 Results

2.4.1 Visual Comparison of SVD Clutter Filtered Images

Figure 2.1 displays images of two representative tumors with distinct vascularization patterns. The figure includes conventional power Doppler images produced by the Vevo 2100's onboard software (panel A), microvascular images constructed using truncated SVD clutter filtering (panels B), microvascular images produced using optimal shrinkage SVD clutter filtering (panels C), and vessel network skeletons extracted from the optimal shrinkage images (panels D). The first tumor image (Fig. 2.1 A-1 to D-1) shows a branching network of intra-tumoral vessels radiating outward from a central, axially oriented feeding vessel; 12 tumors exhibited this architecture. The bottom row shows a dense mesh like network connected to laterally oriented feeding vessels within the CAM; the remaining 10 tumors had this phenotype. The power Doppler images show the B-mode background used to segment the tumor cross sections (cyan arrows) and provide confirmation of the larger vessels that are independent of our offline SVD processing.

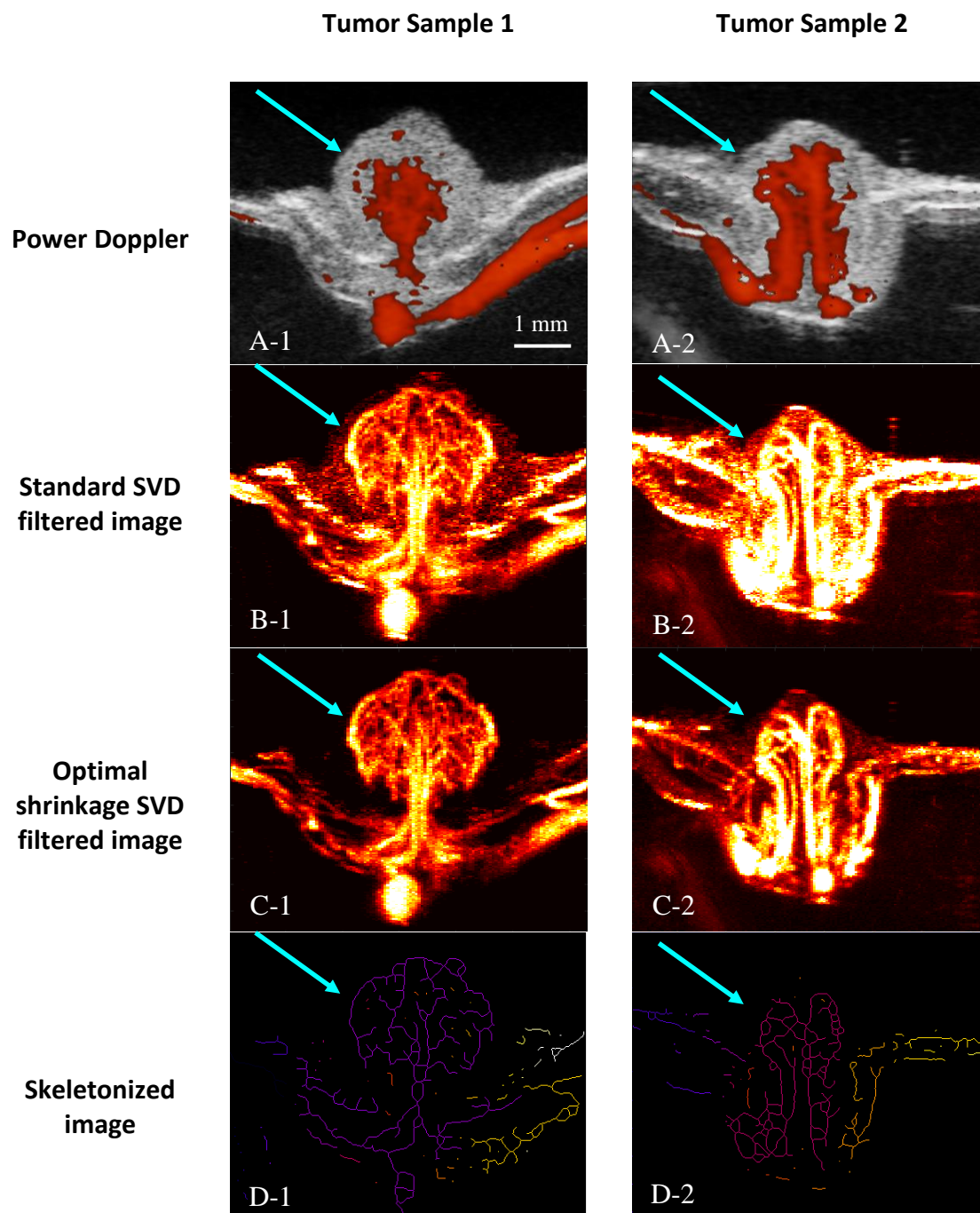


Figure 2.1: Images of tumors engrafted on the CAM of chick embryo. A) Conventional power Doppler (infinite impulse response-filtered) image produced by the ultrasound system. **B)** Image of the same tumor after standard SVD clutter filtering. **C)** Image of the same tumor after optimal shrinkage SVD clutter filtering. **D)** Skeleton of the vascular network extracted from the optimal shrinkage SVD clutter filtered image. The cyan arrows show the tumor.

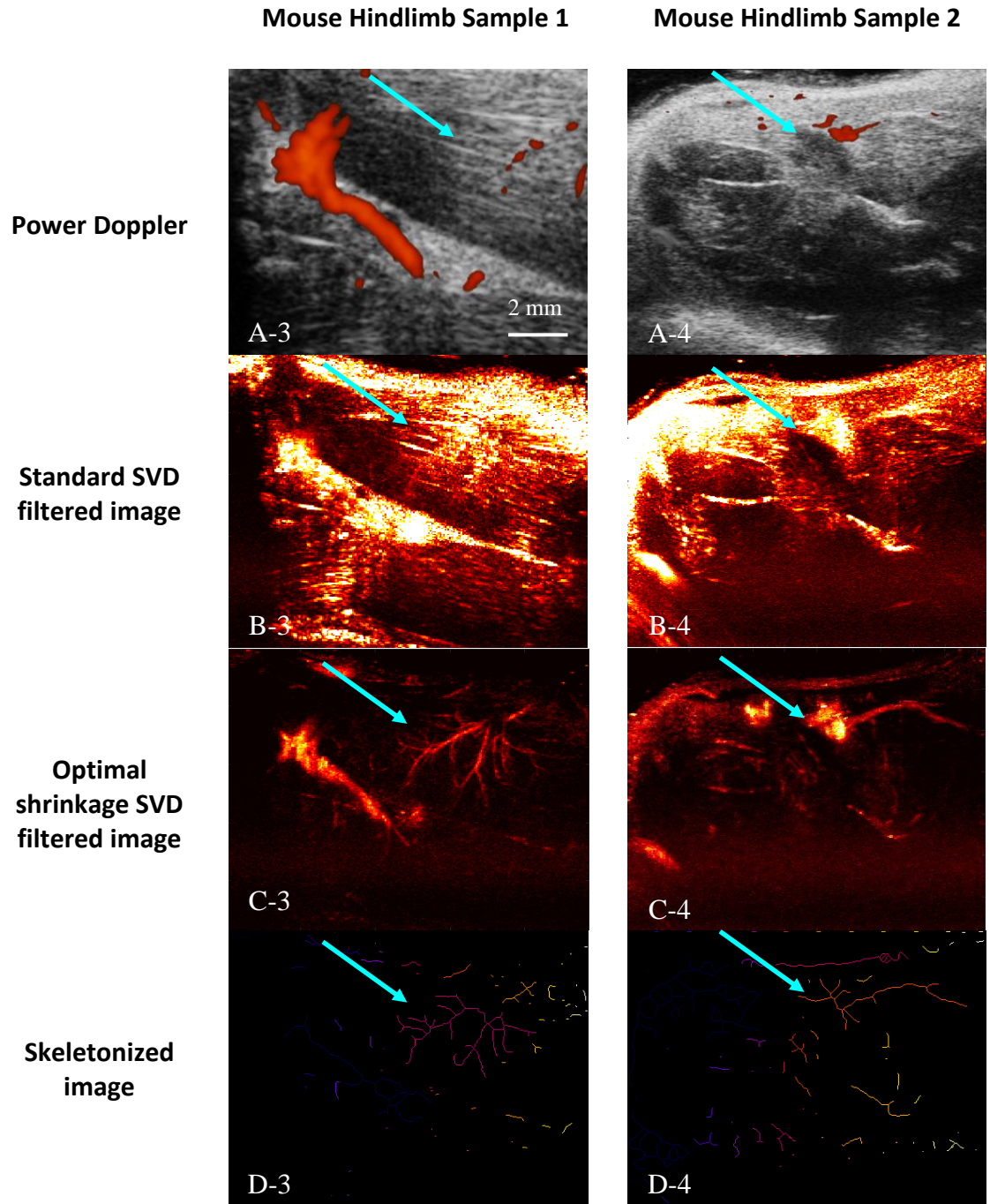


Figure 2.2: Images of mice hindlimb. A) Conventional (infinite impulse response-filtered) image produced by the ultrasound system. B) Image of the same hindlimb after standard SVD clutter filtering C) Image of the same hindlimb after optimal shrinkage SVD clutter filtering. D) Skeleton of the vascular network extracted from the optimal shrinkage SVD clutter filtered image. The cyan arrows show the tumor.

Vascular network skeletons computed from the truncated SVD images are omitted from the figure because they differed only subtly from the vascular skeletons extracted from the optimal shrinkage images. The SVD-filtered tumor microvascular images depict similar large and intermediate-scale vascular structures with clearly enhanced vessel sensitivity relative to the power Doppler images. However, in comparison to the truncated SVD images (Figs. 2.1, panel B), the optimal shrinkage images (Fig. 2.1 panel C) show sharper vessel boundaries with less background clutter in the gaps between adjacent vessels. These characteristics of the optimal shrinkage images enable, upon close inspection, detection of additional small vessels, clearer identification of additional generations of vessel branching, and more complete visualization of the vascular network at the tumor periphery.

Figure 2.2 presents hindlimb images of two different mice laid out in the same format as Fig. 2.1. The advantage of the optimal shrinkage clutter filter, compared to the truncated SVD clutter filter, is much more striking in the hindlimb images than in the tumors and results in larger differences in background clutter level, improved detection of small vessels, and enhanced connectivity of vessel segments. The unfiltered hindlimb data can be expected to include more prominent clutter signal than the tumor data due to the intervening tissue layers in the hindlimb images as well as substantial backscattering intensity from the muscles surrounding the vessels of interest. The difference in relative performance of the two SVD filtering methods is therefore attributed to more effective attenuation of clutter components by the optimal shrinkage filter. Additional evidence for this interpretation is provided in the following subsections.

Representative singular value curves are presented in Fig. 2.3 for the tumor sample 1, and in Fig. 2.4 for the mouse hindlimb sample1. In each panel, the upper boundary of the filled regions corresponds to the singular values of the original Casorati matrix, y_i . The blue area represents the signal power eliminated by the optimal-shrinkage clutter filter and corresponds mathematically to the rescaled shrinkage function, $\frac{\hat{\sigma}_B}{\sigma_{nat}} \eta_{opt} \left(\frac{\sigma_{nat}}{\hat{\sigma}_B} y_i \right)$ in (8). The orange area represents the singular values retained by the optimal-shrinkage filter, *i.e.*, the expression within the outer pair of parentheses in (8), which are assumed to consist primarily of blood signals.

The rightmost vertical dashed lines in both panels indicate the rank at which the original singular value curves intersect the effective singular value threshold, $(\hat{\sigma}_B/\sigma_{nat})(1 + \sqrt{\beta})$, applied by the optimal shrinkage clutter filter. The leftmost vertical dashed line denotes the rank threshold, r , from (10) that is employed by the truncated SVD clutter filter. The truncated SVD filter completely eliminates the signal power from rank 1 to r and retains all of the signal power at ranks greater than (to the right of) r . As the figure suggests, the total power removed by the optimal-shrinkage clutter filter (the blue area) is always greater than the total power removed by the truncated SVD filter, which is reflected in the images by visibly reduced background clutter between vessels.

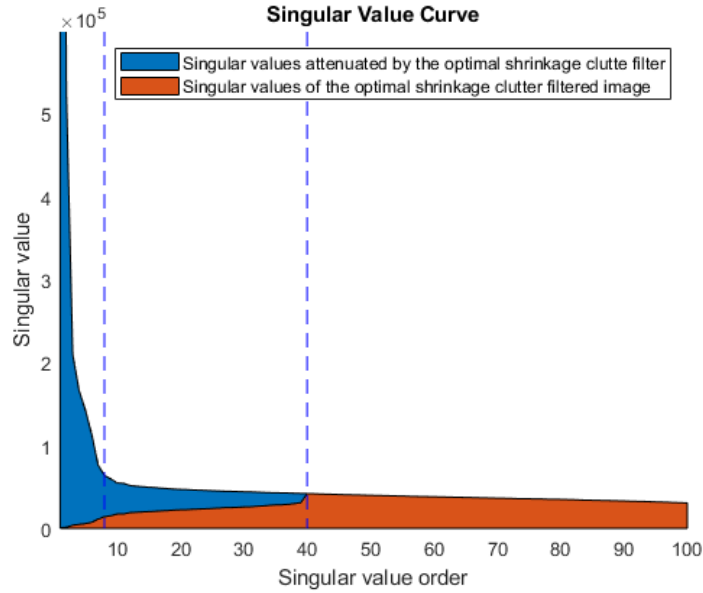


Figure 2.3: Singular value curves for truncated SVD and an optimal shrinkage SVD-filtered tumor image shown in Fig. 2.1 (tumor sample 1). The orange area represents the singular values of the filtered image, and the blue area represents the singular values attenuated by the filter. The blue dashed vertical lines denote the rank thresholds for standard truncated SVD clutter filtering (left) and optimal shrinkage SVD-based clutter filtering (right).

In the tumor example, Fig. 2.3, the singular value curve reached the singular value threshold for the optimal shrinkage clutter filter at rank 40, while the rank threshold for the truncated SVD filter was $r = 8$. 96.8% of the total power was removed from the original data using optimal shrinkage whereas 93.9% of the total power was attenuated using the truncated SVD clutter filter. Across all tumors, the singular value threshold for optimal shrinkage was reached at ranks between 37-45, which was always much greater than the rank threshold employed by the truncated SVD filter, which ranged from 5 to 11.

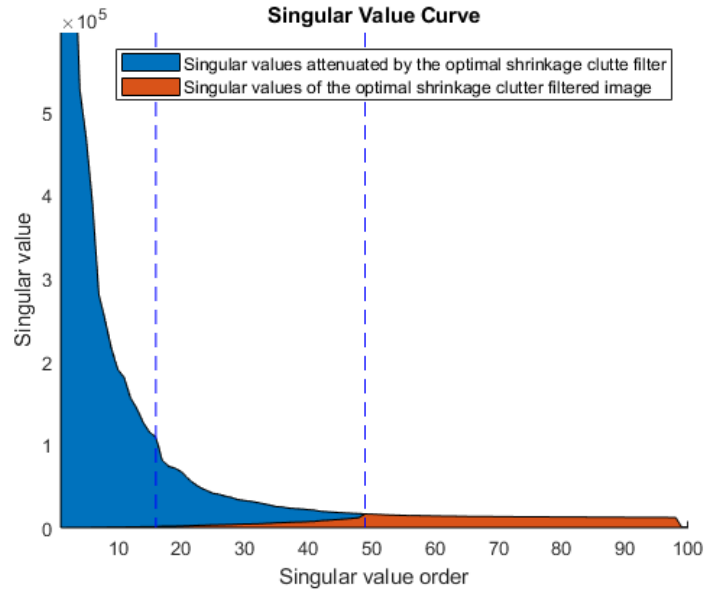


Figure 2.4: Singular value curves for truncated SVD and an optimal shrinkage SVD-filtered hindlimb image shown in Fig. 2.2 (mouse hindlimb sample 1). The orange area represents the singular values of the filtered image, and the blue area represents the singular values attenuated by the filter. The blue dashed vertical lines denote the rank thresholds for standard truncated SVD clutter filtering (left) and optimal shrinkage SVD-based clutter filtering (right).

Similar observations can be made for the hindlimb singular value curves. In the example in Fig. 2.4, the singular value curve reached the singular value threshold for the optimal shrinkage clutter filter at rank 50, while the rank threshold for the truncated SVD filter was $r = 17$. 99.8% of the total power was removed from the original data using optimal shrinkage whereas 95.4% of the total power was attenuated using the truncated SVD clutter filter. Among all mice, the singular value threshold for optimal shrinkage was reached at

ranks between 42 and 53, which was always much greater than the rank threshold employed by the truncated SVD filter, which ranged from 10 to 18. The results indicate that the percentage of the total power removed by optimal shrinkage clutter filtering method is higher in hindlimb application than CAM tumor model application by 1.5%.

2.4.2 Vascular Network Morphological Parameters

Table 2.1 reports the vascular network morphology parameters (number of vessels, number of branching points, and mean vessel length) estimated from the vascular skeletons extracted from the truncated SVD and optimal shrinkage images. Data are reported as mean \pm standard deviation for the 22 tumor and 8 hindlimb images. For both imaging applications, optimal shrinkage substantially increased the number of vessels and the number of branching points detected compared to truncated SVD clutter filtering, which is consistent with the visual observations of improved sensitivity to small vessels stated in Sect. IV.A.

Table 0.1: NV = number of vessels, NB = number of branching points, VL = mean vessel length. Data are reported as mean \pm standard deviation over 22 tumors and 8 mice hindlimb images.

Application	Clutter Filter	NV	NB	VL
Tumor	Standard SVD	42.1 \pm 7.9	21.1 \pm 6.8	137 \pm 90
	Optimal Shrinkage	63.8 \pm 13.7	33.6 \pm 8.7	188 \pm 102
Hindlimb	Standard SVD	18.6.8 \pm 4.5	9.7 \pm 3.1	68 \pm 27
	Optimal Shrinkage	37.5 \pm 9.6	16.8 \pm 3.4	118 \pm 24

Optimal shrinkage also increased the mean vessel length, which indicates that those images depict better-connected vessel segments. The number of vessels depicted using optimal shrinkage was approximately 50% greater than truncated SVD in the tumor images and was doubled in the hindlimb images. Similarly, the mean vessel length using optimal shrinkage was approximately 40% greater in the tumor images and almost 75% greater in the hindlimb images. The larger relative differences in the hindlimb images in the hindlimb

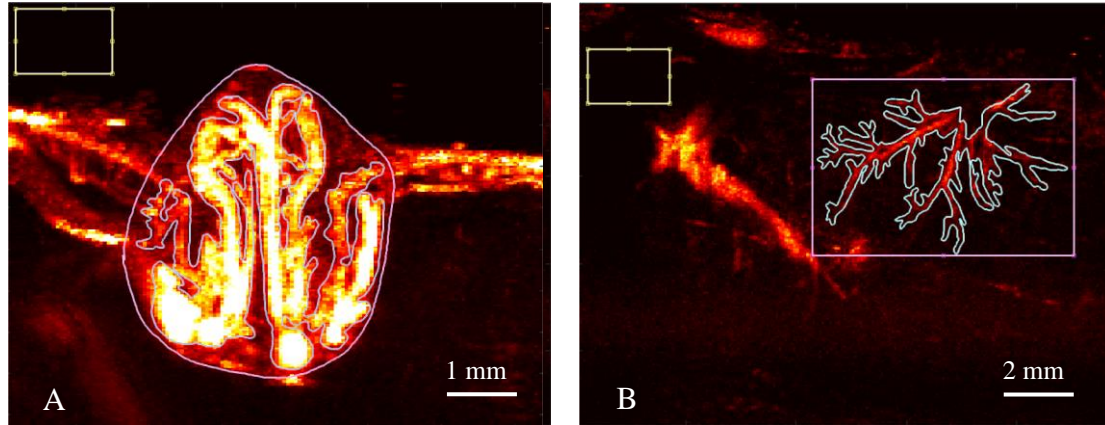


Figure 2.5: A) A reconstructed optimal-shrinkage-filtered image of tumor sample 1, engrafted in CAM model and B) reconstructed optimal-shrinkage-filtered image of a mouse hindlimb sample 1. For CNR and SNR evaluation, the pink box defines the ROI in which the cyan lines indicate the manual segmentation of vessels and the rest of the signal in the white box indicates clutter. The yellow boxed region defines the background noise.

images is again attributed to the presence of more prominent clutter that was more effectively removed by the optimal shrinkage filter.

2.4.3 Image Quality Metric

Figure 2.5 shows examples of the manually segmented intravascular and background ROIs used to compute SNR and CNR for a tumor image (panel A) and a hindlimb perfusion image (panel B). Table 2.2 lists the mean \pm standard deviation of the SNR and CNR for each combination of SVD clutter filter and imaging application. In the tumor images, optimal shrinkage increased the mean SNR by 2.9 dB and the mean CNR by 2.5 dB compared to truncated SVD clutter filtering. In the hindlimb perfusion images, optimal shrinkage increased the mean SNR by 3.7 dB and the mean CNR by 4.9 dB. The more pronounced improvement using optimal shrinkage in the hindlimb images is consistent with the differences in vascular morphology parameters and is again attributed to the benefits of the optimal shrinkage method being more evident in the more challenging clutter conditions presented by the hindlimb model.

Table 2.2: SNR and CNR in tumor and hindlimb applications for each the of SVD clutter filtering method. For tumor application the values are averaged over 22 tumor images and for hindlimb application, the reported values are averaged over 11 mice hindlimb images.

Application	Clutter Filter	SNR	CNR
CAM Tumor	Standard SVD	56.2 \pm 3.5	35.8 \pm 2.7
	Optimal Shrinkage	59.1 \pm 2.9	38.3 \pm 3.8
Mice Hindlimb	Standard SVD	35.9 \pm 4.7	11.9 \pm 2.4
	Optimal Shrinkage	39.6 \pm 6.9	16.8 \pm 3.6

2.5 Discussion

The results indicate that the optimal shrinkage clutter filtering approach outperforms the standard SVD clutter filtering method in effectively suppressing the attenuated clutter signals in both tumor and hindlimb applications. The optimal shrinkage clutter filtered images, represented by panel "C" in both Fig. 2.1 and 2.2, exhibit greater sensitivity to microvessels and contain more vessel structures than the truncated SVD filtered images depicted by panel "B" in both applications.

The optimal shrinkage clutter filtering technique produces clearer vessel network structures, branching points, and increased vasculature, which is supported by the data presented in Table 2.1. Quantitative analysis of morphological parameters reveals that the optimal shrinkage clutter filtered images exhibit a greater number of vessels, branching points, and mean vessel length than the standard SVD filtered images. Moreover, Fig. 2.3 and 2.4 demonstrates how the proposed method shrinks down the singular values of the singular components with rank between the two dashed lines (thresholds are defined by two filtering method of truncated SVD and optimal shrinkage SVD).

Upon comparing the degree of improvement in vascular visualization between the two applications (as illustrated in Fig. 2.1 and 2.2), it becomes evident that the optimal shrinkage clutter filtering approach exhibits superior performance for hindlimb images as compared to tumor images. Specifically, a comparison between panel "B" and "C", of Fig.

2.1 and 2.2, in both applications demonstrates that the optimal shrinkage clutter filtered image in hindlimb application detects a greater amount of vasculature as compared to its standard SVD filtered counterpart.

This observation is further supported by the higher degree of enhancement observed in the reported values for morphological analysis. Upon comparing the NV, NB, and mean VL for the standard SVD filtered images and optimal shrinkage filtered images in both applications, a greater increase in the reported values is observed for hindlimb images as compared to tumor images. These results indicate that the optimal shrinkage clutter filtering approach is more effective in suppressing clutter and enhancing vasculature in hindlimb images than tumor images. Furthermore, this phenomenon is clearly discernible when analyzing the singular value curves of the two applications, as illustrated in Fig. 2.3. Specifically, the singular value curve of the hind limb image exhibits a greater degree of clutter shrinkage in comparison to the singular value curve of the tumor image.

Upon considering the region between the two dashed lines, which indicates the thresholds for standard SVD and optimal shrinkage filters, it becomes apparent that the ratio of the singular values of the optimal shrinkage filtered images (*i.e.*, the singular values depicted by orange) to the attenuated singular values by optimal shrinkage (*i.e.*, the singular values depicted by blue) is less for hind limb images (shown in Fig. 2.3) as compared to tumor images. This discrepancy can be attributed to the fact that the hindlimb muscle images are obtained from deeper regions, resulting in greater attenuation of clutter signals as compared to the chick CAM tumor images, where the tumor is situated on the top of the chick embryo surface.

Moreover, if the rank threshold of the truncated SVD clutter filtering method is increased toward the threshold used in the corresponding optimal shrinkage clutter filters, the appearance of the truncated SVD images shows less distortion by clutter, however with less fine vessel structure and microvascular network in the reconstructed image. This indicates that in truncated SVD clutter filtering, even though the increase in the blood-clutter threshold to higher ranks helps with more elimination of tissue clutter attenuation in the reconstructed image however with the cost of losing more microvasculature. Thus,

increase in the rank of the threshold does not help in detection of more microvasculature and still optimal shrinkage clutter filtering outperforms the truncated filtering with threshold rank increase.

The large separation of the two thresholds (i.e., blood-clutter threshold defined by truncated SVD and optimal shrinkage clutter filtering method) in the results implies that the clutter and blood singular vectors overlap to a much greater extent than is assumed among most of the researchers when they state that the clutter signal is low rank. It further shows why truncated SVD clutter filtering are not capable of fully eliminating tissue clutter attenuation which is due to the assumption that tissues and blood only overlap in the singular components below the low-order defined threshold, while the results clearly shows the overlap between blood and clutter extended to more than twice the threshold defined by truncated SVD clutter filtering methods.

It is notable that the optimal shrinkage method also retains a small amount of blood signal power from singular vectors with rank less than λ , i.e., the much smaller orange area to the left of the lower rank threshold in Fig. 2.3 and 2.4, but this additional blood signal makes only a minor contribution to the image. The greater power removed from the original data by the optimal shrinkage filter improved the Doppler contrast of small vessels in the filtered images. Moreover, the rank threshold of optimal shrinkage clutter filtering for hindlimb images is generally greater than that of tumor images, i.e., the rank threshold is in the range of 42-53 and 37-45 for hindlimb and tumor images respectively. This further confirms that there is more overlap between tissue and blood signal in higher singular value ranks in hindlimb images and that optimal shrinkage method can further detect, shrink, and eliminate the effect of tissue clutter signal in higher ranks.

In addition, Table 2.2 shows a significant increase in the level of enhancement for SNR and CNR in hindlimb images than tumor images. Relatively, there are even more enhancements in CNR than SNR. The reason is that in the hindlimb application, contains high and that is why even with truncated SVD filtering method, the average CNR value is smaller in hindlimb images than in the tumor images. Similarly, the SNR is relatively smaller in hindlimb images due to the existence of a very low blood signal attenuation in

hindlimb images. The proposed filtering method also showed substantial improvement in suppression of the depth-dependent far field tissue clutter. However, it is obvious that the optimal shrinkage significantly improves the SNR and CNR in both applications with further aligns with the other results presented in this paper.

There is a clear consistent outcome with all the results shown which all indicates no matter how different the two presented applications are, optimal shrinkage clutter filtering always outperforms standard SVD clutter filtering in suppressing more clutter attenuation and detection of more signal and therefore more blood signal in the filtered images. Particularly, when the level of tissue clutter attenuation increases, the enhancements in microvessel detection with optimal shrinkage clutter filtering increases both qualitatively and quantitatively.

Noise reduction is not necessary (any technique can be used). The tissue attenuation of the chicken embryo tumor model is minimal, and the line-by-line focused imaging used in this study had a sufficiently high SNR to make the noise suppression unnecessary in this application. Our analysis is designed to show the difference of reconstructed image of two mentioned filtering methods and the ability of proposed method in reducing the effect of more clutter singular components and thus it is independent of noise reduction techniques. In this study we used the standard noise reduction technique with SVD approach which zero out the high order singular values to eliminate the effect of low-power noisy singular components.

2.6 Conclusion and Future Works

This paper presents an SVD-based optimal shrinkage clutter filtering technique that can substantially improve clutter rejection and small vessel imaging quality for power doppler ultrasound. The proposed technique successfully overcame the challenges of small vessel clutter filtering for in vivo human imaging by facilitating robust singular value thresholding on a local level and combining the results for improved imaging quality. This method can facilitate the translation of high frame rate ultrasound small vessel imaging from laboratory to clinic, and has great potential for early detection, diagnosing, and follow up of many diseases.

Currently the signal characteristics that are used and assumed for optimal shrinkage function are not tuned for ultrasound microvascular imaging. Therefore, one possible future work is to tune the optimal shrinkage function for microvascular ultrasound. Moreover, the performance of this optimal shrinkage clutter filtering can be tested on plane-wave ultrasound imaging to evaluate its performance compared to truncated SVD.

References

- [1] A. C. H. Yu and L. Lovstakken, "Eigen-based clutter filter design for ultrasound color flow imaging: a review", *IEEE Transactions on Ultrasonics, Ferroelectrics, and Frequency Control*, vol. 57, no. 5, pp. 1096-1111, May 2010
- [2] J. Baranger, *et al.*, "Adaptive Spatiotemporal SVD Clutter Filtering for Ultrafast Doppler Imaging Using Similarity of Spatial Singular Vectors", *IEEE Transactions on Medical Imaging*, vol. 37, no. 7, pp. 1574-1586, July 2018
- [3] P. Song, *et al.*, "Ultrasound Small Vessel Imaging With Block-Wise Adaptive Local Clutter Filtering", *IEEE Transactions on Medical Imaging*, vol. 36, no. 1, pp. 251-262, Jan. 2017
- [4] M. Kim, *et al.*, "Efficiency of U.S. Tissue Perfusion Estimators," in *IEEE Transactions on Ultrasonics, Ferroelectrics, and Frequency Control*, vol. 63, no. 8, pp. 1131-1139, Aug. 2016
- [5] S.A. Waraich, *et al.*, "Auto SVD clutter filtering for US Doppler imaging using 3D clustering algorithm", *Lecture Notes Computer Science*, vol. 11663, pp. 473-483, 2019.
- [6] M. Gavish and D.L. Donoho, "The optimal hard threshold for singular values is $4/\sqrt{3}$ ", *IEEE Transaction on Information Theory*, vol. 60, pp. 5040-5053, 2014
- [7] M. Gavish and D.L. Donoho, "Optimal shrinkage of singular values", *IEEE Transaction on Information Theory*, vol. 63, pp. 2137-2152, 2017
- [8] K.M. Huynh, *et al.*, "Noise mapping and removal in complex-valued multi-channel MRI via optimal shrinkage of singular values", *Lecture Notes Computer Science*, vol. 12906, 2021
- [9] W. Zhu, *et al.*, "Denoise functional magnetic resonance imaging with random matrix theory based principal component analysis", *IEEE Transaction in Biomedical Engineering*, vol. 69, pp. 3377-3388, 2022
- [10] L. Codero-Grande, *et al.*, "Complex diffusion-weighted image estimation via matrix recovery under general noise models", *NeuroImage*, vol. 200, pp. 391-404, 2019
- [11] H. Chen, *et al.*, "Speckle attenuation by adaptive singular value shrinking with generalized likelihood matching in optical coherence tomography", *Journal of Biomedical Optics*, vol 23, no. 3, 2018
- [12] H. Chen, *et al.*, "Speckle reduction based on fractional-order filtering and boosted singular value shrinkage for optical coherence tomography image", *Biomedical Signal Processing and Control*, vol. 52, pp. 281-292, 2019

- [13] M. Bataghva, *et al.*, "Contrast-Free Ultrasound Microvascular Imaging With Optimal Clutter Shrinkage to Enhance Tumor Vascular Quantification", *IEEE International Ultrasonics Symposium (IUS)*, Las Vegas, NV, USA, 2020, pp. 1-4, 2020
- [14] J. Veraart, *et al.*, "Diffusion MRI noise mapping using random matrix theory", *Magnetic Resonance in Medicine*, vol. 76, pp. 1582-1593, 2016
- [15] S. Maruvada, *et al.*, "High-frequency backscatter and attenuation measurements of porcine erythrocyte suspensions between 30-90 MHz", *Ultrasound in Medicine Biology*, vol. 28, pp. 1081-1088, 2002
- [16] C. Huang, *et al.*, "Noninvasive Contrast-Free 3D Evaluation of Tumor Angiogenesis with Ultrasensitive Ultrasound Microvessel Imaging", *Science Reports*, vol. 9, no. 4907, 2019
- [17] A.C. Tufan and N.L. Satiroglu-Tufan, "The chick embryo chorioallantoic membrane as a model system for the study of tumor angiogenesis, invasion and development of anti-angiogenic agents", *Current Cancer Drug Targets*, vol. 5, no. 4, pp. 249-266, 2005
- [18] M. Bataghva, *et al.*, "Multiparametric Microvascular Ultrasound to Classify Tumor Sensitivity to Anti-Angiogenic Treatment: Application to Multiple Cell Lines," *IEEE International Ultrasonics Symposium (IUS)*, Venice, Italy, pp. 1-4, 2022
- [19] M. Gavish and D. Donoho. (2015). Code Supplement to ‘Optimal Shrinkage of Singular Values’. [Online]. Available: <http://purl.stanford.edu/kv623gt2817>
- [20] S. Ghavami, *et al.*, "Quantification of morphological features in non-contrast-enhanced ultrasound microvasculature imaging", *IEEE Access*, vol. 8, pp. 18925-18937, 2020

Chapter 3

3 Ultrasound-Based Microvascular Parameters for Classification of Anti-Angiogenic Tumor Treatment Response

The contents of this chapter have been adapted from

*"Ultrasound-Based Microvascular Parameters for Classification of Anti-Angiogenic Tumor Treatment Response: A Scalable Preclinical Approach", published in IEEE International Ultrasonics Symposium (IUS), Las Vegas, NV, USA, pp. 1-4, 2020 by M. Bataghva, D. Johnston, N. Power, S. Penuela and J. C. Lacefield**

&

*"Comparison of Contrast-Enhanced Ultrasound Parameters for Classification of Anti-Angiogenic Tumor Treatment Response" published in IEEE International Ultrasonics Symposium (IUS), Xi'an, China, pp. 1-4, 2021 by M. Bataghva, D. Johnston, N. Power, A. Ward, S. Penuela and J. C. Lacefield***

*© 2020 IEEE. Reprinted, with permission, from M. Bataghva, D. Johnston, N. Power, S. Penuela and J. C. Lacefield, "Ultrasound-Based Microvascular Parameters for Classification of Anti-Angiogenic Tumor Treatment Response: A Scalable Preclinical Approach", IEEE International Ultrasonics Symposium (IUS), Las Vegas, NV, USA, pp. 1-4

**© 2021 IEEE. Reprinted, with permission, from M. Bataghva, D. Johnston, N. Power, A. Ward, S. Penuela and J. C. Lacefield, "Comparison of Contrast-Enhanced Ultrasound Parameters for Classification of Anti-Angiogenic Tumor Treatment Response", IEEE International Ultrasonics Symposium (IUS), Las Vegas, NV, USA, pp. 1-4

3.1 Introduction

Ove the past 25 years, many cancer imaging studies have investigated the efficacy of PD and CEUS for assessing tumor vascularity and responses to antiangiogenic drugs. The utility of ultrasound imaging for evaluating anti-angiogenic treatment responses in cancer models is widely recognized. The recent emergence of techniques such as SVD clutter filtering, *e.g.*, [1], and ultrasound localization microscopy [2] have dramatically improved the microvessel sensitivity of ultrasound. The rapid expansion in the armamentarium of microvascular imaging techniques amplifies the need for more efficient approaches to identify combinations of perfusion parameters that correlate with anti-angiogenic treatment responses in specific cancers. However, the best approach to combine ultrasound-based microvascular features remains unclear.

This chapter first presents initial steps towards a scalable preclinical platform for classifying anti-angiogenic treatment response using ultrasound-based multiparametric microvascular imaging. Initially, seven perfusion parameters from two- and three-dimensional PD and two-dimensional contrast-enhanced ultrasound (CEUS) as well as tumor volume are fed into a multivariable logistic regression learning model to classify control (modeling resistant) and treated (modeling sensitive) tumors engrafted on a chicken embryo assay. Classification results indicate that, optimal shrinkage SVD-based filtered PD images are valuable for detecting anti-angiogenic treatment responses and the microvascular and perfusion parameters derived from these filtered PD images improves the classification performance when used along those of conventional analysis of PD and CEUS.

Further in this chapter, the utility of statistical CEUS method, which describes the change in the histogram of image intensity during microbubble wash-in, that was developed previously in our lab in antiangiogenic treatment response classification is studied. We investigated whether the statistical analysis of CEUS as a means of characterizing the spatial heterogeneity of tumor perfusion should be preferred to conventional mean-intensity-based CEUS analysis for classification of anti-angiogenic treatment responses in

a preclinical tumor model. The results showed that the learning model combining features from both conventional and statistical CEUS analysis more accurately classified anti-angiogenic response than models using either statistical or conventional features alone. Therefore, the statistical CEUS method is best used as a supplement to conventional CEUS analysis.

3.1.1 PD Microvascular Quantification

PD and CEUS are real-time, inexpensive, and safe tools for microvascular imaging. PD ultrasound is sensitive to the squared magnitude of the blood flow signal which is correlated with blood volume, making it particularly useful for detecting low-velocity blood flow in small vessels. Doppler ultrasound has become an increasingly popular tool for microvascular imaging, particularly in cancer research [3], it can be used to assess tumor angiogenesis and microvascular perfusion [4], or the formation of new blood vessels to support tumor growth [5]. However, power Doppler ultrasound suffers from the presence of clutter signals caused by tissue motion and other factors unrelated to blood flow. These clutter signals can obscure the low-amplitude signals from slow-flowing blood in small vessels, reducing the sensitivity and specificity of power Doppler imaging for microvascular perfusion.

SVD clutter filtering improves the contrast and resolution of power Doppler images, allowing for better visualization and quantification of microvascular perfusion. If one assumes the eigen spectra of blood and clutter overlap, truncated SVD attenuates the lowest-order, highest singular value components and is incapable of removing all clutter signals specifically the high-order singular components representing them. On the other hand, truncated SVD may remove all low-order singular components representing microvessels. Optimal shrinkage clutter filtering introduced in the previous chapter demonstrates significant improvements in elimination of low-order clutter singular values and therefore allows for better visualization and quantification of microvascular perfusion.

Microvascular parameters are crucial for understanding the tumor microenvironment and assessing treatment effectiveness. Among the microvascular parameters commonly used in these applications are the VI, NV, NB, and mean VL. VI represents the percentage of

the tumor area occupied by blood vessels while the number of vessels and branching points are measures of the density and complexity of the tumor vasculature, respectively. Changes in these microvascular parameters can indicate the effectiveness of the treatment in inhibiting angiogenesis [6] and monitoring these parameters can also help predict patient prognosis and guide treatment selection.

3.1.2 CEUS Perfusion Analysis

CEUS imaging, on the other hand, enables rapid, longitudinal quantification of microvascular perfusion with the administration of microbubbles. Contrast-enhanced ultrasound can be used to quantify changes in perfusion to stratify and monitor anti-angiogenic treatment responses [7]. However, conventional dynamic CEUS analysis relies on the mean backscattered signal intensity from a region of interest, which discounts additional information that might be available from heterogeneous contrast enhancement in the tumor cross section. To address this limitation, a method for analyzing the change in first-order speckle statistics during microbubble wash-in from a time series of nonlinear CEUS images was introduced in our lab.

In statistical CEUS method [8], the PDF of the contrast-enhanced signal intensity, $f(I)$, is modeled as a mixture of exponential PDFs weighted by the function $w(\theta)$,

$$f(I) = \int w(\theta)p(I|\theta)d\theta \quad (3.1)$$

Where $p(I|\theta)$ is an exponential distribution conditional on the scale parameter, θ :

$$p(I|\theta) = \theta e^{-\theta t} \quad (3.2)$$

Different values of θ can be viewed as arising from different local microbubble concentrations, such that $w(\theta)$ characterizes the spatial heterogeneity of contrast enhancement in the region of interest. A statistical CEUS wash-in curve is constructed by analyzing the change in $w(\theta)$ during either a bolus infusion or destruction-replenishment.

In [8], the statistical CEUS method was applied to a murine breast cancer xenograft model using a bolus-injection CEUS protocol. Parameters estimated from statistical CEUS wash-in curves discriminated bevacizumab-treated tumors from untreated tumors more accurately than the corresponding parameters from conventional CEUS analysis. Those

results suggested that the statistical method could improve the reliability of CEUS for quantifying anti-angiogenic treatment response in tumors. However, only pairwise comparisons of single parameters from statistical and conventional CEUS were performed in that experiment.

3.1.3 Machine Learning Models for Antiangiogenic Treatment Response

In recent years, the use of machine learning for medical image analysis and cancer research has significantly expanded. One particularly promising application of machine learning in cancer imaging is the classification of tumor treatment sensitivity [9]. Evaluation of responses to anti-angiogenic drugs requires a machine learning algorithm that can be trained to discriminate treatment-sensitive from treatment resistant tumors based on features that provide morphological and/or functional information about a tumor's vascular network. Recent advances in imaging technology, such as power Doppler ultrasound and contrast-enhanced ultrasound, have provided high-resolution images that can be used to extract useful information about the microvascular features of tumors. Training, testing, and validation of a classification algorithm often require many images, so the scalability of the experimental model used to develop a classifier becomes an important consideration.

3.2 Methods and Materials

3.2.1 Study Design

In this study, we advocate for the use of cancer cell lines xenografted onto the *ex-ovo* chicken embryo CAM as an experimental model that addresses the efficiency and scalability requirements outlined in the preceding paragraphs. Chick CAM models are an effective tumor angiogenesis assay [10] that yield high-quality, high throughput images with high-frequency ultrasound [11]. The efficiency of the platform is a consequence of the low cost of fertilized eggs (< \$1 each) relative to the immunocompromised rodents often used for human cancer xenografts as well as the rapid growth rates of tumor specimens in the chick CAM, where treatment endpoints occur at approximately two weeks. Scalability is provided by the use of established cell lines, which should produce genomically identical initial tumors, thereby permitting data to be pooled over multiple serial experiments so large sample sizes may be accumulated within a few weeks. Cell line

models are sufficient for our purposes because our emphasis is on the development of new ultrasound imaging techniques and image analysis methods.

As proof of concept, we report here on a treatment response experiment using the Caki-1 human mRCC cell line. Caki-1 cells exhibit high sensitivity to the anti-angiogenic agent Sunitinib [12], which is an approved first-line systemic therapy for mRCC [13] and therefore is the drug used in this study. It is worth mentioning that in clinical practice, Sunitinib anti-angiogenic treatment is predominantly used for metastatic tumors as they have a less established blood supply and are more responsive to anti-angiogenic therapies like Sunitinib and that why both the tumor type and therapy was used in this thesis. The study design yields a group of tumors with an unequivocally strong treatment response for comparison to control specimens that represent tumors with no treatment response. In this pilot study, feature selection for the classifiers begins with a maximum of eight inputs: endpoint tumor volume, one vascular feature from three-dimensional (3D) PD using conventional infinite impulse response (IIR) clutter filtering, three vascular features from two-dimensional (2D) PD using an SVD clutter filter, and three perfusion features from 2D CEUS. Classifier performance is evaluated by determining the accuracy, sensitivity, and specificity for discriminating treated tumors from control tumors.

Moreover, to assess the value of statistical CEUS for detecting anti-angiogenic treatment responses, multiparametric classifiers constructed using classical machine learning methods (*i.e.*, logistic regression and support vector machine) are compared, thereby accounting for correlations among different features. The performance of classifiers using only statistical CEUS features is compared to classifiers using only conventional CEUS features and classifiers using a combination of statistical and conventional features. Feature selection algorithms are also applied to the complete set of parameters to identify the most informative features. The results enable an assessment of whether the statistical CEUS method should be preferred to conventional analysis for this treatment-monitoring application.

The platform employs high frequency ultrasound imaging of a human metastatic renal cell carcinoma cell line engrafted onto the CAM of *ex-ovo* chicken embryos. Images are

acquired from untreated tumors and tumors treated with an anti-angiogenic tyrosine kinase inhibitor, Sunitinib. This study design yields a group of tumors with a strong treatment response for comparison to control specimens with no treatment response. Use of the CAM assay in place of the murine model in [14] provides a more economical tumor model that reaches its experimental endpoint more quickly. The CAM assay requires a destruction-replenishment CEUS protocol, rather than the bolus injection protocol used in [14], because it is not feasible to image a CAM tumor model simultaneously with a contrast injection into the CAM's delicate vessel network.

3.2.2 Ex-Ovo Tumor Model Experiment

Caki-1 kidney tumor cells (American Type Culture Collection, Manassas, VA) were engrafted onto ex ovo chick CAMs following the protocol described in [15]. Briefly, chick embryos were transferred from their shells into laboratory weigh boats on the EDD-3 and maintained at 37 °C in a humid incubator until EDD-10. On EDD-10, Caki-1 cells were suspended in Matrigel at a concentration of 10^6 cells per 10 μ L. An abrasion was made using sterile filter paper near a branching vessel of the chick CAM and 10 μ L of the Matrigel/cell mixture was pipetted onto the abraded area. Embryos were immediately returned to the incubator after cancer cell engraftment.

Sunitinib powder was dissolved in dimethyl sulfoxide (DMSO) at a concentration of 10 mM. The stock was further diluted to a 1:1000 ratio in phosphate-buffered saline (PBS) to create a working solution of 10 μ M Sunitinib. DMSO diluted to 1:1000 in PBS was used as a vehicle control. Starting on EDD-12, tumors were treated daily with a topical application of 5 μ L of either the Sunitinib solution or the control solution. The tumor model on CAM assay is depicted in Fig. 3.1. The study began with equally sized treated and control groups; however, only the chicks that survived through endpoint imaging (22 treated tumors, 16 control tumors) were included in the data analysis.

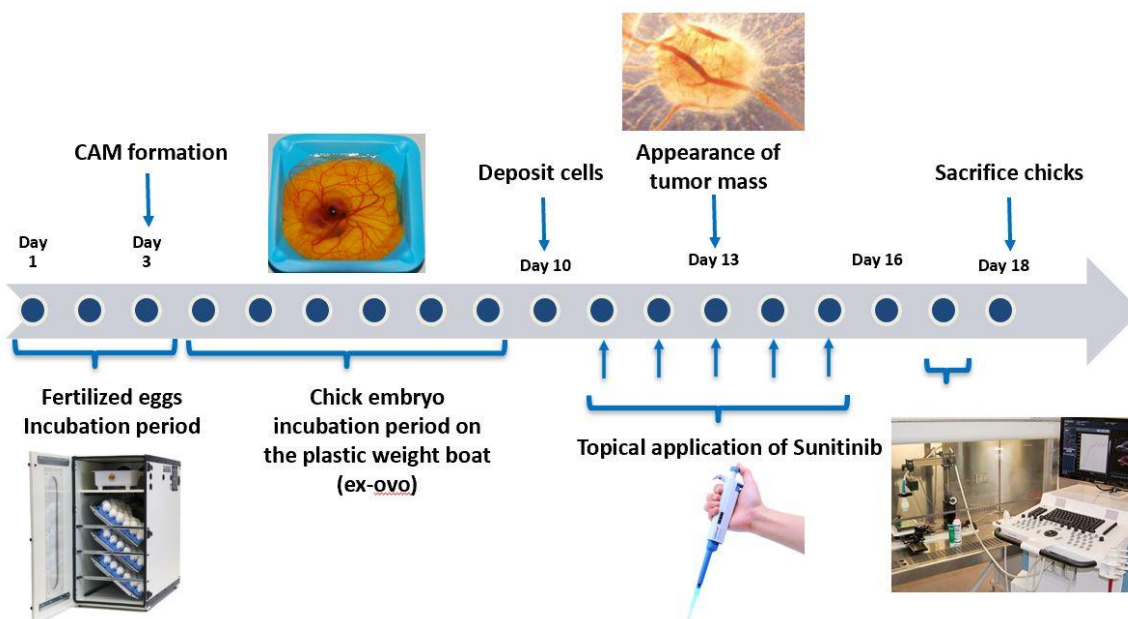


Figure 3.1: Chick CAM Tumor Model and Development Timeline

3.2.3 Power Doppler Image Acquisition and Analysis

At the experimental endpoint on EDD-18, the tumors were imaged using a VisualSonics Vevo 2100 ultrasound system (FujiFilm VisualSonics Inc., Toronto, ON) equipped with Digital RF mode for acquisition of beamformed, quadrature demodulated echo signals. Three-dimensional PD images of the tumor volume and 2D B-mode image sequences, 100 frames in duration, of a cross-section through the center of the tumor were acquired using a 40 MHz linear array (MS-550D). The 3D images were acquired via mechanical translation of the array.

Tumors were manually segmented in all three image types using Vevo Lab analysis software (VisualSonics) to define regions of interest (ROIs) for quantitative analysis. Tumor ROIs in the 3D PD images were used to estimate the tumor volume and VI, which is equal to the proportion of voxels in the ROI with detected blood flow. Clutter filtering of the 3D PD images employed the IIR high-pass filter in the VisualSonics software.

The 2D B-mode sequences were processed in MATLAB (version R2019a, The MathWorks, Natick, MA) using the optimal shrinkage SVD clutter filtering method

described in chapter 2 to construct PD images with enhanced microvessel sensitivity. Vascular network morphological parameters were extracted from the resulting 2D PD images using a vessel skeletonization algorithm, implemented in ImageJ [17], that is similar to [18]. Briefly, the method involves several sequential processing steps for noise and clutter suppression using morphological image processing techniques such as top-hat filtering, erosion, and dilation. A vessel enhancement filter was utilized to enhance tubular structures followed by skeletonization of the binary image. Quantitative vascular metrics, specifically, the NV, NB, and mean VL, were computed by recursively traversing the vessel skeleton.

3.2.4 CEUS Image Acquisition and Analysis

Also, on EDD-18, CEUS imaging was performed after injecting 0.7 mL of a 2×10^9 microbubbles/mL solution of Vevo MicroMarker microbubbles (VisualSonics) suspended in PBS into a large CAM vessel. Destruction-replenishment sequences of 2D subharmonic CEUS images were acquired using a 20 MHz linear array (MS-250). The CEUS image plane was matched to the plane of the 2D B-mode sequence as closely as possible given that it was necessary to move the chick to perform the microbubble injection. Contrast wash-in cine loops were exported as uncompressed intensity signal data files. Tumors were manually segmented in B-mode images to define ROIs for quantitative analysis. The study began with equally sized treated and control groups; however, only the chicks that survived through endpoint imaging (20 treated tumors, 30 control tumors) were included in the data analysis.

In conventional time-intensity CEUS analysis, contrast enhancement was estimated as the mean nonlinear signal intensity within the ROI for each frame of the cine loop. Empirical wash-in time series were constructed to characterize the kinematics of contrast enhancement. Perfusion parameters were derived from the wash-in curves as described below using Vevo Lab (VisualSonics) software. Time-intensity analysis of the 2D CEUS image sequences was performed using Vevo Lab. The resulting perfusion parameters were peak enhancement (correlated with blood volume), time to peak intensity (correlated with blood flow), and the area under the wash-in curve (AUC), which is correlated with intratumoral microvessel density.

The statistical CEUS method [8] analyzes the change in the first-order statistics of the nonlinear intensity signal within the ROI during contrast enhancement. A Lomax distribution,

$$f(I|\alpha, \beta) = \frac{\beta \alpha^\beta}{(I+\alpha)^{\beta+1}} \quad (3.3)$$

which approximates a compound distribution of exponential PDFs weighted by a log-normal function [19], is fit to the histogram of the nonlinear signal intensity, I , in each frame via maximum likelihood estimation. The compound distribution's weighting function, $w(\theta)$, is estimated for each frame from the hyperparameters of the Lomax distribution, α and β , via [19]:

$$w(\theta|\alpha, \beta) = \frac{\alpha^\beta}{\Gamma(\beta)} \theta^{\beta-1} e^{-\alpha\theta} \quad (3.4)$$

where θ is the scale parameter of the exponential PDF in (3.2). Enhanced tumor fraction at time t is defined as one minus the normalized area of overlap between $w(\theta)$ at t and $w(\theta)$ estimated from the baseline unenhanced image. An empirical wash-in time series is constructed by plotting enhanced tumor fraction as a function of time during microbubble replenishment. Statistical CEUS analysis was performed using MATLAB.

For both conventional and statistical CEUS, wash-in curves were characterized by fitting a monoexponential function, $A(1 - e^{-t/\tau})$, to the empirical wash-in time series. Peak enhancement (PE, equal to A), rise time (defined here as the time the fitted curve reaches $0.95A$, which equals 3τ), wash-in rate (defined as the ratio PE/rise time), and the area under the wash in curve (AUC, computed from $t = 0$ to $t = 3\tau$) were estimated from the fitted wash-in curves for conventional CEUS. PE, rise time, and AUC were similarly estimated from the statistical method's wash-in curves. Pearson correlation coefficients were computed for each pair of wash-in curve parameters.

3.2.5 Classification and Feature Selection Algorithms

Image features were used as inputs to a support vector machine (SVM) and multi-variable logistic regression classifiers implemented in Python that were trained to output a binary classification of each tumor as sensitive or resistant to Sunitinib. Data were centered and

scaled before being input to the classifier. Supervised machine learning was employed where the treated tumors were assumed to be sensitive, and the control specimens were assumed to model resistant tumors. Leave-one-out cross validation was used to avoid overfitting due to the modest sample size.

For the assessment of the developed model based on ultrasound microvascular parameters, different classifiers using different combinations of input features were trained: the first model used tumor volume and the three CEUS features (peak enhancement, time to peak, AUC), the second one used tumor volume and the four PD features (VI, NV, NB, VL), the third model used the best performing combination of features determined using backward elimination feature selection, and the fourth model used all eight features.

On the other hand, to evaluate the effectiveness of statistical analysis of CEUS in discriminating treated and untreated tumors, the seven features of PE, rise time, wash-in rate, and the AUC estimated from the fitted wash-in curves for conventional CEUS and PE, rise time, and AUC from the statistical method's wash-in curves, were used as inputs to SVM and multi-variable logistic regression classifiers. Three different models using different combinations of input features were trained with each classification algorithm: the first model used only the four features from conventional CEUS analysis (PE, wash-in rate, rise time, and AUC), the second model used only the three features from statistical CEUS analysis (PE, rise time, and AUC), and the third model included all seven features.

Classifier performances were evaluated by computing their accuracy, sensitivity, specificity, and receiver operating characteristic (ROC) curves for identifying treated tumors. Ten-fold cross-validation was used for performance evaluation to avoid overfitting due to the modest sample size. Separately from the performance evaluations, three feature selection algorithms: principal component analysis, forward feature selection, and backward feature elimination using logistic regression, were applied to the complete set of seven features to identify the most important features for treatment response classification.

Table 3.1: Perfusion parameters from conventional PD, optimal shrinkage SVD filtered PD images, conventional CEUS as well as tumor volume.

Feature	Imaging technique	Sunitinib (treated)	DMSO (control)
Tumor volume [mm ³]	3D PD	10.6 ± 2.7	17.4 ± 7.6
Vascularization index	2D PD	3.7 ± 2.7	9.4 ± 2.5
Time to peak [s]	2D CEUS	5.0 ± 4.2	5.4 ± 4.5
Peak enhancement [a.u.]	2D CEUS	1.4 ± 1.8	4.8 ± 2.8
Area under the time-intensity curve [a.u.]	2D CEUS	2.6 ± 2.0	8.4 ± 4.4
Number of vessels	SVD-filtered PD	25.6 ± 8.2	59.8 ± 16.5
Number of branching points	SVD-filtered PD	19.8 ± 5.4	35.3 ± 8.2
Mean vessel length [□m]	SVD filtered PD	168 ± 19	181 ± 121

3.3 Results

3.3.1 Power Doppler and CEUS Vascular Parameters

Table 3-1 lists the means and standard deviations of the vascular parameters for 22 treated tumors and 16 control tumors that were estimated using each imaging method. A general trend of lower vascularity and smaller tumors was observed in the treated group compared to the control group. Therefore, the Caki-1 cell line exhibited the expected high level of Sunitinib sensitivity and the experimental design successfully produced two groups of tumors with distinctly different vascular architecture and perfusion.

Figure 3.2 shows CEUS images of the same control tumor, outlined in green, taken at baseline (panel a) and at peak enhancement (panel b), while panel c shows that tumor's wash-in curve from the statistical analysis and demonstrates that the reperfusion kinematics of the statistical method's enhanced tumor fraction estimate conform closely to the assumed monoexponential curve shape.

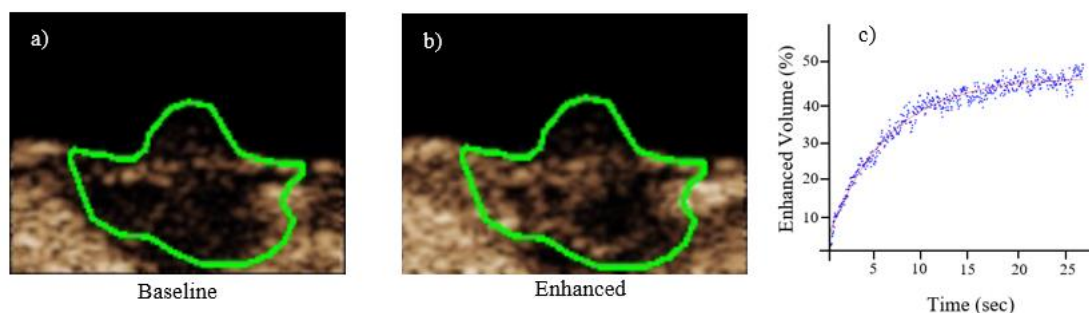


Figure 3.2: Nonlinear contrast-enhanced ultrasound (CEUS) images of a control tumor engrafted on the CAM of a chick embryo. a) Baseline image. b) Image at peak enhancement. The manually segmented tumor boundary is shown in green in both images. The field of view is 3.5 mm lateral \times 3.7 mm axial. c) Statistical CEUS destruction-replenishment data (blue dots) and fitted monoexponential wash-in curve (red line) for the same tumor.

Table 3-2 lists the means and standard deviations of the perfusion parameters for 20 treated tumors and 30 control tumors that were used as inputs to the classifiers. A consistent trend of lower vascularity was observed via the lower PE and AUC in the treated group compared to the control group. Therefore, the Caki-1 cell line exhibited the expected high level of Sunitinib sensitivity. Also, note that the different units used for PE in the conventional and statistical methods result in a larger dynamic range for both PE and AUC in statistical CEUS compared to conventional CEUS. Among all pairs of perfusion parameters, the highest Pearson correlation coefficients were between AUC from statistical analysis and AUC of conventional analysis, AUC from statistical analysis and PE of conventional analysis (both at 0.77), and AUC of conventional analysis and PE of conventional analysis at 0.80.

Table 3.2: Perfusion parameters from conventional and statistical analysis of CEUS

Feature	Imaging technique	Sunitinib (treated)	DMSO (control)
PE [a.u.]	Conventional CEUS	2.0 ± 1.7	6.4 ± 3.3
Rise Time [s]	Conventional CEUS	5.9 ± 4.5	6.5 ± 4.4
AUC [a.u.]	Conventional CEUS	7.7 ± 5.3	11.0 ± 4.9
Wash-in rate [a.u.]	Conventional CEUS	3.4 ± 1.8	6.7 ± 5.0
PE [%]	Statistical CEUS	2.4 ± 1.8	16.0 ± 9.4
Rise Time [s]	Statistical CEUS	12.8 ± 7.5	8.4 ± 5.2
AUC [%xs]	Statistical CEUS	15.4 ± 8.3	93.3 ± 32.7

3.3.2 Tumor Treatment Classification Response

Table 3.3 reports the classification performance for the four logistic regression models. In this data, a Sunitinib-sensitive classification was treated as a “positive” decision for purposes of defining sensitivity and specificity. The best-performing classifier used VI from 3D conventional PD images and two features, NV and NB, from 2D SVD-filtered PD images. The model that considered tumor volume and all four PD features yielded the second-best performance, the model using tumor volume and the three CEUS features was the third most accurate, and the model that included all eight features was the lowest performing classifier.

Table 3.3: Classification results using only perfusion parameters from conventional CEUS

	Model	Accuracy	Sensitivity	Specificity
1	Volume + conventional CEUS-based features	84%	86%	81%
2	Volume + SVD-filtered PD-based features	89%	86%	94%
3	Best combination of features (VI, NV, NB)	95%	95%	94%
4	All features	82%	86%	75%

3.3.3 CEUS + conventional PD and optimal shrinkage SVD-filtered PD analysis

Figure 3.3 shows a scatter plot of two of the three features incorporated into the best performing classifier to illustrate the inter-tumor variability of the most important features. The background shading highlights the boundary between the sensitive (light blue) and resistant (pink) decision regions. The high classification accuracy depicted in the figure is consistent with the performance metrics listed in Table 3.2 for Model #3.

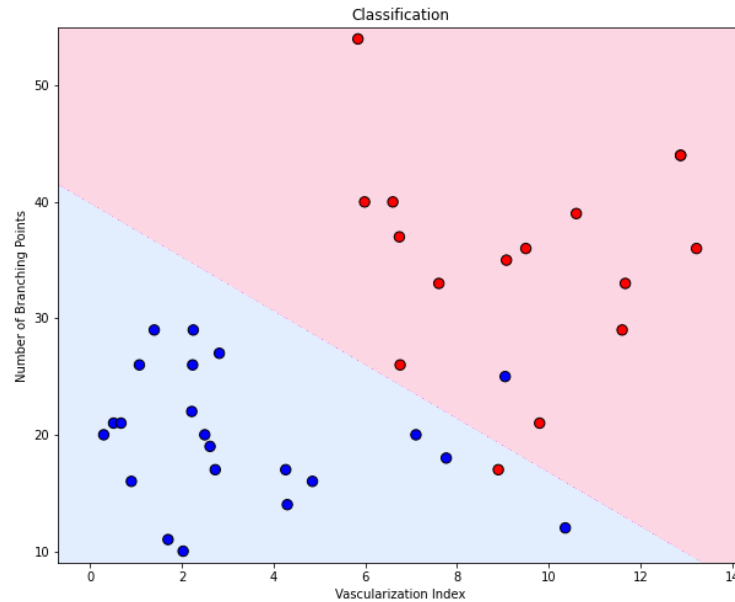


Figure 3.3: Scatter plot of vascularization index and number of branching points for Sunitinib-treated (blue circles) and DMSO-control red circles) tumors. The background shading highlights the decision boundary.

Table 3.4 reports the classification performance for the three learning models using perfusion parameters estimated from conventional analysis, from statistical analysis, and both methods as inputs to logistic regression (top 3 rows) and SVM (bottom 3 rows) classifiers. The best-performing model, for both classification algorithms, contained all perfusion features estimated from both CEUS methods. The models that considered only features from statistical CEUS yielded modestly higher performance than the conventional CEUS models for both classification algorithms.

Table 3.4: Classification performance for comparing the usefulness of conventional and statistical analysis of CEUS

	Model	Accuracy	Sensitivity	Specificity
1	Logistic Regression + Conventional CEUS features	0.86	0.85	0.86
2	Logistic Regression + Statistical CEUS features	0.88	0.90	0.86
3	Logistic Regression + All CEUS features	0.90	0.90	0.86
4	Support Vector Machine + Conventional CEUS features	0.86	0.95	0.79
5	Support Vector Machine + Statistical CEUS features	0.90	1.00	0.83
6	Support Vector Machine + All CEUS features	0.92	1.00	0.86

Figure 3.4 shows the ROC curves for the three logistic regression classifiers in table 3-5. Consistent with the results in Table 3-6, the classifier containing all perfusion parameters from both conventional and statistical CEUS (shown in purple) yielded the highest area under the ROC curve, 0.95. The areas under the ROC curves for the classifiers using only statistical and only conventional CEUS features were 0.94 and 0.91, respectively. The ROC curves for the SVM classifiers (not shown) were like the logistic regression ROC curves.

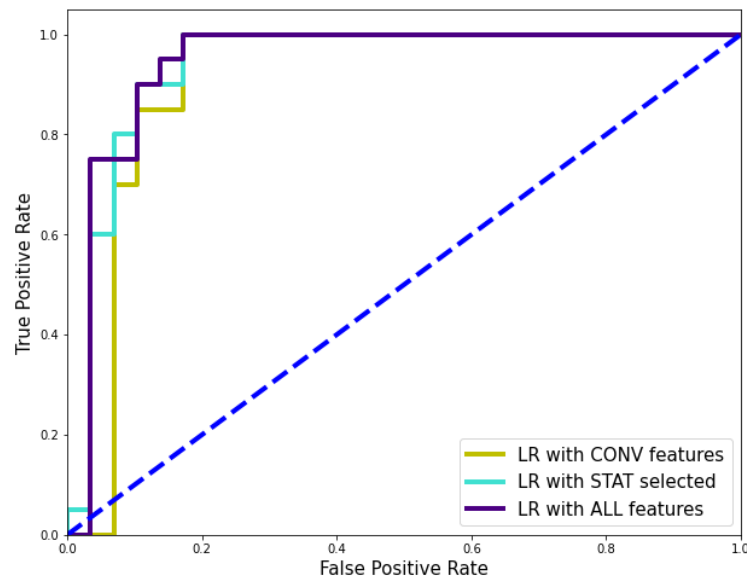


Figure 3.4: Receiver Operating Characteristic curves of three logistic regression models with different combination of CEUS perfusion parameters

3.3.4 Feature Selection

Table 3.5 lists the features selected using three different algorithms. The results indicate that AUC is consistently selected from conventional and statistical CEUS features and thus is identified as an important parameter for detecting antiangiogenic responses in the CAM assay. Each feature selection algorithm retained at least one feature from both conventional and statistical CEUS.

Table 3.5: Feature Selection Results on all conventional and statistical CEUS perfusion parameters

Feature Selection Algorithm	Conventional CEUS	Statistical CEUS
Backward feature elimination	AUC, Rise time	AUC, PE
Forward feature selection	AUC, PE	AUC
Principal component analysis	AUC, Rise time	AUC

3.4 Discussion

3.4.1 Scalable Preclinical Model for Tumor Treatment Response Evaluation

In this chapter, a scalable and efficient method to model the tumor and evaluate its treatment response based on perfusion parameters derived from ultrasound image analysis was presented. The objectives of the paper were to demonstrate the effectiveness of the chick CAM assay for assessing the marginal utilities of employing additional ultrasound imaging modes and of extracting additional image features. The classification performances reported in table 3.3 suggest that, for this Caki-1 tumor model, there is little additional benefit to acquiring 2D CEUS images when 2D SVD-filtered PD images are also available.

On the other hand, 3D vascular images, even if they are acquired using conventional PD with lower vessel sensitivity than SVD-filtered PD, do provide valuable additional information about tumor blood flow. Similarly, the comparison of the best performing classifier (model #3 in Table 3.3) to the tumor volume + PD features classifier (model #2 in Table 3.3) illustrates the use of the platform to assess the utility of additional image

features. In this case, there was no benefit to adding tumor volume and mean vessel length to the three PD features (VI, NV, and NB) that were included in model #3.

In addition to the low cost of the CAM assay cited in the introduction, the relatively high imaging throughput of the assay is another source of its scalability and efficiency. The image acquisition performed for this study required about 15 minutes per tumor with two investigators working together (one to operate the scanner and the second to perform the microbubble injections), so the 38 tumors used to train and validate the classifiers required slightly less than 20 person hours of imaging time. Imaging the CAM model is substantially faster than imaging a murine model because the tumor is clearly visible on the CAM surface and because many of the animal care steps required for murine ultrasonography (*e.g.*, induction of anesthesia, depilation of the imaging site, recovery from anesthesia) are not needed with the CAM model.

The observations reported above about the relative utilities of the various image features are not intended as generalized recommendations for ultrasound cancer imaging, but it is possible to identify aspects of this specific experiment that contributed to the patterns in our data. First, the optimal shrinkage SVD clutter filter significantly improves PD sensitivity to small vessels, so it is unsurprising that the feature selection method preferred features from those images. On the other hand, 3D imaging facilitated tumor segmentation, especially in cases where the tumor margin was ambiguous in the 2D planes of the SVD-filtered PD and CEUS images. The 3D PD image also provided a holistic view of tumor blood flow that complements the higher vessel sensitivity in one plane obtained from the 2D images. This reasoning suggests that the ideal experimental protocol would include 3D SVD-filtered images, but the Vevo 2100 does not support that technique because the mechanical probe translation employed for 3D imaging provides either one acquisition per plane (3D B-mode) or 13 acquisitions per plane (3D PD), but not the long ensembles of ~ 100 pulses needed for SVD processing.

The limited utility of the CEUS features in the logistic regression classifiers observed in Table 3.3 was not anticipated. We suspect that this observation reflects recognized sources of variability in CEUS imaging [20] exacerbated by the difficulty of performing consistent

microbubble injections in the delicate CAM vessel network. Due to the latter problem, there were some tumors for which PD images, but no CEUS images, were acquired. This factor contributed to the unequal group sizes in the data analysis.

The significant difference in treated versus control endpoint tumor volumes may be surprising considering that Sunitinib is viewed as a cytostatic agent. However, the Sunitinib concentration used in this study was higher than the clinical dose, which is $< 1 \mu\text{M}$. Similarly high Sunitinib concentrations have been observed to slow Caki-1 tumor growth both in vitro and in murine xenografts. Furthermore, in our experiment, treatment was initiated at a relatively early stage of tumor growth, thereby preventing angiogenesis and restricting growth, rather than remodeling an established tumor vascular network.

Logistic regression was used as the learning model for the classifiers. Logistic regression is formulated for binary classification problems involving independent observations of continuous variables. Both of those assumptions were satisfied in our data: the data set was constructed from image parameters estimated from different tumors and the high precision of the parameter estimates made them effectively continuous variables. Moreover, SVM classifier was used due to its capabilities in performing well with small sample sizes. Also, SVM is a robust algorithm that is less affected by outliers than other classifiers.

This experiment was designed as a preliminary study to demonstrate the CAM assay + high-frequency ultrasound platform. Therefore, we chose a mRCC cell line that is known to be highly sensitive to Sunitinib [21] to ensure that we obtained two tumor groups with distinct blood flow characteristics. A more complete evaluation of the platform would include more cell lines (this study design is used in chapter 4) and/or additional therapeutic agents to obtain a greater diversity of treatment responses. Furthermore, the classifier performance results reported above were obtained via leave-one-out cross-validation. A more rigorous evaluation would employ independent data sets for validation and testing of the classifiers.

3.4.2 Utility of a Statistical CEUS Analysis for Tumor Response Evaluation

Moreover, in this chapter, we investigated the utility of a statistical CEUS analysis method for detecting tumor responses to anti-angiogenic treatment. The statistical method was assessed in comparison to a conventional method of dynamic CEUS analysis. The comparison showed that the relative performance of conventional CEUS, statistical CEUS, and hybrid classifiers is consistent with different classification algorithms. Using both logistic regression and SVM classifiers, a hybrid model including features from both CEUS methods outperforms models containing only conventional or statistical CEUS parameters (Table 3.4 and Fig. 2). Moreover, when the feature selection methods listed in Table 3.5 were applied to the hybrid model, parameters from both conventional and statistical CEUS were consistently retained. Therefore, the results suggest that statistical CEUS supplements the information obtained from conventional CEUS, such that statistical CEUS is best employed in combination with conventional CEUS rather than as a stand-alone replacement for the conventional method.

Two learning models, logistic regression and SVM, were employed to demonstrate that the classification results are consistent for learning models with different strengths. Logistic regression is an effective learning model that is easy to implement without the need to tune its hyperparameters. The high precision of the CEUS parameter estimates made them effectively continuous variables, which satisfies a key assumption of logistic regression. On the other hand, the experimental data included CEUS feature samples with very high variation from their means that may be considered outliers. Therefore, SVM was used because it exhibits low sensitivity to outliers in its classification performance.

Area under the wash-in curve appears to be a particularly important parameter for detecting anti-angiogenic responses in a CAM assay because both the conventional and statistical CEUS estimates of AUC were retained by all three feature selection methods. In destruction replenishment studies, the AUC of a mean-intensity wash-in curve is correlated with microvessel density and the AUC for the statistical method's enhanced tumor fraction wash-in curve is also sensitive to microvessel density [8]. It is unclear whether this association of AUC with microvessel density holds for destruction-replenishment studies

using statistical CEUS, but if so, this observation would be consistent with the expectation that the treated tumors should exhibit reduced vascularity compared to the control tumors.

Feature selection algorithms typically assess the individual importance of features in relation to the target variable. By applying basic algebraic calculations, it is possible to easily compute the AUC using the values of two other features, namely PE and RT. Here, AUC is the feature that was selected from both conventional and statistical CEUS using all three feature selection algorithms employed. The construction of AUC as a feature enables the capturing of valuable information that is not fully represented by its constituent features alone (PE and RT). Consequently, the feature selection algorithms pick AUC as an informative feature about intra-tumor microvasculature and thus in treatment response classification. The inclusion of AUC, as a constructed feature that incorporates the interaction effects between PE and RT, has demonstrated its potential to enhance the performance of the model. Hence, it can be inferred that AUC is preferable over PE and RT when analyzed separately, as it effectively represents both of these parameters within a single feature in CEUS image analysis.

In the original development of the statistical method [8], a Lomax distribution to approximate the first-order statistics of CEUS intensity was justified by assuming that the weighting function in (3.1) would have the same form as the distributions of vessel diameters and velocities in a microvessel network, which are both log-normal given a fractal network architecture [22]. Subsequently, Parker and Poul [23] demonstrated that a Lomax distribution also approximates the first-order speckle statistics produced by scattering from a fractal microvessel network. Since nonlinear CEUS images emphasize signals from microbubbles, which are confined to the intravascular space, Parker and Poul's calculations provide an additional analytical foundation for our statistical CEUS approach.

The complete set of classifier features was unbalanced (four conventional CEUS parameters, three statistical CEUS parameters) because wash-in rate was not included among the statistical parameters. Wash-in rate was excluded from the statistical features because its variability was anomalously high (mean \pm standard deviation of 1.9 ± 1.65 and

20.2 \pm 17.9 for treated and control tumors, respectively), so this feature would have interfered with classifier performance. The source of the high variability in the statistical CEUS wash-in rate requires further investigation.

3.5 Conclusion

In addition to the application to imaging algorithm development demonstrated here, this platform may also be employed for preclinical cancer research. When using established cell lines for drug development studies, the CAM assay provides an alternative to in vitro cell-line panels or tumor spheroid preparations that retains the efficiency of those techniques while also acting as a biologically relevant model of tumor angiogenesis [4]. High-frequency ultrasound is ideal for imaging the fragile CAM models and can provide accurate, nondestructive 3D measurements of tumor volume and perfusion that are difficult to obtain using more conventional laboratory methods. The biological fidelity of the CAM assay can also be increased by using patient-derived cell lines or tumor xenografts [24] to reproduce the intra- and intertumoral heterogeneity of clinical cancers.

Moreover, the effectiveness of CEUS perfusion features for discriminating highly treatment sensitive tumors from untreated tumors was investigated. A more comprehensive study should include additional cell lines exhibiting different degrees of treatment sensitivity, including resistant and partially sensitive cell lines, and/or additional therapeutic agents to obtain a greater diversity of treatment responses. Perfusion parameters from power Doppler and other contrast-free microvascular imaging techniques could also be included to obtain a more convincing assessment of the utility of the statistical CEUS method, *e.g.*, by testing whether statistical CEUS parameters are still retained when the feature selection algorithms are presented with more options. Furthermore, classifier performance should be evaluated using independent data sets for validation and testing rather than the cross-validation approach employed here.

References

- [1] C. Demené, *et al.*, "Spatiotemporal clutter filtering of ultrafast ultrasound data highly increases Doppler and fUltrasound sensitvitiy", *IEEE Transaction in Medical Imaging*, vol. 34, pp. 2271- 2285, 2015.
- [2] C. Errico, *et al.*, "Ultrafast ultrasound localization microscopy for deep super-resolution vascular imaging", *Nature*, vol. 527, pp. 499-502, 2015.
- [3] C. H. Leow, *et al.*, "3-D Microvascular Imaging Using High Frame Rate Ultrasound and ASAP Without Contrast Agents: Development and Initial In Vivo Evaluation on Nontumor and Tumor Models", *IEEE Transactions on Ultrasonics, Ferroelectrics, and Frequency Control*, vol. 66, no. 5, pp. 939-948, May 2019
- [4] M.S. Gee, *et al.*, "Doppler ultrasound imaging detects changes in tumor perfusion during antivascular therapy associated with vascular anatomic alterations", *Cancer Research*, vol. 61, no. 7, Apr. 2001
- [5] K. W. Ferrara, *et al.*, "Evaluation of tumor angiogenesis with US: Imaging, Doppler, and contrast agents", *Academic Radiology*, vol. 7, no. 10, pp. 824-839, 2000
- [6] S. Sabeti, *et al.*, "A Morphometric analysis of tumor microvessels for detection of hepatocellular carcinoma using contrast-free ultrasound imaging: A feasibility study", *Frontiers in Oncology*, vol. 13, Apr. 2023
- [7] J. M. Hudson, *et al.*, "Dynamic contrast enhanced ultrasound for therapy monitoring", *European Journal of Radiology*, vol. 84, no. 9, pp.1650-1657, 2015
- [8] M.R. Lowerison, *et al.*, "Compound speckle model detects anti-angiogenic tumor response in preclinical nonlinear contrast-enhanced ultrasonography", *Medical Physics*, vol. 44, no. 1, pp. 99-111. Jan. 2017
- [9] P. Lambin, *et al.*, "Radiomics: The bridge between medical imaging and personalized medicine", *Nature Review Clinical Oncology*, vol. 14, pp. 749-762, 2017
- [10] A.C. Tufan and N.L. Satiroglu-Tufan, "The chick embryo chorioallantoic membrane as a model system for the study of tumor angiogenesis, invasion and development of anti-angiogenic agents", *Current Cancer Drug Targets*, vol. 5, no. 4, pp. 249-266, 2005
- [11] M.R. Lowerison, *et al.*, "Ultrasound localization microscopy of renal tumor xenografts in chicken embryo is correlated to hypoxia", *Science Reports*, vol. 10, 2020
- [12] K.S. Han, *et al.*, "Cellular adaptation to VEGFtargeted antiangiogenic therapy induces evasive resistance by overproduction of alternative endothelial cell growth factors in renal cell carcinoma", *Neoplasia*, vol. 17, pp. 805-816, 2015.

- [13] J.J. Hsieh, *et al.*, "Renal cell carcinoma", *Nature Review Disease Primers*, vol. 3, art. 17009, 2017
- [14] Turco S, *et al.*, "Contrast-Enhanced Ultrasound Quantification: From Kinetic Modeling to Machine Learning", *Ultrasound in Medicine Biology*, vol. 46, no. 3, pp. 18-543. 2020
- [15] T.J. Freeman, *et al.*, "Inhibition of Pannexin 1 reduces the tumorigenic properties of human melanoma cells", *Cancers*, vol. 11, art. 102, 2019
- [16] M. Bataghva, *et al.*, "Contrast-free ultrasound microvascular imaging with optimal clutter shrinkage to enhance tumor vascular quantification", *IEEE Ultrasonic Symposium.*, 2020
- [17] M.D. Abramoff, *et al.*, "Image processing with ImageJ", *Biophotonics International*, vol. 11, no. 7, pp. 36-42, 2004.
- [18] S. Ghavami, *et al.*, "Quantification of morphological features in non-contrast-enhanced ultrasound microvasculature imaging", *IEEE Access*, vol. 8, pp. 18925-18937, 2020.
- [19] S.D. Dubey, "Compound gamma, beta and F distributions", *Metrika* , vol. 16, pp. 27–31, 1970
- [20] M.X. Tang, *et al.*, "Quantitative contrast enhanced ultrasound imaging: A review of sources of variability", *Interface Focus*, vol. 1, pp. 520-539, 2011
- [21] K.S. Han, *et al.*, "Cellular adaptation to VEGF targeted antiangiogenic therapy induces evasive resistance by overproduction of alternative endothelial cell growth factors in renal cell carcinoma", *Neoplasia*, vol. 17, pp. 805-816, 2015.
- [22] H. Qian and J. B. Bassingthwaite, "A Class of Flow Bifurcation Models with Lognormal Distribution and Fractal Dispersion", *Journal of Theory Biology*, vol. 205, pp. 261-268, 2000
- [23] K. J. Parker, *et al.*, "Correlation of Real-time Gray Scale Contrast-Enhanced Ultrasonography With Microvessel Density and Vascular Endothelial Growth Factor Expression for Assessment of Angiogenesis in Breast Lesions", *Ultrasond Imaging*, vol. 42, pp. 203–212, 2020.
- [24] L.C. DeBord, *et al.*, "The chick chorioallantoic membrane (CAM) as a versatile patient-derived xenograft (PDX) platform for precision medicine and preclinical research", *The American Journal of Cancer Research*, vol. 8, pp. 1642-1660, 2018

Chapter 4

4 Generalization of Multiparametric Microvascular Ultrasound Models to Assess Tumor Response to Anti-Angiogenic Treatment

The contents of this chapter have partially been adapted from

*"Multiparametric Microvascular Ultrasound to Classify Tumor Sensitivity to Anti-Angiogenic Treatment: Application to Multiple Cell Lines", published in IEEE International Ultrasonics Symposium (IUS), Venice, Italy, pp. 1-4, 2022 by M. Bataghva, D. Johnston, N. Power, A. Ward, S. Penuela and J. C. Lacefield**

*© 2022 IEEE. Reprinted, with permission, from M. Bataghva, D. Johnston, N. Power, A. Ward, S. Penuela and J. C. Lacefield, "Multiparametric Microvascular Ultrasound to Classify Tumor Sensitivity to Anti-Angiogenic Treatment: Application to Multiple Cell Lines", IEEE International Ultrasonics Symposium (IUS), Las Vegas, NV, USA, pp. 1-4

4.1 Introduction

Although the effectiveness of PD and CEUS imaging for evaluating tumor angiogenesis has been widely studied, it is difficult to definitively establish the best combination of PD and CEUS perfusion parameters for a specific application [1]. In chapter 1 of this thesis, we discussed the limitation of conventional PD and CEUS in microvascular detection and therefore, to improve the reliability of ultrasound estimates of tumor perfusion, our lab has developed a PD clutter filtering method that employs optimal shrinkage of singular values [2] (Chapter 2) and a CEUS method that analyzes the change in the first-order statistics of contrast signal intensity during a destruction replenishment sequence [3]. The optimal shrinkage clutter filter is an SVD method that reweights intermediate singular vectors to compensate for overlap of blood and clutter signal components in the eigen domain. The statistical CEUS method is designed to characterize spatially heterogeneous contrast enhancement more effectively than is possible with methods that only consider the mean contrast signal intensity.

The objective of this study is to conduct a more comprehensive study of Ultrasound-based perfusion parameters in tumor antiangiogenic treatment response with parameters from both conventional and developed PD and CEUS and identify the best combination of features and also evaluate the generalization capabilities of the model pipeline with the best combination of perfusion parameters. Therefore, in this chapter, we first, assessed the usefulness of the perfusion parameters from SVD-based optimal shrinkage clutter filtered PD and statistical histogram-based CEUS images, compared to perfusion parameters from conventional PD and mean-intensity-based CEUS images, in improving the antiangiogenic tumor treatment response classification of cell lines with differing sensitivity level. Secondly, to evaluate the robustness and generalization capabilities of the model pipeline, an independent set of tumors whose treatment sensitivity was unknown to the model was tested.

4.1.1 A more comprehensive study with more perfusion parameters to classify resistant and sensitive tumors to antiangiogenic treatment

In chapter 3, we observed that classical machine learning classifiers (*i.e.*, using logistic regression or support vector machine, SVM) that included a combination of perfusion parameters from PD using a conventional IIR clutter filter, PD using the more familiar truncated SVD method (*i.e.*, rather than optimal shrinkage) for spatiotemporal clutter filtering, and conventional mean-intensity-based CEUS analysis provided the highest sensitivity and specificity to tumor anti-angiogenic treatment response compared to classifiers that included features from only one or two of those imaging modes. Also in chapter 3, we demonstrated that a combination of features from conventional and statistical CEUS was also more sensitive to anti-angiogenic treatment response than classifiers that incorporated features from only conventional or only statistical CEUS. The experiments in chapter 3 employed a preclinical tumor model consisting of an established renal cell carcinoma (RCC) cell line, Caki-1, implanted onto the CAM of *ex-ovo* chicken embryos and compared images of untreated and treated tumors to tumors.

This study builds upon chapter 3 by incorporating both optimal shrinkage SVD PD and statistical CEUS into the treatment-response classifier and by challenging the classifier with tumors from two RCC cell lines (Caki-1 and ACHN) with differing drug sensitivity. The objectives of this study are to obtain a more complete assessment, compared to the simpler experimental designs of chapter 3, of whether (1) the high vessel sensitivity of PD with SVD clutter filtering is sufficient to avoid the need for more expensive and more technically difficult CEUS techniques when assessing tumor antiangiogenic responses and (2) whether, if CEUS is indicated, our statistical CEUS method should be preferred to or used in combination with conventional CEUS analysis.

4.1.2 Evaluate classification performance on an independent tumor

Moreover, evaluating the performance of a classification algorithm on a separate test set is essential for several reasons. Firstly, it allows for an unbiased estimation of performance. When developing a classification algorithm, it is common to use the cross-validation method, to test its performance. If the same data is used for both training and testing, the

algorithm may overfit the training data, meaning it will perform well on the training data but poorly on new, unseen data. Evaluating the algorithm on a separate test set ensures that the performance estimates are unbiased, as the algorithm has not seen this data during training.

Secondly, evaluating the algorithm on a separate test set allows for an assessment of its ability to generalize to new data, ensuring the generalization of performance. A classification algorithm that performs well on a particular dataset does not necessarily perform well on new, unseen data. By evaluating the algorithm on a separate test set, we can assess its ability to generalize to new data and get a more accurate estimate of its true performance.

Thus, to evaluate the robustness and generalization capabilities of the model pipeline, we used an independent set of tumors whose treatment sensitivity was unknown to the model. We trained the classifier using two tumor cell lines with distinct (high and low) treatment sensitivity and assessed its performance for a third, independent cell line.

4.1.3 Study Design

As in chapter 2 and 3, we again employ the *ex-ovo* chick CAM tumor model due to its high-throughput capability. The use of established cell lines is appropriate for the goals of this study because each cell line produces a population of tumors that are initially genetically identical, so data may be pooled over multiple serial experiments to accumulate large sample sizes within a few weeks. The resulting uniformity of tumors from the same cell line is desirable because our emphasis is on performance assessment of perfusion parameters from the ultrasound techniques, we introduced in chapter 2 and 3, so we wish to avoid the inter-tumor biological variability that might confound experiments with more clinically relevant models such as patient-derived tumor specimens.

Also, as in chapter 2 and 3, Sunitinib, an approved first-line systemic therapy for metastatic RCC, is the drug used in this study. The Caki-1 cell line used in the study exhibits high sensitivity to Sunitinib [6] while ACHN demonstrates little response to Sunitinib [7] and parental 786-O showed moderate sensitivity to Sunitinib antiangiogenic treatment [8].

An experiment in which eight different treatment-sensitivity classifiers were constructed by feature selection beginning from a maximum of twelve inputs is presented. The available features were endpoint tumor volume from 3D ultrasound; VI from 2D conventional PD; three vascular network morphology features (NV, NB, and mean VL) from 2D SVD-filtered PD; four parameters of PE, RT, WIR, and AUC from mono-exponential wash-in curves fit to mean-intensity time series from conventional CEUS; and three analogous parameters (PE, TTP, and AUC) from mono-exponential wash-in curves obtained from the statistical CEUS method.

Four feature sets were used in classification models trained using each of logistic regression and SVM: (1) features from conventional PD and CEUS only, (2) features from SVD-filtered PD and statistical CEUS only; (3) the most informative features as determined the backward elimination feature selection, and (4) all 12 features. Moreover, the SVM classifier performance on an independent set of tumors using all 12 perfusion parameters and only the selected set of most informative features were evaluated.

Classification performance was evaluated via the accuracy, sensitivity, specificity, and area under the receiver operating characteristic curve (AROC) for discriminating sensitive from resistant tumors. The relative importance of the individual features was also compared by computing their Shapely additive explanations (SHAP) values [9]. The results highlight the diagnostic potential of optimal-shrinkage-SVD-filtered PD and statistical CEUS analysis.

To evaluate model pipeline robustness, we trained the classifier using two tumor above-mentioned cell lines with distinct (high and low) treatment sensitivity and used it to classify a third, independent cell line (i.e., 786-O mRCC cells). A SVM classifier was trained with tumor samples from ACHN and Caki-1 cells and tested using twenty 786-O tumor samples. The SVM's performance was evaluated based on its ability to identify 786-O tumors as Sunitinib-resistant.

4.2 Materials and Methods

4.2.1 Tumor Model Experiment

Caki-1, ACHN and 786-O kidney tumor cells (American Type Culture Collection, Manassas, VA) were engrafted onto CAMs of ex ovo chicken embryos near a branching vessel following the protocol described in [4]. Where Caki-1 and ACHN are metastatic RCC cell lines while 786-O is a cell line from primary site [10]. It is important to note that both Caki-1 and 786-O are clear cell RCC tumor cells while ACHN is the papillary RCC [10]. Starting on embryonic development day 12 (EDD-12), each group of tumors was treated by topical application of 5 μ L of a 10 μ M Sunitinib solution.

The study began with equal treated tumor sample for Caki-1, ACHN and 786-O groups; however, only the chicks that survived through endpoint imaging on EDD-18 (20 Caki-1 tumors, 25 ACHN tumors and 20 786-O) were included in the data analysis. Tumors were imaged using a VisualSonics Vevo 2100 ultrasound system (FujiFilm VisualSonics Inc., Toronto, ON) equipped with Digital RF mode for acquisition of beamformed, quadrature demodulated echo signals.

4.2.2 Image Acquisition and Feature Analysis

Three-dimensional PD images of the tumor volume were acquired using a 40 MHz linear array (MS-550D) via mechanical translation of the array. 2D B-mode image sequences, 100 frames in duration, of a cross-section through the center of the tumor were also acquired using the 40 MHz array. CEUS images were acquired after injecting 0.7 mL of a 2×10^9 microbubbles/mL solution of Vevo MicroMarker microbubbles (VisualSonics) suspended in PBS into a large CAM vessel. Destruction-replenishment sequences of 2D subharmonic CEUS images were acquired using a 20 MHz linear array (MS-250). Regions of interest (ROIs) for image analysis were defined via manual segmentation of the tumors using Vevo Lab analysis software (VisualSonics). VI was also computed for the conventional PD images using Vevo Lab.

The 2D B-mode sequences were processed in MATLAB (version R2019a, The MathWorks, Natick, MA) using the optimal shrinkage SVD clutter filtering method

described in chapter 2. Briefly, the B-mode frames were extracted from a cine loop and combined into a 2D Casorati matrix. A singular value shrinkage function optimized for Frobenius norm loss [11, Eq. 7] was employed to isolate the most coherent data component. Subtraction of the shrinkage function from the singular values of the Casorati matrix extracted the blood signal components from the image data. A PD image was then reconstructed by rearranging the filtered Casorati matrix into a sequence of 2D images and summing the signal power of each pixel over all frames. Vascular network morphological parameters were extracted from the resulting 2D PD images using a vessel skeletonization algorithm, implemented in ImageJ (National Institutes of Health), that is similar to [12]. The vascular network morphology features NV, NB, and VL were computed by recursively traversing the vessel skeleton.

Conventional time-intensity analysis of the 2D CEUS image sequences was estimated as the mean nonlinear signal intensity within the ROI for each frame of the cine loop. Perfusion parameters were then derived from the wash-in curves using the Vevo Lab software. In the statistical CEUS method [3], a Lomax distribution is fit to the histogram of contrast signal intensity within the tumor ROI for each frame of the replenishment sequence. The Lomax distribution approximates a mixture distribution of exponential functions. Enhanced volume fraction in each frame is estimated from the scale parameter of the Lomax distribution as detailed in [3]. A wash-in curve is constructed by plotting enhanced volume fraction versus time over the contrast replenishment interval. For both conventional and statistical CEUS, wash-in curves were characterized by fitting a monoexponential function as explained in [5] to estimate PE, RT, and AUC. Wash-in rate was also calculated from the monoexponential fit to the conventional CEUS sequence.

4.2.3 Classification and Feature Selection Algorithms

The eleven perfusion parameters plus tumor volume were used as inputs to a multivariable logistic regression model, as well as an SVM model, which were implemented in Python to classify resistant (*i.e.*, ACHN) and sensitive (*i.e.*, Caki-1) tumors to Sunitinib. The models were trained using supervised learning to output a binary classification of each tumor as sensitive or resistant to Sunitinib, with the expected sensitivity of the cell line (Caki-1 high, ACHN low) used as ground truth.

Leave-one-out cross validation was used to avoid overfitting due to the small numbers of tumors. For each of logistic regression and SVM, four different classifiers were trained using different combinations of input features: (1) features from conventional PD and CEUS only; (2) features from SVD-filtered PD and statistical CEUS only; (3) the best performing combination of features determined using backward elimination feature selection; and (4) all 12 features. Accuracy, sensitivity, specificity, and the AUC of ROC were computed to assess the performance of the models. The treatment-sensitive classification was treated as a positive result for the purposes of computing sensitivity and specificity.

Similarly, to evaluate the model performance on 786-O as an independent cell line and classify it to either sensitive or resistant group, SVM classifier is trained with tumor samples from ACHN and Caki-1 with both 12 ultrasound-based microvascular parameters and only selected set of parameters, and tested with 786-O. The treatment-sensitive classification was treated as a positive result for the purposes of computing sensitivity and specificity. Accuracy, sensitivity, specificity, and the AUC of ROC for classification performance were reported.

SHAP is a model-agnostic method for explaining individual predictions made by machine learning models and are used here to interpret the relative impact of large and small values and positive and negative values of each feature on the classification output [13]. It is based on cooperative game theory and aims to provide a unified approach to model interpretation by connecting feature importance and feature attribution. The method calculates the contribution of each feature to the final prediction for a specific input by calculating the difference between the model's prediction for the input with and without the feature. SHAP values are then used to rank the features by their importance to the prediction [14]. SHAP values were computed as described in [8] for all the eleven perfusion parameters plus tumor volume and for the logistic regression classification algorithm only.

Table 4.1: Perfusion parameters of conventional and developed PD and CEUS

Feature	Imaging Technique	Caki-1 tumors	ACHN tumors	786-O tumors
Tumor volume [mm ³]	Conventional PD	10.2 ± 3.1	15.9 ± 6.1	8.9 ± 4.2
Vascularization index	Conventional PD	3.7 ± 2.7	10.9 ± 3.8	5.8 ± 2.9
Number of vessels	SVD-filtered PD	25.6 ± 8.2	64.1 ± 14.9	34.5 ± 6.4
Number of Branching points	SVD-filtered PD	19.8 ± 5.4	45.4 ± 10.4	27.5 ± 8.7
Mean vessel Length [μm]	SVD-filtered PD	168 ± 18	170.2 ± 30	150.2 ± 10
Peak enhancement [a.u.]	Conventional CEUS	2.0 ± 1.7	8.2 ± 2.8	4.6 ± 1.9
Rise Time [s]	Conventional CEUS	5.9 ± 4.5	7 ± 3.8	7.1 ± 2.4
Area under the wash-in curve [a.u.]	Conventional CEUS	7.7 ± 5.3	13.1 ± 4.2	21.3 ± 6.5
Wash-in rate [a.u.]	Conventional CEUS	3.4 ± 1.8	8.9 ± 4.7	4.3 ± 3.8
Peak Enhancement [%]	Statistical CEUS	2.4 ± 1.8	16.5 ± 8.4	9.5 ± 4.3
Rise Time [s]	Statistical CEUS	12.8 ± 7.5	9.8 ± 4.4	11.7 ± 3.8
Area under the wash-in curve [%xs]	Statistical CEUS	15.4 ± 8.3	89.3 ± 24.8	31.9 ± 11.7

4.3 Results

4.3.1 Perfusion parameters for cell lines with different sensitivity level to antiangiogenic therapy

Table 4.1 lists the means and standard deviations of all 12 microvascular ultrasound image features for tumors from all three cell lines with sensitivity level to Sunitinib. As expected, a general trend of lower vascularity was observed in the Caki-1 mRCC tumor cells, which were expected to be Sunitinib-sensitive, compared ACHN mRCC tumor cells, which were expected to be resistant to Sunitinib. On the other hand, the 786-O RCC tumor cells from

primary tumor site exhibited relatively low vascularity, however, the microvascular parameters of 786-O tumor cell were slightly higher than that of Caki-1 tumor cells. It is mainly because 786-O tumor cells are less sensitive to Sunitinib than that of Caki-1 tumor cells. The highlighted features determine those selected by feature selection algorithm.

4.3.2 Utility of Lab-developed versus Conventional PD and CEUS perfusion parameters in Tumor Treatment Response Classification

Table 4.2 reports the classification performance of resistant from sensitive tumor cell lines for the four logistic regression and four SVM models in terms of accuracy, sensitivity, specificity and the area under the ROC curve. The best-performing classifier used selected perfusion parameters of VI from 3D conventional PD, NV and NB from 2D PD with optimal shrinkage SVD clutter filtering, and AUC of wash-in curve and PE from statistical CEUS. The model with all of features from both PD and CEUS derived from both conventional analysis and the newly developed analysis yielded the second-best performing model.

Table 4.2: Classification results using two different tumor cell lines.

	Model	Acc.	Sens.	Spec.	AROC
1	LR + conventional CEUS and PD features	0.87	0.84	0.89	0.92
2	LR + newly developed CEUS and PD features	0.85	0.91	0.88	0.92
3	LR + selected CEUS and PD features	0.95	0.97	0.96	0.98
4	LR + All CEUS and PD features	0.92	0.93	0.90	0.94
5	SVM + conventional CEUS and PD features	0.92	0.90	0.91	0.93
6	SVM + newly developed CEUS and PD features	0.94	0.93	0.93	0.94
7	SVM + selected CEUS and PD features	0.98	0.97	0.98	0.98
8	SVM + All CEUS and PD features	0.95	0.96	0.95	0.96

4.3.3 Feature Importance Analysis

Figure 4.1 shows the impact of each of the features on the classification of tumor treatment response. Higher-magnitude SHAP values imply higher impact; lower-magnitude SHAP values indicate lower importance. In figure 4.1, the horizontal axis displays the SHAP value, and the features are ordered vertically from the highest impact (top) to the lowest effect on the prediction (bottom). The violin plots show how the SHAP value for each feature changes as that feature's magnitude varies from low (blue) to high (red). High values of NV, NB, and AUC from statistical CEUS have an inverse relationship on the prediction (*i.e.*, a high value of one of these parameters suggests a treatment-resistant classification) and are the most important features in tumor treatment-response classification.

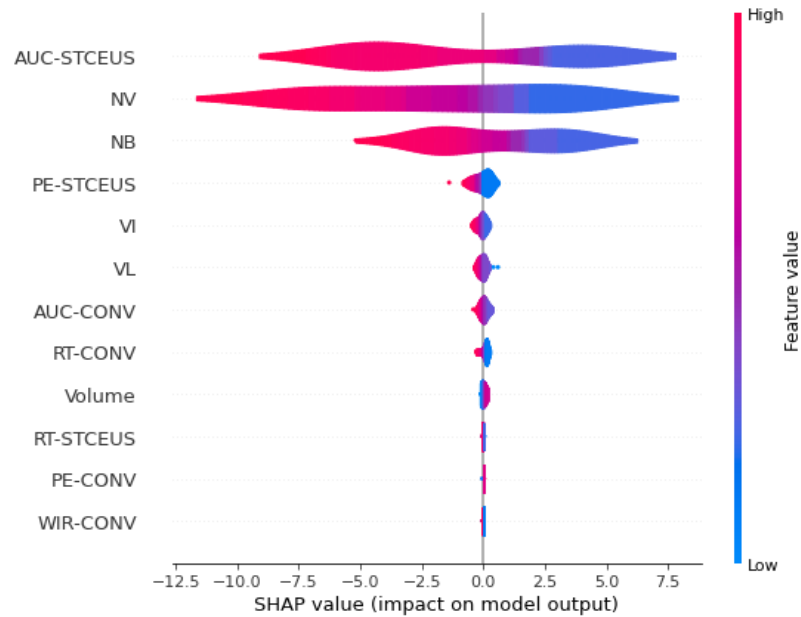


Figure 4.1: SHAP values of all the twelve features presented in this study. STCEUS stands for statistical analysis of CEUS while CONV is the conventional CEUS analysis.

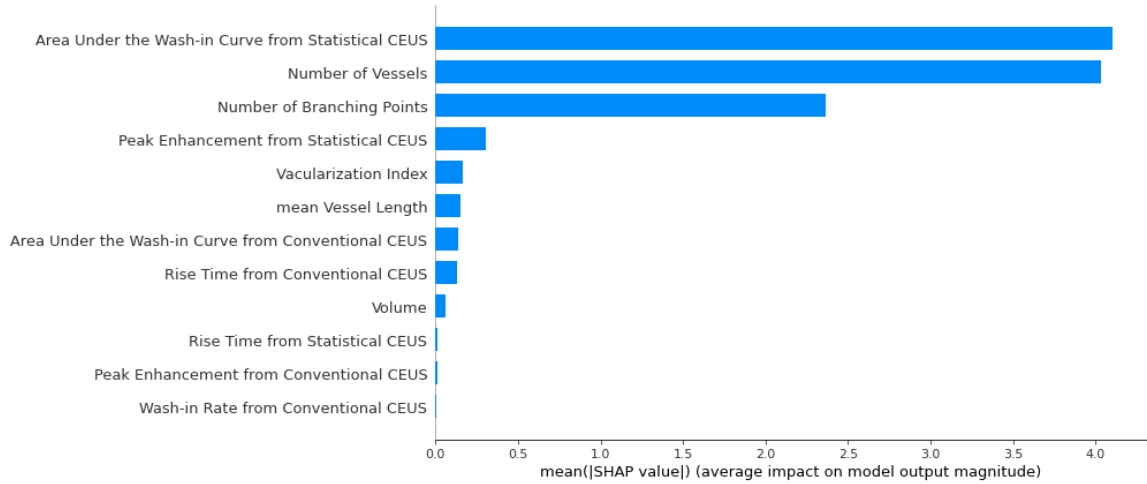


Figure 4.2: Feature Importance Analysis

4.3.4 Robustness and Generalization capabilities of the model pipeline

Table 4.3 reports the classification performance using an independent tumor cell line, *i.e.*, 786-O, as sensitive tumor cells to antiangiogenic therapy. The SVM classifier using all 12 features from PD and CEUS images achieved accuracy, sensitivity, and specificity of 82%, 78%, and 80%, respectively, with stratified sampling while the results were 87%, 83%, and 89%, respectively, for the selected parameters. The area under the ROC curve for classification of 786-O tumor cells was 0.85 and 0.88 using all and selected features, respectively, which was lower than the cross-validation AUC of 0.95 for the labeled cell lines. Similar to other performance results, it is expected to have lower AUC ROC when testing the model with an unseen test set than cross validation method.

Table 4.3: Classification results using 786-O tumor cell line.

	Model	Acc.	Sens.	Spec.	AROC
1	SVM + selected CEUS and PD features	0.87	0.83	0.89	0.88
2	SVM + All CEUS and PD features	0.82	0.78	0.80	0.85

4.4 Discussion

In this study, we investigated the utility of the combination of optimal shrinkage SVD clutter filtering for PD and statistical CEUS analysis for classifying tumors as sensitive or resistant to Sunitinib antiangiogenic treatment. The results indicate that conventional PD should be used in combination with SVD clutter filtered PD in circumstances, such as this study, where it is only practical to obtain 3D information from conventional PD. On the other hand, the statistical CEUS method may be sufficiently informative to recommend it be used in place of conventional mean-intensity CEUS analysis when additional information is available from PD modes.

The performance of the classification models was evaluated using two classification algorithms, logistic regression and SVM. The relative performance of the four logistic regression and the four SVM models followed a similar trend. With both logistic regression and SVM, the model with features selected by backward elimination outperformed the other three models, which represent the performance that could be expected if the choices of imaging methods are limited in advance (Models 1, 2, 5, and 6 in Table 4.2) or no choices are made about which imaging modes to use (Models 4 and 8 in Table 4.2). The consistency of performance with logistic regression and SVM demonstrates that the classification results are independent of the choice of classification algorithm.

The results also suggested that the machine learning model had reasonable generalization capabilities, but its performance on the 786-O as an independent test set was not as good as the cross-validation results. This behavior is common in machine learning models and is expected considering that in cross validation the model has already been trained on the data that it is being tested with. This discrepancy could be due to overfitting, which is a common issue in machine learning when the model starts to fit to the outliers in the training data. This means that the model may perform well on the training data (*e.g.*, cross validation or leave-one-out method) but fails to generalize well to new, unseen data. One way to address the issue of overfitting is to collect more data to improve the model's training and generalization capabilities.

Higher magnitudes of SHAP values for NV, NB, and AUC from statistical CEUS, compared to all other parameters, indicate their greater importance for classifying tumors as sensitive versus resistant to antiangiogenic treatment. Also, Fig. 4.1 further demonstrates that these features have inverse relation with the “sensitive” classification. This observation is consistent with the interpretation that lower NV and NB in the tumor means the antiangiogenic drug reduced the tumor vascularity and, therefore, the tumor was sensitive to the drug. Moreover, the aforementioned features with higher SHAP values are also the top five features selected by the backward elimination. The SHAP analysis is consistent with the conclusions about the importance of the features that can be drawn by comparing their mean values in Table I and confirms their importance in classification of treatment sensitivity.

The SHAP values also indicate that, for both conventional and statistical CEUS, AUC is the most informative wash-in curve parameter for classifying antiangiogenic treatment sensitivity. Moreover, Fig. 4.1 agrees with the results in chapter 3 [Table 3.3] where we compared the utility of conventional against statistical CEUS. In chapter 3, the backward feature elimination method selected AUC and PE from statistical CEUS and AUC and RT from conventional CEUS analysis as the best performing combination of CEUS features. In Fig. 4.1, we see that these features also have higher SHAP values compared to the other CEUS features for both conventional and statistical analysis.

The feature selection process for the final machine learning (ML) model considered features that exhibit both high correlations and interactions. Features are correlated because they are all representative of intra-tumoral microvascular structure. They are also with interactions since one feature can be calculated based on two other features (i.e., AUC that can be calculated based on PE and RT). The selected features from a combination of US imaging analysis suggests that both functional and structural features from 2-D and 3D of different analysis of PD and CEUS are informative for making classification. The model containing selected features outperform the model with all the features due to reduce noise, redundancy, and irrelevant information, focusing on the features that best represented the underlying microvascular structure and function.

The higher performance achieved by the ML model with the selected features compared to the model that included all features can be interpreted by enhanced relevance, decrease in redundancy and reduction in overfitting. The presence of correlated or redundant features in the full feature set can introduce noise or duplicate information, potentially hindering the model's performance. The selected features were likely more closely related to the target variable and contained stronger predictive power than the non-selected features. By excluding redundant features through feature selection, the model focused on the most distinct and informative ones, leading to improved discrimination and classification capabilities. On the other hand, including all available features in the model can lead to overfitting, where the model becomes too complex and fits the training data too closely, leading to poor generalization on unseen data. By selecting a subset of features, we are mitigating the risk of overfitting and allowing it to generalize better to new instances.

4.5 Conclusion

The machine learning models could classify resistant from sensitive tumors with high accuracy, precision and specificity using perfusion parameters from both newly developed and conventional analysis of PD and CEUS and therefore, the experimental design successfully produced two groups of tumors with distinctly different vascular architecture and perfusion. Moreover, the classification performance of the machine learning model for identifying 786-O as sensitive to therapy was relatively high, indicating its potential for accurately predicting the sensitivity of independent tumor test samples and its generalization capabilities.

Although these results of these studies are promising, they likely overestimate the classification sensitivity, specificity, and accuracy that can be expected in a clinical setting because CAM models using established cell lines do not model the intra and inter-tumor heterogeneity that is usually encountered in clinical cases.

References

- [1] M.-X. Tang, *et al.*, "Quantitative contrast enhanced ultrasound imaging: A review of sources of variability", *Interface Focus*, vol. 1, pp. 520-529, 2011.
- [2] M. Bataghva, *et al.*, "Contrast-free ultrasound microvascular imaging with optimal clutter shrinkage to enhance tumor vascular quantification", *IEEE Ultrasonic Symposium.*, 2020
- [3] M. R. Lowerison, *et al.*, "Compound speckle model detects anti-angiogenic tumor response in preclinical nonlinear contrast enhanced ultrasonography", *Medical Physics*, vol. 44, pp. 99-111. 2017
- [4] M. Bataghva, *et al.*, "Ultrasound-based microvascular parameters for classification of anti-angiogenic tumor treatment response: A scalable preclinical platform", *IEEE Ultrasonic Symposium*, 2020
- [5] M. Bataghva, *et al.*, "Comparison of contrast-enhanced ultrasound parameters for classification of anti-angiogenic tumor treatment response" , *IEEE Ultrasonic Symposium* 2021
- [6] N.M. D'Costa, *et al.*, "Y-box binding protein-1 is crucial in acquired drug resistance development in metastatic clear-cell renal cell carcinoma", *Journal of Experimental Clinical Cancer Research*, pp. 33-39, 2020
- [7] Magdalena Buczek, *et al.*, "Resistance to tyrosine kinase inhibitors in clear cell renal cell carcinoma: From the patient's bed to molecular mechanisms", *Biochimica et Biophysica Acta (BBA) - Reviews on Cancer*, vol. 1845, pp. 31-41, 2014.
- [8] A. Mizumoto, *et al.*, "Induction of epithelial-mesenchymal transition via activation of epidermal growth factor receptor contributes to sunitinib resistance in human renal cell carcinoma cell lines", *The Journal of Pharmacology and Experimental Therapeutics*, vol. 355, no. 2, pp. 152–158, 2015.
- [9] Y. Wang, *et al.*, "The E3 ligase RBCK1 reduces the sensitivity of ccRCC to sunitinib through the ANKRD35-MITD1-ANXA1 axis", *Oncogene*, vol. 42, no. 13, pp. 952-966, Mar. 2023
- [10] K.K. Brodaczewska, *et al.*, "Choosing the right cell line for renal cell cancer research", *Molecular Cancer*, vol. 15, no. 83, 2016
- [11] M. Gavish and D.L. Donoho. "Optimal shrinkage of singular values", *IEEE Transaction in Information Theory*, vol. 63, pp. 2137-2152, 2017
- [12] S. Ghavami, *et al.*, "Quantification of morphological features in non-contrast-enhanced ultrasound microvasculature imaging", *IEEE Access*, vol. 8, pp. 18925-18937, 2020

- [13] S. Lundberg, S. Lee, "A Unified Approach to Interpreting Model Predictions", *arXiv:1705.07874*
- [14] Z. Gaosen, *et al*, "A machine learning model based on ultrasound image features to assess the risk of sentinel lymph node metastasis in breast cancer patients: Applications of scikit-learn and SHAP", *Frontiers in Oncology*, 12, 2022

Chapter 5

5 Conclusion and Future Works

5.1 Summary

This research study aims to introduce a classification model pipeline based on ultrasound imaging microvascular parameters to evaluate the tumor treatment response. However, Since the conventional PD ultrasound images are not capable of provide accurate microvascular parameters due to the existence of the clutter, we first proposed a novel SVD-based clutter filtering for PD images to enhance the vascular quantification of ultrasound-based perfusion imaging through the use of optimal shrinkage SVD-based clutter filtering. The proposed method was compared to truncated SVD clutter filtering methods, and the results demonstrate significant improvements in image quality, visualization, and microvascular and perfusion quantification, leading to increased SNR and CNR, which, in turn, improve the quantification of tumor microvessels.

Moreover, to evaluate the tumor treatment response, we presented tumor engrafted on the CAM of chick embryo as a scalable and efficient preclinical tumor model to classify renal cell carcinoma tumor cell response to antiangiogenic treatment based on multiparametric ultrasound microvascular and perfusion parameters. Moreover, we demonstrated the effectiveness of the proposed machine learning model pipeline to study antiangiogenic treatment response using ultrasound microvascular imaging. We also evaluated the utility of microvascular and perfusion parameters derived from optimal shrinkage SVD-based power Doppler and statistical analysis of contrast-enhanced ultrasound in the context of

tumor treatment evaluation. The results indicated that derived features from these two analyses when used along with the microvascular parameters derived from conventional analysis will improve the classification of tumor response to antiangiogenic treatment.

We further assessed the robustness and the generalization capabilities of the multiparametric microvascular ultrasound machine learning pipeline with RCC tumor cells engrafted on the CAM of chick embryo to classify tumor treatment response on independent set of tumor cells with unknown treatment response to the machine learning model. The classification results demonstrated that the model pipeline is robust and can easily be generalized to any other tumor cell line.

5.2 Future Works

5.2.1 Optimal Shrinkage SVD Clutter Filtering

Real-time implementation of SVD-based clutter filtering can be challenging due to the large amount of data that needs to be processed. In medical imaging applications such as power Doppler ultrasound, real-time processing is critical for accurately identifying and tracking blood flow signals. Future research could focus on developing efficient algorithms that can perform clutter filtering in real-time [1]. For example, randomized SVD (rSVD) has been shown to successfully accelerate filtering of in vivo stationary tissues [2] where two methods of randomized singular value decomposition (rSVD) and randomized spatial down sampling were presented to improve the computational performance of singular value-based clutter filters for ultrasound blood flow imaging. Both methods were tested on a flow phantom and in vivo tissue with the presence of heavy tissue clutter and were found to provide comparable clutter rejection performance to full SVD with significantly improved computational performance.

Another possible approach is to use parallel processing techniques to distribute the computational load across multiple processors or graphics processing units (GPUs). This can help reduce the processing time and enable real-time implementation of SVD-based clutter filtering. In addition to developing more efficient algorithms, researchers can also investigate the use of machine learning techniques, such as convolutional autoencoders, to improve clutter filtering performance. These techniques can learn the underlying patterns

and features of clutter signals in a data-driven manner, which can help improve the accuracy of clutter filtering. For instance, a recent study [3] has shown that using convolutional autoencoders can improve clutter filtering in power Doppler ultrasound imaging, particularly in the presence of low signal-to-noise ratios and weak flow signals.

Furthermore, exploring the use of SVD-based clutter filtering in combination with other imaging techniques, such as contrast-enhanced ultrasound or microvascular imaging, can also be a promising direction for future research [4]. These techniques can provide complementary information about the microvascular structure and perfusion of tissues, which can help improve the detection of small blood vessels and slow blood flow signals. For example, [5] has shown that combining power Doppler ultrasound with contrast-enhanced ultrasound can improve the detection of slow blood flow signals in liver tumors. Such multimodal imaging approaches can provide more comprehensive and accurate information about tissue perfusion and can have potential applications in cancer diagnosis and treatment.

Moreover, the effectiveness of SVD filtering is reduced when blood, clutter, and noise do not follow orthogonal bases due to limitations in factorization rank and complex tissue motions. This overlap between signals creates a trade-off between clutter rejection and preservation of the blood signal. Although longer ensemble sizes improve SVD filtering, this is not practical in clinical settings where short ensemble lengths, typically less than 50 frames, are necessary to achieve real-time Doppler frame rates. For instance, the author in [6] presented a new filtering approach, which involved applying high-order SVD (HOSVD) to a 3-D tensor of aperture data containing spatial, slow-time, and channel dimensions and showed that leveraging spatial, temporal, and aperture features enhance the rejection of clutter and noise signals.

5.2.2 Other Tumor and Animal Models to Study Anti-Angiogenic Therapy Effectiveness

5.2.2.1 Use Patient Derived Xenografts (PDX) Tumors

In the proposed tumor model, the tumor cell lines are grown on the surface of the chick embryo which lacks the complexity of the tumor microenvironment. Patient-derived

xenografts (PDXs), on the other hand, are considered better than tumor cell lines to evaluate antiangiogenic drug treatment for several reasons [7]. First, PDXs are created by implanting fragments of human tumors directly into immunocompromised mice and CAM of chick embryo. This means that the tumor microenvironment, including the blood vessels and surrounding tissues, are preserved in the PDXs, which better mimics the complexity of human tumors. Therefore, PDXs are more representative of human tumors and can provide a more accurate prediction of the response to antiangiogenic drugs in human patients.

Additionally, using PDX models from actual patients allows for a more personalized approach to cancer research and treatment, potentially leading to more effective therapies tailored to individual patients. Thus, one possible future direction is to develop a tumor treatment response evaluation using the PDX tumor models. This would allow for more of a clinical translation of antiangiogenic treatment response of tumors xenografts from either primary or metastatic tumor site within the human body and determine their sensitivity to clinically used treatments.

5.2.2.2 Use of Mice Animal Models to Evaluate PDX Response to Antiangiogenic Drugs

On the other hand, mice are considered good preclinical animal models for the growth of PDXs for several reasons as well. These models are particularly useful because they closely mimic the human tumor microenvironment, allowing researchers to observe and evaluate the effectiveness of antiangiogenic therapies on the tumors in a controlled setting and makes the results of antiangiogenic treatment more translatable to humans. For instance, the study in [8] used a mouse model bearing clear-cell renal cell carcinoma xenograft tumors to test the effectiveness of using ultrasound microvascular imaging to evaluate response to anti-angiogenic therapy. Although mice animal models have their advantages, PDX models are notoriously difficult to establish in any host, so CAM assays may still be useful for time- or cost-sensitive applications [9].

5.2.3 Use of Additional Parameters for Tumor Treatment Response

The findings presented in this thesis demonstrated that ultrasound-based perfusion parameters could effectively classify tumor treatment response with decent performance when tested on independent tumor cells. However, it is possible to further enhance the classification performance by incorporating more features that are descriptive of tumor angiogenesis. One potential approach could be to include additional perfusion parameters, such as measures of vascular heterogeneity or microvascular density, from histology tests and genomics.

Vessel microstructure and perfusion parameters, such as blood vessel density, can be quantified from histological samples of tumors. These parameters provide important information about tumor microenvironment, angiogenesis, and the effectiveness of anti-angiogenic therapies. In addition, genomics-based approaches, such as gene expression profiling and DNA sequencing, provide additional information that supplements perfusion parameters. The use of perfusion parameters from histology tests and information from genomics represents a valuable approach for improving the accuracy of tumor response assessment and ultimately, the outcomes of cancer patients.

Perfusion parameters from genomics and histology tests can be useful when used along with ultrasound microvascular parameters in evaluating tumor antiangiogenic treatment response. For example, three-dimensional (3D) dynamic contrast enhanced ultrasound (DCE-US) perfusion map characterization can be used as an inexpensive, bedside and longitudinal indicator of tumor perfusion for prediction of vascular changes and therapy response [10]. Models developed using this method have shown excellent prediction of response in pre-clinical data and significant correlations with histological assessments of tumor vasculature. This approach can identify responders based on early perfusion changes, using perfusion properties correlated to gold-standard vascular properties.

5.2.4 Use of Ultrasound-based Perfusion Parameters in Other Anti-Angiogenic Treatment Response Evaluation

At the beginning of this research project, Sunitinib antiangiogenic drug was considered as the primary clinical treatment for metastatic renal cell carcinoma (mRCC). However, with

the advancements in clinical research, immune therapies have now become the main treatment for mRCC. Despite this, ultrasound-based perfusion parameters are not limited to evaluating the response of Sunitinib anti-angiogenic treatment alone, as explored in this thesis. These parameters can also be utilized to evaluate other tumors, such as breast tumors, prostate tumors, and thyroid tumors, as well as other antiangiogenic therapies, such as bevacizumab. Furthermore, these parameters can also be applied to other diseases with antiangiogenic therapies, such as peripheral arterial disease and coronary artery disease.

These parameters have the potential to be utilized in assessing the efficacy of a wide range of angiogenic and antiangiogenic therapies for various diseases. Angiogenic treatments are used in various diseases where promoting the formation of new blood vessels is necessary for tissue regeneration. For instance, anti-angiogenic treatments are used in various diseases where inhibiting the formation of new blood vessels is necessary to prevent tumor growth and other disease processes. The use of ultrasound-based perfusion parameters in the context of tumor antiangiogenic treatment can be extended to other drugs such as bevacizumab, Sunitinib, and sorafenib and in various types of cancer, such as colorectal, lung.

Angiogenic treatments are used for peripheral arterial disease (PAD), which is a condition characterized by the narrowing or blockage of blood vessels in the legs, leading to reduced blood flow to the affected limbs, to promote the formation of new blood vessels in the affected area, improving blood flow to the affected limb. Moreover, angiogenic treatments are used for coronary artery disease (CAD), a condition characterized by the narrowing or blockage of blood vessels that supply blood to the heart muscle which leads to chest pain or heart attack, to promote the formation of new blood vessels in the heart muscle and improving blood flow to the affected area.

5.3 Conclusion

Overall, this research project highlighted the potential of optimal shrinkage SVD-based clutter filtering and machine learning models for improving the accuracy and reliability of ultrasound-based microvascular imaging and for studying antiangiogenic therapy response. This study has shown that the combination of perfusion parameters from both proposed PD

and CEUS ultrasound image analysis are critical for assessing antiangiogenic sensitivity in a CAM tumor model. We have identified a minimal set of perfusion/microvascular parameters that are essential for evaluating antiangiogenic sensitivity, including selected vascularization index, number of vessels and vessel length from optimal shrinkage SVD filtered 2D and 3D PD, as well as area under the wash-in curve from 2D CEUS.

References

- [1] X. Yue, *et al.*, "Fast and Robust Clutter Filtering in Ultrafast Echocardiography", *Ultrasound in Medicine and Biology*, vol. 49, no. 2, pp. 441- 453, Feb. 2023
- [2] P. Song, *et al.*, "Accelerated Singular Value-Based Ultrasound Blood Flow Clutter Filtering With Randomized Singular Value Decomposition and Randomized Spatial Downsampling," *IEEE Transactions on Ultrasonics, Ferroelectrics, and Frequency Control*, vol. 64, no. 4, pp. 706-716, Apr. 2017
- [3] C. H. Shih and M. L. Li, "Power Doppler Imaging with a Novel Convolutional Autoencoder Based Clutter Filtering Technique: Feasibility Study", *IEEE International Ultrasonics Symposium (IUS)*, Glasgow, UK, pp. 2249-2251, 2019
- [4] K. Riemer, *et al.*, "On the Use of Singular Value Decomposition as a Clutter Filter for Ultrasound Flow Imaging", *arXiv:2304.12783*, [physics.med-ph], Apr. 2023
- [5] B. Pialot, *et al.*, "Adaptive noise reduction for power Doppler imaging using SVD filtering in the channel domain and coherence weighting of pixels", *Physics in Medicine and Biology*. vol. 68, no. 2, Jan. 2023
- [6] K. A. Ozgun and B. C. Byram, "Multidimensional Clutter Filtering of Aperture Domain Data for Improved Blood Flow Sensitivity," *IEEE Transactions on Ultrasonics, Ferroelectrics, and Frequency Control*, vol. 68, no. 8, pp. 2645-2656, Aug. 2021
- [7] Y. Choi, *et al.*, "Studying cancer immunotherapy using patient-derived xenografts (PDXs) in humanized mice", *Experimental and Molecular Medicine*, 50, pp. 1–9, 2018
- [8] J. D. Rojas, *et al.*, "Ultrasound Measurement of Vascular Density to Evaluate Response to Anti-Angiogenic Therapy in Renal Cell Carcinoma", *IEEE Transactions on Biomedical Engineering*, vol. 66, no. 3, pp. 873-880, Mar. 2019
- [9] M. Li, *et al.*, "Chick Chorioallantoic Membrane (CAM) Assay as an Efficient Xenograft Model of Hepatocellular Carcinoma", *Journal of Visualized Experiments*, vol. 104, 2015
- [10] A. El Kaffas, *et al.*, "Spatial Characterization of Tumor Perfusion Properties from 3D DCE-US Perfusion Maps are Early Predictors of Cancer Treatment Response", *Science Reports*, 10, 6996, 2020

Appendix: Copyright approval

The logo for Springer Nature, with "SPRINGER" in black and "NATURE" in red.

Decreased renal cortical perfusion, independent of changes in renal blood flow and sublingual microcirculatory impairment, is associated with the severity of acute kidney injury in patients with septic shock

Author: James Watchorn et al

Publication: Critical Care

Publisher: Springer Nature

Date: Sep 1, 2022

Copyright © 2022. The Author(s)

Creative Commons

This is an open access article distributed under the terms of the [Creative Commons CC BY](#) license, which permits unrestricted use, distribution, and reproduction in any medium, provided the original work is properly cited.

You are not required to obtain permission to reuse this article.

CC0 applies for supplementary material related to this article and attribution is not required.

JOHN WILEY AND SONS LICENSE
TERMS AND CONDITIONS

Jun 26, 2023

This Agreement between Mahsa Bataghva ("You") and John Wiley and Sons ("John Wiley and Sons") consists of your license details and the terms and conditions provided by John Wiley and Sons and Copyright Clearance Center.

License Number	5576331403252
License date	Jun 26, 2023
Licensed Content Publisher	John Wiley and Sons
Licensed Content Publication	Medical Physics
Licensed Content Title	Compound speckle model detects anti-angiogenic tumor response in preclinical nonlinear contrast-enhanced ultrasonography
Licensed Content Author	James C. Lacefield, David W. Holdsworth, Ann F. Chambers, et al
Licensed Content Date	Jan 19, 2017
Licensed Content Volume	44
Licensed Content Issue	1
Licensed Content Pages	13
Type of use	Dissertation/Thesis

Requestor type	University/Academic
Format	Electronic
Portion	Figure/table
Number of figures/tables	1
Will you be translating? No	
Title	PhD student
Institution name	Robarts research institute, Western University
Expected presentation date	Jul 2023
Portions	Fig. 1. Page 105
	Mahsa Bataghva 1151 Richmond St
Requestor Location	London, ON N6A 3K7 Canada Attn: Mahsa Bataghva
Publisher Tax ID	EU826007151
Total	0.00 USD
Terms and Conditions	

TERMS AND CONDITIONS

This copyrighted material is owned by or exclusively licensed to John Wiley & Sons, Inc. or one of its group companies (each a "Wiley Company") or handled on behalf of a society with which a Wiley Company has exclusive publishing rights in relation to a particular work (collectively "WILEY"). By clicking "accept" in connection with completing this licensing

transaction, you agree that the following terms and conditions apply to this transaction (along with the billing and payment terms and conditions established by the Copyright Clearance Center Inc., ("CCC's Billing and Payment terms and conditions"), at the time that you opened your RightsLink account (these are available at any time at <http://myaccount.copyright.com>).

Terms and Conditions

- The materials you have requested permission to reproduce or reuse (the "Wiley Materials") are protected by copyright.
- You are hereby granted a personal, non-exclusive, non-sub licensable (on a stand-alone basis), non-transferable, worldwide, limited license to reproduce the Wiley Materials for the purpose specified in the licensing process. This license, **and any CONTENT (PDF or image file) purchased as part of your order**, is for a one-time use only and limited to any maximum distribution number specified in the license. The first instance of republication or reuse granted by this license must be completed within two years of the date of the grant of this license (although copies prepared before the end date may be distributed thereafter). The Wiley Materials shall not be used in any other manner or for any other purpose, beyond what is granted in the license. Permission is granted subject to an appropriate acknowledgement given to the author, title of the material/book/journal and the publisher. You shall also duplicate the copyright notice that appears in the Wiley publication in your use of the Wiley Material. Permission is also granted on the understanding that nowhere in the text is a previously published source acknowledged for all or part of this Wiley Material. Any third party content is expressly excluded from this permission.
- With respect to the Wiley Materials, all rights are reserved. Except as expressly granted by the terms of the license, no part of the Wiley Materials may be copied, modified, adapted (except for minor reformatting required by the new Publication), translated, reproduced, transferred or distributed, in any form or by any means, and no derivative works may be made based on the Wiley Materials without the prior permission of the respective copyright owner. **For STM Signatory Publishers clearing permission under the terms of the STM Permissions Guidelines only, the terms of the license are extended to include subsequent editions and for editions in other languages, provided such editions are for the work as a whole in situ and does not involve the separate exploitation of the permitted figures or extracts**, You may not alter, remove or suppress in any manner any copyright, trademark or other notices displayed by the Wiley Materials. You may not license, rent, sell, loan, lease, pledge, offer as security, transfer or assign the Wiley Materials on a stand-alone basis, or any of the rights granted to you hereunder to any other person.
- The Wiley Materials and all of the intellectual property rights therein shall at all times remain the exclusive property of John Wiley & Sons Inc, the Wiley Companies, or their respective licensors, and your interest therein is only that of having possession of and the right to reproduce the Wiley Materials pursuant to Section 2 herein during the continuance of this Agreement. You agree that you own no right, title or interest in or to the Wiley Materials or any of the intellectual property rights therein. You shall have no rights hereunder other than the license as provided for above in Section 2. No right, license or interest to any trademark, trade name, service mark or other branding ("Marks") of WILEY or its licensors is granted hereunder, and you agree that you shall not assert any such right, license or interest with respect thereto

- NEITHER WILEY NOR ITS LICENSORS MAKES ANY WARRANTY OR REPRESENTATION OF ANY KIND TO YOU OR ANY THIRD PARTY, EXPRESS, IMPLIED OR STATUTORY, WITH RESPECT TO THE MATERIALS OR THE ACCURACY OF ANY INFORMATION CONTAINED IN THE MATERIALS, INCLUDING, WITHOUT LIMITATION, ANY IMPLIED WARRANTY OF MERCHANTABILITY, ACCURACY, SATISFACTORY QUALITY, FITNESS FOR A PARTICULAR PURPOSE, USABILITY, INTEGRATION OR NON-INFRINGEMENT AND ALL SUCH WARRANTIES ARE HEREBY EXCLUDED BY WILEY AND ITS LICENSORS AND WAIVED BY YOU.
- WILEY shall have the right to terminate this Agreement immediately upon breach of this Agreement by you.
- You shall indemnify, defend and hold harmless WILEY, its Licensors and their respective directors, officers, agents and employees, from and against any actual or threatened claims, demands, causes of action or proceedings arising from any breach of this Agreement by you.
- IN NO EVENT SHALL WILEY OR ITS LICENSORS BE LIABLE TO YOU OR ANY OTHER PARTY OR ANY OTHER PERSON OR ENTITY FOR ANY SPECIAL, CONSEQUENTIAL, INCIDENTAL, INDIRECT, EXEMPLARY OR PUNITIVE DAMAGES, HOWEVER CAUSED, ARISING OUT OF OR IN CONNECTION WITH THE DOWNLOADING, PROVISIONING, VIEWING OR USE OF THE MATERIALS REGARDLESS OF THE FORM OF ACTION, WHETHER FOR BREACH OF CONTRACT, BREACH OF WARRANTY, TORT, NEGLIGENCE, INFRINGEMENT OR OTHERWISE (INCLUDING, WITHOUT LIMITATION, DAMAGES BASED ON LOSS OF PROFITS, DATA, FILES, USE, BUSINESS OPPORTUNITY OR CLAIMS OF THIRD PARTIES), AND WHETHER OR NOT THE PARTY HAS BEEN ADVISED OF THE POSSIBILITY OF SUCH DAMAGES. THIS LIMITATION SHALL APPLY NOTWITHSTANDING ANY FAILURE OF ESSENTIAL PURPOSE OF ANY LIMITED REMEDY PROVIDED HEREIN.
- Should any provision of this Agreement be held by a court of competent jurisdiction to be illegal, invalid, or unenforceable, that provision shall be deemed amended to achieve as nearly as possible the same economic effect as the original provision, and the legality, validity and enforceability of the remaining provisions of this Agreement shall not be affected or impaired thereby.
- The failure of either party to enforce any term or condition of this Agreement shall not constitute a waiver of either party's right to enforce each and every term and condition of this Agreement. No breach under this agreement shall be deemed waived or excused by either party unless such waiver or consent is in writing signed by the party granting such waiver or consent. The waiver by or consent of a party to a breach of any provision of this Agreement shall not operate or be construed as a waiver of or consent to any other or subsequent breach by such other party.
- This Agreement may not be assigned (including by operation of law or otherwise) by you without WILEY's prior written consent.
- Any fee required for this permission shall be non-refundable after thirty (30) days from receipt by the CCC.

- These terms and conditions together with CCC's Billing and Payment terms and conditions (which are incorporated herein) form the entire agreement between you and WILEY concerning this licensing transaction and (in the absence of fraud) supersedes all prior agreements and representations of the parties, oral or written. This Agreement may not be amended except in writing signed by both parties. This Agreement shall be binding upon and inure to the benefit of the parties' successors, legal representatives, and authorized assigns.
- In the event of any conflict between your obligations established by these terms and conditions and those established by CCC's Billing and Payment terms and conditions, these terms and conditions shall prevail.
- WILEY expressly reserves all rights not specifically granted in the combination of (i) the license details provided by you and accepted in the course of this licensing transaction, (ii) these terms and conditions and (iii) CCC's Billing and Payment terms and conditions.
- This Agreement will be void if the Type of Use, Format, Circulation, or Requestor Type was misrepresented during the licensing process.
- This Agreement shall be governed by and construed in accordance with the laws of the State of New York, USA, without regards to such state's conflict of law rules. Any legal action, suit or proceeding arising out of or relating to these Terms and Conditions or the breach thereof shall be instituted in a court of competent jurisdiction in New York County in the State of New York in the United States of America and each party hereby consents and submits to the personal jurisdiction of such court, waives any objection to venue in such court and consents to service of process by registered or certified mail, return receipt requested, at the last known address of such party.

WILEY OPEN ACCESS TERMS AND CONDITIONS

Wiley Publishes Open Access Articles in fully Open Access Journals and in Subscription journals offering Online Open. Although most of the fully Open Access journals publish open access articles under the terms of the Creative Commons Attribution (CC BY) License only, the subscription journals and a few of the Open Access Journals offer a choice of Creative Commons Licenses. The license type is clearly identified on the article.

The Creative Commons Attribution License

The [Creative Commons Attribution License \(CC-BY\)](#) allows users to copy, distribute and transmit an article, adapt the article and make commercial use of the article. The CC-BY license permits commercial and non-

Creative Commons Attribution Non-Commercial License

The [Creative Commons Attribution Non-Commercial \(CC-BY-NC\) License](#) permits use, distribution and reproduction in any medium, provided the original work is properly cited and is not used for commercial purposes.(see below)

Creative Commons Attribution-Non-Commercial-NoDerivs License

The [Creative Commons Attribution Non-Commercial-NoDerivs License \(CC-BY-NC-ND\)](#) permits use, distribution and reproduction in any medium, provided the original work is

properly cited, is not used for commercial purposes and no modifications or adaptations are made. (see below)

Use by commercial "for-profit" organizations

Use of Wiley Open Access articles for commercial, promotional, or marketing purposes requires further explicit permission from Wiley and will be subject to a fee.

Further details can be found on Wiley Online Library
<http://olabout.wiley.com/WileyCDA/Section/id-410895.html>

Other Terms and Conditions:

v1.10 Last updated September 2015

Questions? customercare@copyright.com.

Curriculum Vitae

Name:	Mahsa Bataghva Shahbaz
Post-secondary Education and Degrees:	<p>Semnan University Semnan, Iran 2009 - 2013 B.Sc. in Electrical Engineering</p> <p>The University of Western Ontario London, Ontario, Canada 2015 - 2017 M.Sc. in Electrical Engineering</p>
Honours and Awards:	<p>IEEE WIE Inspiring Student Member of the Year Award Honorable Mention (USD \$250), 2022, IEEE Women In Engineering, Global</p> <p>Best Pitch Presentation Award (\$500), 2021, Graduate Student Innovation Scholars (GSIS) program by WORDiscovery & Ivey Business School at Western University & Western Morrisette Institute for Entrepreneurship</p> <p>1st place award (USD \$2500), 2021, 1st Innovation Sprint, Mayo Clinic, Rochester, USA</p> <p>Best Poster Presentation Award (CAD \$350), 2019, 17th Imaging Network Ontario Symposium, London, ON.</p> <p>Excellent Oral Presentation Award (CAD 200\$), 2019, Robarts Research Retreat</p> <p>The Best Affinity Group of the Year Award (USD \$500), 2018, IEEE Women In Engineering, Global</p> <p>Academic Achievement Scholarship (CAD \$500), 2018, Public Service Alliance of Canada, Local 610, Canada</p> <p>Travel Award (CAD \$400), 2017, Electrical and Computer Engineering Dept., Western University, Canada</p>
Related Work Experience	<p>Teaching Assistant The University of Western Ontario 2015-2022</p>

Peer-Reviewed Journals:

- [1] **M. Bataghva**, F. Serack, C. Leclerc, D. Johnston, D. Hess, L. Flynn, N. Power, S. Penuela and J. C. Lacefield, "Contrast-Free Ultrasound Microvascular Imaging With Optimal Shrinkage Clutter Filtering to Enhance Vascular Quantification", *IEEE Transactions on Medical Imaging* (Submitted)
- [2] Saeed Samadizadeh, Maha Masoudi, Mostafa Rastegar, Vahid Salimi, **Mahsa Bataghva Shahbaz**, Alireza Tahamtan, "COVID-19: Why does disease severity vary among individuals? ", *Respiratory Medicine*, Volume 180, 2021, 106356
- [3] Majid Teymoori-Rad, Saeed Samadizadeh, Alijan Tabarraei, Abdolvahab Moradi, **Mahsa Bataghva Shahbaz** & Alireza Tahamtan "Ten challenging questions about SARS-CoV-2 and COVID-19", *Expert Review of Respiratory Medicine*, 2020, 14:9, 881-888
- [4] A. Behnad, **M. Bataghva Shahbaz**, T. J. Willink and X. Wang, "Statistical Analysis and Minimization of Security Vulnerability Region in Amplify-and-Forward Cooperative Systems," in *IEEE Transactions on Wireless Communications*, vol. 16, no. 4, pp. 2534-2547, April 2017

Conference Proceedings:

- [1] **M. Bataghva**, D. Johnston, N. Power, A. Ward, S. Penuela and J. C. Lacefield, "Multiparametric Microvascular Ultrasound to Classify Tumor Sensitivity to Anti-Angiogenic Treatment: Application to Multiple Cell Lines", *IEEE International Ultrasonics Symposium (IUS)*, Venice, Italy, 2022, pp. 1-4
- [2] **M. Bataghva**, D. Johnston, N. Power, A. Ward, S. Penuela and J. C. Lacefield, "Comparison of Contrast-Enhanced Ultrasound Parameters for Classification of Anti-Angiogenic Tumor Treatment Response," *2021 IEEE International Ultrasonics Symposium (IUS)*, Xi'an, China, 2021, pp. 1-4
- [3] **M. Bataghva**, D. Johnston, N. Power, S. Penuela and J. C. Lacefield, "Contrast-Free Ultrasound Microvascular Imaging With Optimal Clutter Shrinkage to Enhance Tumor Vascular Quantification," *2020 IEEE International Ultrasonics Symposium (IUS)*, Las Vegas, NV, USA, 2020, pp. 1-4
- [4] **M. Bataghva**, D. Johnston, N. Power, S. Penuela and J. C. Lacefield, "Ultrasound-Based Microvascular Parameters for Classification of Anti-Angiogenic Tumor Treatment Response: A Scalable Preclinical Approach," *2020 IEEE International Ultrasonics Symposium (IUS)*, Las Vegas, NV, USA, 2020, pp. 1-4
- [5] **M. B. Shahbaz**, Xianbin Wang, A. Behnad and J. Samarabandu, "On efficiency enhancement of the correlation-based feature selection for intrusion detection systems," *2016 IEEE 7th Annual Information Technology, Electronics and Mobile Communication Conference (IEMCON)*, Vancouver, BC, Canada, 2016, pp. 1-7

Other conference presentations & Abstracts:

[1] **Mahsa Bataghva**, James C. Lacefield, “Monitoring Microvascular of PDX Model of RCC Tumor Response to Vascular Targeted Therapy Using Adaptive Clutter Filter for Ultrasound PD Imaging”, *11th International Conference on Ultrasonic Biomedical Microscanning*, Lakeville, CT, USA, 2018 (Oral Presentation)

[2] **Mahsa Bataghva**, Fiona Serak, Christopher Leclerc, David Hess, Lauren Flynn, James C. Lacefield, “Contrast-Free Ultrasound Microvascular Imaging to Enhance Vascular Quantification in a Mouse Model of Peripheral Artery Disease”, *Imaging Network of Ontario*, Virtual, 2021 (Oral Presentation)

[3] **Mahsa Bataghva**, Fiona Serak, Christopher Leclerc, David Hess, Lauren Flynn, James C. Lacefield, “Contrast-Free Ultrasound Microvascular Imaging to Enhance Vascular Quantification in a Mouse Model of Peripheral Artery Disease”, *London Health Research Day*, London, ON. Canada, 2021 (Oral Presentation)

[4] **Mahsa Bataghva**, James C. Lacefield, “Ultrasound-Based Microvascular Parameters for Classification of AntiAngiogenic Tumor Treatment Response: A Scalable Preclinical Approach”, *Robarts Research Retreat*, London, ON. Canada, 2020 (Poster Presentation)

[5] **Mahsa Bataghva**, James C. Lacefield, “Microvessel Detection in Power Doppler Ultrasound Using Adaptive Singular Value Decomposition Clutter Filtering”, *Imaging Network of Ontario*, London, ON. Canada, 2019 (Poster Presentation)

[6] **Mahsa Bataghva**, James C. Lacefield, “Microvessel Detection in Power Doppler Ultrasound Using Adaptive Singular Value Decomposition Clutter Filtering”, *Robarts Research Retreat*, London, ON. Canada, 2019 (Oral Presentation)